Aeroelastic Characteristics of a Rapid Prototype Multi-Material Wind Tunnel Model of a Mechanically Deployable Aerodynamic Decelerator

Submitted By

Boris Raskin

IN PARTIAL FULFILLMENT OF THE REQUIREMENTS FOR THE DEGREE OF

MASTER OF SCIENCE IN MECHANICAL ENGINEERING

School of Engineering
Tufts University
Medford, Massachusetts

May 2016

Certified By:
Professor Robert White
Department of Mechanical Engineering
Tufts University

Committee:
Professor Chris Rogers
Department of Mechanical Engineering
Tufts University

Committee:
Mr. Kurt Long
NASA Ames Research Center

Abstract

Scaled wind tunnel models are necessary for the development of aircraft and spacecraft to simulate aerodynamic behavior. This allows for testing multiple iterations of a design before more expensive full-scale aircraft and spacecraft are built. However, the cost of building wind tunnel models can still be high because they normally require costly subtractive manufacturing processes, such as machining, which can be time consuming and laborious due to the complex surfaces of aerodynamic models. Rapid prototyping, commonly known as 3D printing, can be utilized to save on wind tunnel model manufacturing costs.

A rapid prototype multi-material wind tunnel model was manufactured for this thesis to investigate the possibility of using PolyJet 3D printing to create a model that exhibits aeroelastic behavior. The model is of NASA's Adaptable Deployable entry and Placement (ADEPT) aerodynamic decelerator, used to decelerate a spacecraft during reentry into a planet's atmosphere. It is a 60° cone with a spherically blunted nose that consists of a 12 flexible panels supported by a rigid structure of nose, ribs, and rim.

The novel rapid prototype multi-material model was instrumented and tested in two flow conditions. Quantitative comparisons were made of the average forces and dynamic forces on the model, demonstrating that the model matched expected behavior for average drag, but not Strouhal number, indicating that there was no aeroelastic behavior in this particular case. It was also noted that the dynamic properties (e.g., resonant frequency) associated with the mounting scheme are very important and may dominate the measured dynamic response.

Tests were run for the models mounted on 30.50 cm and 19.05 cm rods, at 0°, 15°, and 60° angle of attacks in 16.8 m/s and 32.6 m/s flow. The drag force on both stiff and soft decelerator models at 0° and 15° angle of attack was near 1.0 which agrees with data on the Viking lander collected in the 1970's of similar geometry. However, the drag force was much lower, near 0.5, for the model at a 60° angle of attack because the drag force was reduced by about twice as much as the projected frontal area as compared to 0° angle of attack. The drag coefficients of the stiff and soft models had no statistically significant difference. There was also no statistically significant difference between the Stouhal number (St) of stiff and soft decelerator models. However, the St varied depending on the length of the rod that the model was mounted on and the flow velocity. This shows that the resonant frequency corresponds to the natural frequency of the mechanical system, rather than aeroelastic behavior. This was confirmed by performing tap tests to verify that the resonant frequencies of the underdamped system coincided with the resonant frequencies from the flow testing. Wake data was also collected by measuring the dynamic pressure behind the model to verify that the flow velocity was accelerated as it flowed around the model and there was a shadow behind the decelerator model with swirls. The conclusion reached was that aeroelastic behavior was not visible because the dynamics of the mechanical system dominated the data. The scale of the decelerator and the experimental setup would need to be modified in order to attempt to detect aeroelastic phenomena. However, the use of multi-material rapid prototyping for a scale aerodynamic model was successfully demonstrated for the first time, and similitude parameters of relevance to the problem were delineated.

Acknowledgements

Firstly, I would like to express my sincere gratitude to my advisor, Professor Robert White, for the continued support of this research, for his patience, motivation, and guidance as I worked on this research. I would also like to thank him for giving me the opportunity to work on this important topic. His willingness to accommodate my schedule and stay late on many days was instrumental to allow me the opportunity to work with him. His advice helped me immensely at all stages of research and writing of this thesis.

My sincere thanks also go to the rest of my thesis committee: Professor Chris Rogers and Kurtis R. Long for their insightful comments and encouragements.

I would like to thank NASA Ames Research Facility for allowing the use of their facilities for running wind tunnel testing using their equipment. Without this support, it would not be possible to conduct this research.

I want to thank my fiancé, Kayley, for providing emotional support and encouragement during long days and late nights of work. Lastly, I could not have done it without the support of my family: my parents, brother, sister-in-law for supporting me throughout writing this thesis and my life in general.

Table of Contents

Table of Figures

Table of Tables

1 Introduction

This thesis investigates the possibility of using the PolyJet 3D printing rapid prototyping (RP) technique to successfully create a wind tunnel model of a mechanically deployable aerodynamic decelerator with aeroelastic characteristics. Scaled wind tunnel models are necessary in development of aircraft in order to simulate their aerodynamic behavior in testing multiple iterations of a design before building more expensive full scale aircraft. However, the cost of building wind tunnel models can still be high because they normally require costly subtractive manufacturing processes, such as machining which can be time consuming and laborious due to the complex surfaces of aerodynamic models. Rapid prototyping can be utilized to save on wind tunnel model manufacturing costs.

Many groups have already used rapid prototyping to create wind tunnel models to illustrate the cost savings that can be realized. A lot of techniques have been attempted to model different types of aircraft, with a number of different rapid prototyping technologies, materials, and applications. The ones that are documented in literature are covered in chapter 2: SLA rapid prototyping [1-7]; comparison of SLA, SLS, FDM, LOM rapid prototyping [8]; FDM models with reinforcements [9-11]; wind tunnel models with internal features [12-14]; wind tunnel model pieces that are assembled with other conventionally machined pieces [15-17]; plated rapid prototyping materials [18]. Aeroelastic models have even been created by taking advantage of the flexibility of the SLA material [19]. PolyJet has also been utilized to create wind tunnel models from a single material [20-22].

The goal of this thesis is to determine whether the range of properties and scales available for a multi-material PolyJet printer will allow construction of self-similar models to full scale vehicles that exhibit aeroelastic behavior and to explore a specific example of this process for the ADEPT decelerator. The soft decelerator model that was constructed contains flexible panels that could potentially exhibit aeroelastic behavior, meaning that there is interaction between aerodynamic, inertial, and elastic forces resulting in deformation or vibration of the model's flexible panels. Significant cost saving can be realized if a multi-material rapid prototype model can be used to model full scale aircraft made from both hard and soft materials.

The model with the flexible panels has a rigid supporting structure, which includes the ribs, nose, rim and soft panels that deflect when pressed. To verify their mechanical properties for use in similitude calculations, the stiff, VeroClear, and soft, TangoPlus, materials that the models were constructed from were also tensile tested to determine their mechanical properties. It was observed that the VeroClear material has an elastic modulus of 0.393 GPa and a tensile strength of 19.1 MPa. The TangoPlus material has an elastic modulus of 0.354 MPa and a tensile strength of 0.566 MPa.

A number of wind tunnel tests were conducted. The 1:49 scale stiff and soft decelerator models were tested by mounting them on a rod that was attached at the lower end to a torque transducer. Torque measurements of the transducer were converted into force data which was used to calculate the drag force and coefficients under a number of different conditions. The stiff and soft decelerators were tested on 30.50 cm and 19.05 cm rods, at 0°, 15°, and 60° angles of attack and in 16.8 m/s and 32.6 m/s flows. The Reynolds numbers of the 16.8 m/s and 32.6 m/s flows based on diameter of the

decelerator were 147,000 and 284,000 respectively. The drag coefficients of both stiff and soft models were near 1 for both rod lengths at 0° and 15° angles of attack which agree with known values of drag coefficient for similar geometry of the Viking lander aeroshell. The drag coefficient for both stiff and soft models was near 0.5 for both rod lengths at 60° angle of attack. This drag coefficient is lower than expected at this angle of attack; unfortunately, the Viking lander data is not available for comparison for such a steep angle of attack. The resonant frequencies of the models in flow were near 28 Hz for both models in both flow velocities on the 19.05 cm rod and near 16 Hz for both models in both flow velocities on the 30.50 cm rod. Once again, the primary feature seen in the vibration spectrum is the first structural mode and there is no evidence of aeroelastic flow effects.

In addition to the wind tunnel testing under flow, the models were tested with the wind tunnel off in order to find their resonant frequency by tap testing and recording the response of the mechanical system. The decelerator on rod was found to be an underdamped mass-spring system that vibrates at 28 Hz on the 19.05 cm rod and 16 Hz on the 30.50 rod. This suggests that the resonant frequency of the model in flow is dominated by the resonant frequency of the mechanical system which is excited by broadband unsteady forcing.

Wake measurements were also taken using a pitot tube behind the model that traversed up from the floor of the tunnel which measured the dynamic pressure that was converted into a velocity profile. The measurements produced expected results which showed that the flow accelerates as it is forced around the decelerator model and there is a shadow where the flow reverses in a wake behind the decelerator model.

Similitude calculations were performed to determine the nondimensional parameters of the wind tunnel model. It became apparent that it was not practically possible to match the full scale decelerator similitude parameters with this size model for the types of flow conditions expected in a Venus reentry, although it may be possible for other geometries or less extreme operating conditions. Similitude issues will be demonstrated through direct numerical examples relevant to this study.

1.1 Contributions

To the best of our knowledge, this is the first demonstration of a multi-material rapid prototype aeroelastic wind tunnel model. The novel rapid prototype multi-material model was instrumented and tested in flow conditions. Quantitative comparisons were made of the average forces and dynamic forces on the model, demonstrating that the model matched expected behavior for average drag, but not demonstrating any aeroelastic behavior for this particular case. It was also noted that the dynamic properties (e.g. resonant frequency) associated with the mounting scheme are very important and may dominate the measured dynamic response.

Known nondimensional parameters describing the aerodynamic and aeroelastic behavior have been elucidated for this case. Example computations for the types of materials available in multi-material 3d printing show the difficulty of matching the properties of the full-scale article at this size scale. The nondimensional parameters can be matched by increasing the length scale and decreasing the thickness of the panels of the wind tunnel models as well as increasing the flow velocity in the wind tunnel while keeping it compressible, below Mach 0.3.

2 Background

2.1 Rapid Prototyping

Rapid prototyping (RP) technology is employed to quickly create components from CAD models using an additive process without the use of conventional tooling. In an additive process, components are built by depositing materials in layers to obtain the final geometry [23]. In the mid-1980s, a number of rapid prototyping technologies first emerged that were capable of creating both plastic and metallic rapid prototyped parts. Today, many technologies are available that use different techniques to form the layers from a variety of materials. More than 40 different types of RP technologies are currently available. Some of the most commonly used ones are stereolithography (SLA), selective laser sintering (SLS), laminated object manufacturing (LOM), fused deposition modelling (FDM), multi-jet modelling (MJM), and three-dimensional printing (3DP) [24].

A list of common rapid prototype processes, the companies that commercialized their respective technology and description of the method by which parts are built using that process are listed in Table 2-1. Many of today's commercialized "3D printers" should not be confused with the three-dimensional printing (3DP) technology commercialized by Z-Corporation. Most of the "3D printers" on the market use a different type of technology. For example, the tabletop MakerBot line of printers uses FDM, while the Form 1+ tabletop 3D printer uses SLA. This thesis will sometimes refer to different types of rapid prototyping techniques by the now commonly used term, "3D printing".

Technology	Commercialized by	Process	Method
Stereolithography (SLA)	3D Systems (California, USA)	Photo curing	A UV laser hits a vat of photopolymer epoxy resin and solidifies the polymer in layers as it traces each layer. The base tray is lowered 0.050-0.250 mm at a time.
Selective Laser Sintering (SLS)	DTM Corp (Texas, USA)	Sintering of powders	Material particles or granules are fused or sintered as they are layered.
Laminated Object Manufacturing (LOM)	Helisys Inc. (California, USA)	Paper lamination	An adhesive layer of material is stuck to the previous layer and a laser is used to cut away the unused material.
Fused Deposition Modeling (FDM)	Stratasys (Minnesota, USA)	Melt extrusion	Molten bead of material is extruded by a movable nozzle in layers and bonds with the previous layer. A second nozzle is used to extrude another material for a support structure.
Multi-jet Modelling (MJM)	3D Systems (California, USA)	Melt extrusion	A print head containing many tiny nozzles passes over the part in x-y plane and deposits droplets of thermo-plastic polymer which bond to the previous layer.
Three-dimensional printing (3DP)	Z Corporation (Massachusetts, USA)	Ink-jet printing	Corn starch material is released from a feed chamber and a feed roller spreads the material over the build chamber. A binder cartridge moves in the x-y plane and deposits a binder solution to build the layers as the build platform is lowered.

Table 2-1: List of common rapid prototyping technologies [23, 24]

More recently, a specific type of RP technology called polyjet printing (PP) emerged. The technology was developed by a company called Objet Geometries Ltd in Rehovot, Israel which was later acquired by Stratasys when Objet became one of Stratasys' brands. PP is of particular interest for this thesis because it allows printing one component using multiple materials that have different physical properties [25]. This makes it possible to print multi-material components out of both hard and flexible materials with different mechanical properties. During printing, the jetting printer head moves back and forth along the x-axis as shown in Figure 2-1, while depositing a very thin (16 micron) layer of photopolymer onto the previous layer or

initially onto the build tray as it transverses along the y-axis. A polyjet printer uses ultraviolet (UV) light which is located in the printer head to cure photopolymer materials as the head moves along the x-axis. In addition to the materials used to print the actual component, another soft gel like material is printed around the component for support. After printing is complete, this supporting material can be removed from the component by a water jet or hand and brush [23, 26]. The ability to create multi-material models makes it very convenient to evaluate designs that consist of multiple materials.

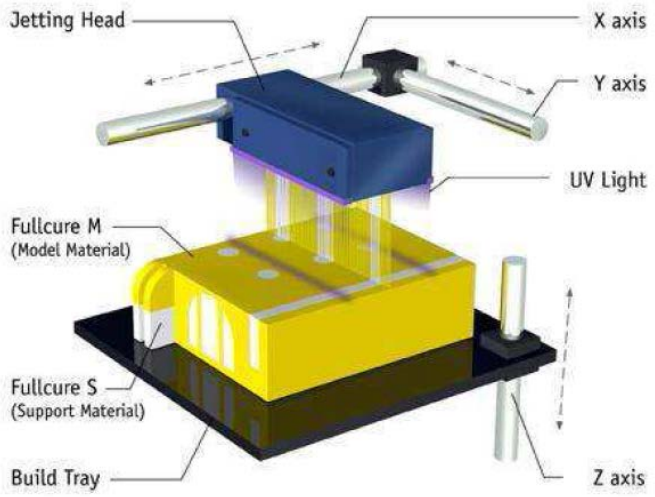

Figure 2-1: Polyjet Printer Technology [21]

The typical process of manufacturing a model by RP starts with a solid model created in computer aided design (CAD) software. The original file is converted into an STL format which is a volumetric mesh representation of the geometry. STL is the neutral CAD format used by most 3D printers. The STL file is imported into the 3D printer software that then splits it up into layers and support material is added if necessary. The model is then built in layers and after 3D printing is complete, it is removed and cleaned of support or unneeded material. Figure 2-2 shows the general steps of a typical RP process.

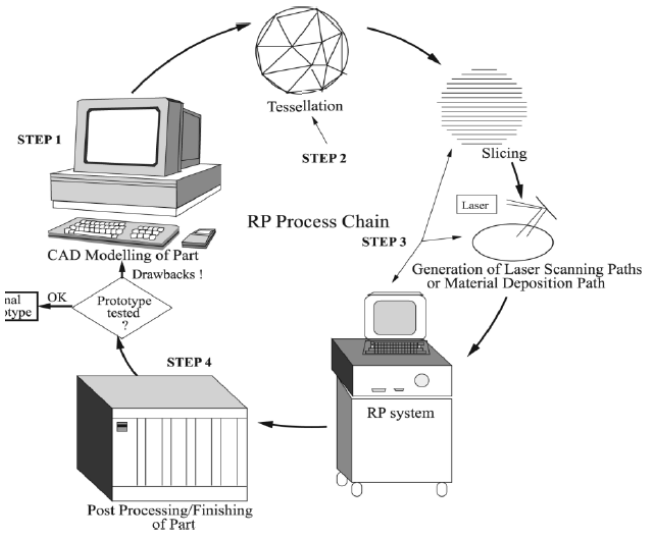

Figure 2-2: General steps of a RP process [23]

RP is used in a variety of applications, including concept modeling and proof of concept during a product's design. It is also used in manufacturing to create fit and functional models, pattern making for casting processes, and rapid tooling. There are medical field applications where 3d printed parts are used as surgical aids, drug delivery systems, or bone implants [27]. RP is also often used in aerodynamic studies of wind tunnel models.

2.2 Wind-Tunnel Testing of Rapid Prototyped Models

Wind tunnel models are used to test the aerodynamic performance of a design before creating the final product. Wind tunnel testing makes it possible to create multiple iterations of designs and subsequently models to test performance before choosing the final design. It is also possible to use non-dimensional analysis to scale down a model in order to test a large design in a smaller size wind-tunnel.

RP is well-suited for fabrication of aerodynamic wind-tunnel models due to the fact that the model geometry is typically complex. This is an alternative to the traditional subtractive manufacturing processes, such as computer numerical control (CNC) machining, which may be

time consuming and laborious due to the complex surfaces of aerodynamic models. Due to the nature of RP techniques which are additive processes, the models can be built much more quickly and cost effectively. The model created using a rapid prototyping technique can be used in lieu of a machined model if it is dimensionally accurate, has an acceptable surface roughness, and is strong enough to withstand the load from aerodynamic forces [8].

RP was first introduced as a new option in aerodynamic modelling in the late 1980s when a wind tunnel model was created in CAD software and fabricated by using SLA. The acrylic model was then tested in a low-speed wind tunnel [1]. Since then, SLA has become an accepted manufacturing technique for creating wind tunnel models as shown by the research into the feasibility of using SLA RP in the airfoil design process conducted by Landrum et al. In this study, the airfoil model fabricated from polyurethane by a common casting technique was compared to an airfoil fabricated using the SLA process. The two were found to produce similar aerodynamic testing results, showing that surface finish produced by SLA is comparable to that of 'aerodynamically smooth' surfaces [2].

Several studies were also performed by Springer et al. at the NASA Marshall Space Flight Center to compare static stability aerodynamic properties of launch vehicle models fabricated using SLA and conventional models in low-speed, transonic, and high-speed wind tunnels [3-7]. At the time they were conducting the experiments (1997 and 1998), they concluded that only preliminary design studies with limited configurations could be performed due to bending of the materials that occurred because of poor mechanical properties of the materials. However, they foresaw at the time that with the rapid improvement in RP material properties, it would soon be possible to use RP models in a wider range of wind tunnel testing applications.

In addition to SLA, as other RP fabrication processes emerged and became more affordable and accessible, they were considered for creating wind tunnel models. Chuk et al. [8] made an analysis of nine RP processes in 1998 that were considered in the creation of wind tunnel models when Bombardier Aerospace Inc. was looking to improve wind tunnel model fabrication time and cost: SLA, SLS, FDM, LOM, solid ground curing (SGC), Sanders ModelMaker (MM), direct shell production casting (DSPC), 3D Keltool, and RapidTool.

The processes were analyzed to compare the most important RP component requirements, which are dimensional accuracy, surface finish, and strength. The following criteria were established to evaluate the RP technologies: cost, time, build envelope, material strength, additional engineering, and availability. The study showed that RP wind tunnel models could be created with necessary accuracy and may be used when they do not undergo significant loads. However, at the time, they could not completely replace machined components for thin section parts, such as tip fins and flaps. The authors did foresee that with the fast advancement of the technology, this would become possible as the mechanical properties of RP materials were improving.

Some novel techniques have been employed to work around the problem of RP materials' low strength. Hildebrand et al. [9], working for the Air Force Research Laboratory (AFRL), built a model which was 3 feet long with a span of 4 feet. To strengthen the model, it was fabricated in pieces and reinforced with metallic parts that also held the model pieces together. Similar work was performed by Kroll et al. [10, 11], who proposed using stiffening plates when assembling wind tunnel models made by FDM technology. Kroll described the advantage of RP short build times in a classroom setting where students have limited time to create models of designs that are developed over the course of a semester-long class and that

are only finished at the end of the semester with several weeks left for testing of the created concepts. One of the models that was designed and tested is CERBERUS, a low radar cross section (low- RCS), long-range unmanned aerial vehicle (UAV) bomber illustrated in Figure 2-3 (b). The model was reinforced and held together with stiffening plates. Another model tested was ILAS, a low-altitude, quiet, fuel-cell powered observation aircraft carrying an electro-optical payload. The full scale aircraft had a wing span of 3 m and could fly at a speed of 20-25 m/s. The scale of the wind tunnel model was 1:5.5. The model shown in Figure 2-4 was reinforced and held together by stiffening rods that ran horizontally across the model, perpendicular to the direction of flight.

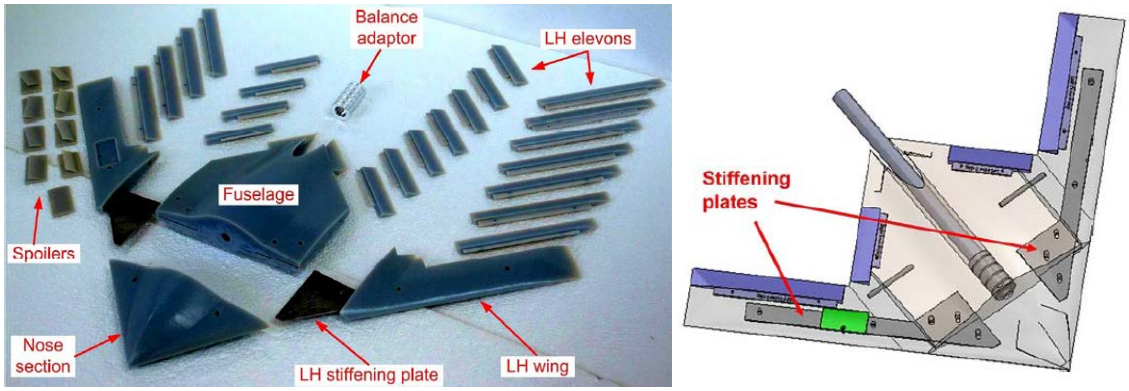

(a) (b)

Figure 2-3: CERBERUS, a low-RCS, UAV bomber (a) wind tunnel model pieces and (b) CAD model

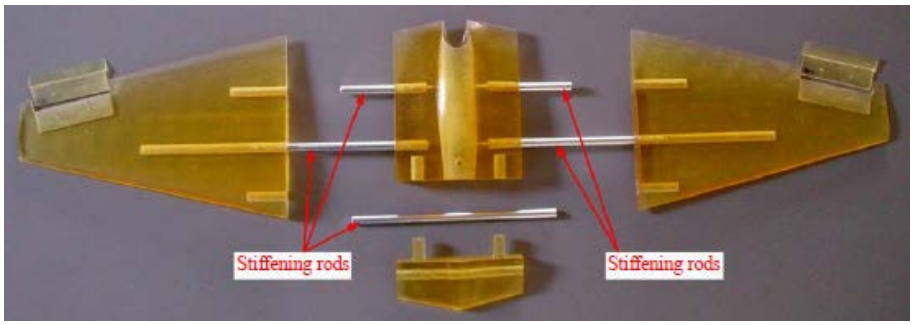

(a)

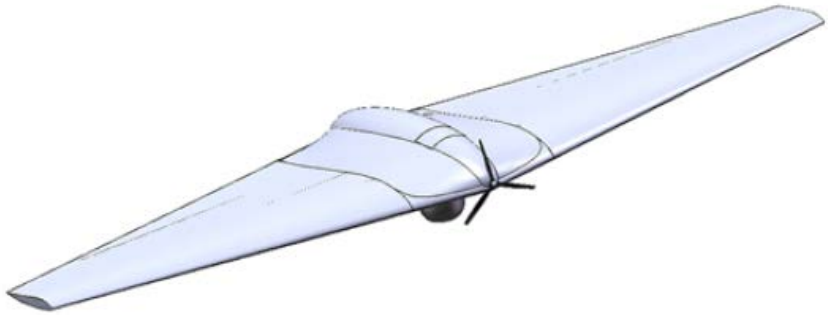

(b)

Figure 2-4: ILAS, a low-altitude observation aircraft (a) wind tunnel model (b) CAD rendering.

Constructing the model in pieces also allowed manufacturing of control surfaces such as ailerons, elevators, and spoilers as separate pieces as shown in Figure 2-3 (a). This also provided the opportunity to test aerodynamic behavior of the aircraft with the pitch and roll control surfaces actuated using a single wind tunnel model.

Heyes et al. [12], Tyler et al. [13], and Shun et al. [14] discuss the benefits of RP models because of the ability to build in internal features that would otherwise not be possible using CNC machining. These internal features can be used to embed instrumentation directly into the model. Tyler tested two models at the Air Force Research Laboratory, the UCAV X-45A and the Striker Tanker. Both contained internal features that allowed the insertion of a balance block,

pressure scanning module, and pressure tap instrumentation, and device for detecting model contact under load. Shun created a NACA 63-421 airfoil section by RP from three main sections which were provided with tongue and groove features to assist in accurate location of adjacent components during assembly. The wind tunnel model contained an Air Jet Vortex Generator (AJVG), which was used to modify the flow over the airfoil for flow diagnostics by injecting air into it. CAD model of AJVG equipment, shown in Figure 2-5, requires the provision for complex plumbing for supply of air and pressure measurement equipment inside of the wind tunnel model. This equipment was housed inside the leading edge section of the wind tunnel model as illustrated in Figure 2-6. According to these studies, the capabilities of the RP techniques used were ideally suited for manufacturing of wind tunnel models with internal features.

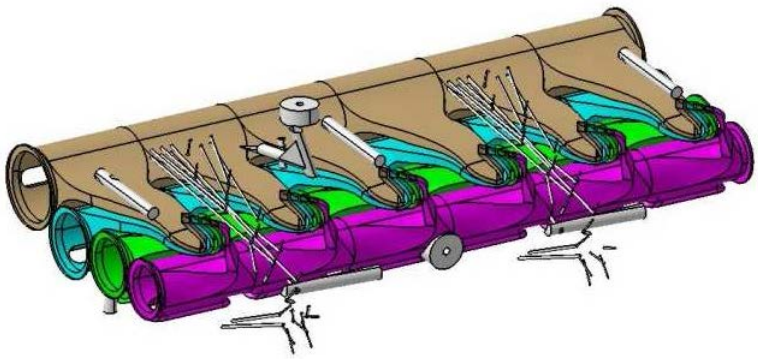

Figure 2-5: CAD model of AJVG [13]

Figure 2-6: Wind tunnel model of NACA 63-421 with internal features for AJVG

Working at KNT University of Technology in Tehran, Iran, Afhanajafi et al. [15] produced four wing-body-tail configuration models shown in Figure 2-7 from aluminum and using SLA, SLS, and FDM RP techniques. The models were constructed as a single part and nose section was separated and machined to install an aluminum balance adapter at the center of body. The nose was then reattached to the body. The models were tested at Mach numbers of 0.3, 0.8, 1.05, 1.2 and angles of attack between -5 and 20 degrees. The results of the aluminum and SLA models showed good agreement until about 12 degrees when they started diverging due to SLA model bending under higher loading. The SLS model tested did not match the aluminum model results as well as the FDM and SLA models. The greatest difference between the aluminum model and the RP models at high Mach numbers was in the axial force, where the axial force coefficient was slightly higher than that of the aluminum model at all angles of attack. In general, at subsonic Mach numbers, the majority of configurations started diverging at about 10 to 12 degrees angle of attack due to the higher loads. Therefore, the strength of the material is a factor because it caused deflection in RP models especially at higher Mach numbers. The effect of the rough surface finish of the RP models was also determined by adding grit to the aluminum model to make the surface rougher to see if it would make the aerodynamic characteristics agree better. The rougher surface had a big effect on the axial force, but not on the pitching and normal force coefficients. The rougher aluminum model had better agreements with RP models, showing that surface roughness of the models does affect the aerodynamic characteristics of the model. The higher axial force can also be explained by higher drag coefficient caused by the roughness of the RP models.

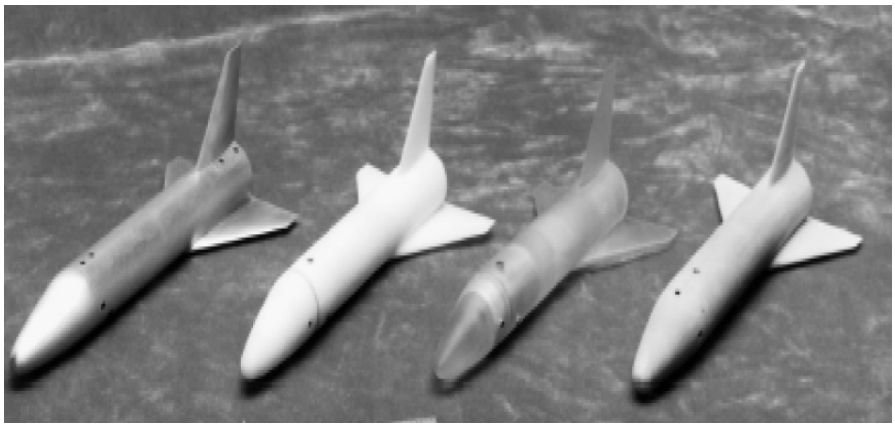

Figure 2-7: Wing-body wind tunnel models (left to right), aluminum, FDM-ABS, SLA, and SLS [15]

The same group also investigated the effect that the layer thickness of RP models has on aerodynamic coefficients of the same model geometry. Stereolithography was used to build models with the following layers thicknesses and horizontal resolution: 0.05mm vertically and 0.1µm (Ra) horizontally, 0.125mm vertically and 0.22µm (Ra), and 0.15mm vertically and 4.6µm (Ra) horizontally. They were tested in Mach range of 0.3 – 0.9 and angle of attack range of -2 deg to +12 deg. This tested the effect that surface roughness has on aerodynamic characteristics. The results showed that layer thickness did have an effect on the aerodynamic characteristics. The data for the three models differed by 5% or less. This difference was more visible at lower Mach numbers and higher angle of attacks [16].

In a different study, this group investigated the effect of electroplating an FDM model in an attempt to get results that were closer to a model created using conventional machining processes. Unfortunately, this did not work and electroplating had little effect on the aerodynamic characteristics except for axial force [17].

Similar work was performed by Zhou et al. [18] where electrochemical deposition (ED) was used to coat SLA components with nickel. Figure 2-8 shows electrodeposited pieces of the airfoil

wind tunnel model. However, their motivation was different; it was to strengthen the model. They concluded that electrodeposited nickel coating resulted in increased Young's modulus, ultimate tensile strength (UTS), flexural modulus and strength. These improvements can allow the fabrication of more functional RP models.

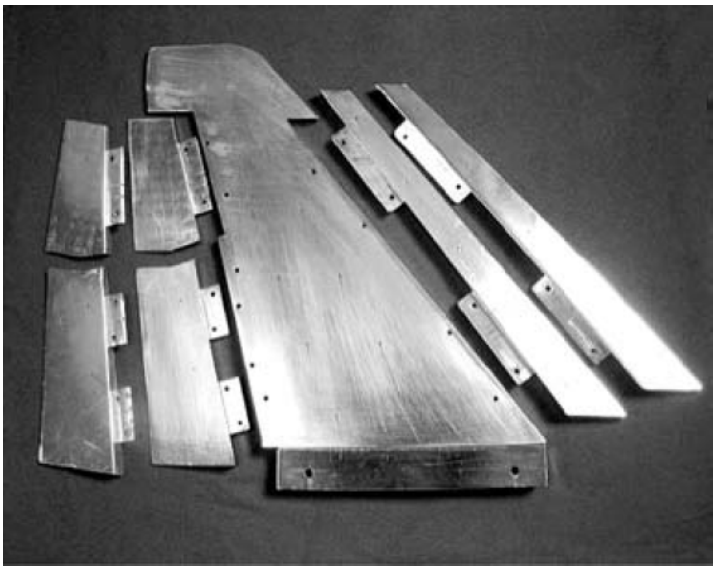

Figure 2-8: Electrodeposited airfoil wind tunnel model [18]

Studies conducted at NASA Langley Research Center by Danehy and Alderfer et al. [28, 29] used RP wind tunnel models created with SLA to visualize flow over the models in a hypersonic wind tunnel. The tests were run at Mach 10 speed and since a lot of heating is produced at that speed, the models had to be coated with heat resistant materials and the test durations were kept short. In addition to the quick fabrication times, another advantage of using these models was that internal ducting could be built into the model and used to channel a tracer gas that was then injected into the flow field. Two different models were tested. One was an inflatable re-entry vehicle experiment (IRVE) which is a sphere-cone with a 60 degree half angle seen in Figure 2-9 (a). The diameter of the model was 2 inches. The other model was of an Orion crew exploration vehicle (CEV) seen in Figure 2-9 (b). It was a 5 inch diameter model. Even though

some models were damaged after a single short tunnel run, about half of them did survive and produced meaningful results showing that RP models are resilient enough to withstand hypersonic flow when coated with heat resistant materials.

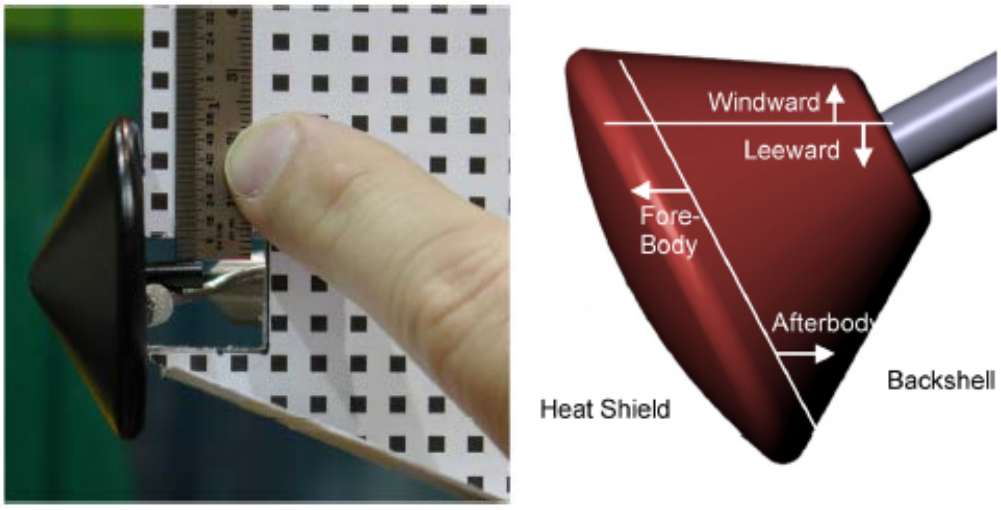

(a) **(b)**

Figure 2-9: Wind tunnel models of (a) IRVE and (b) CEV[28]

Dedoussis et al. at the Laboratory of Thermal Turbomachines at National Technical University of Athens, Greece used SLA to demonstrate that RP components can be used to make a cascade of 2 ½-D blades, with NACA 65-12(A10)10 profile sections for aerodynamic experimental investigations to simulate flow conditions through compressor blades. It was estimated that manufacturing the components with CNC milling would be about two to three times more expensive than fabricating them with the SLA techniques that were used. The cascade was installed and tested in an educational aerodynamic test rig. The orientation of the aerodynamically important surfaces were built perpendicularly to the SLA machine's platform, resulting in a surface finish roughness of 3-4μm, which is effectively 'aerodynamically smooth'. Experimental measurements agreed with the numerical calculations made for two incidence

angles, concluding that SLA RP models were reliable alternatives for wind tunnel testing of compressor blades [30].

Aghanajafi et al. more recent work has involved creating assembled wind-tunnel models that consist of both RP pieces and conventional CNC machined pieces as shown in Figure 2-10 [31]. The RP nose of the missile wind tunnel model was manufactured using a three-dimensional printing (3DP) technology which is developed by Z-Corporation. Although this technology offers some advantages over other RP technologies, like speed, low material cost, and wide range of colors, the worse surface roughness and lower mechanical properties make it a less suitable RP technology for wind tunnel models. This group concluded that wind tunnel models that incorporate both RP components made with 3DP and conventional metal components can be used for initial baseline aerodynamic database development. However, due to slight deviation especially at larger Mach numbers and greater angles of attack, they recommended using conventional wind tunnel models.

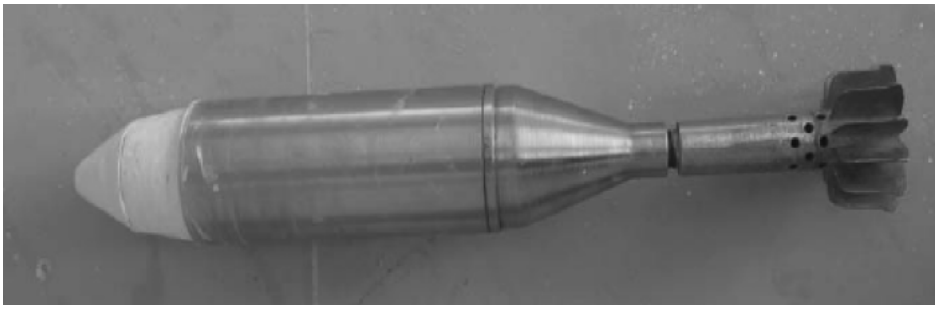

Figure 2-10: Steel model of missile with 3DP nose [31]

2.2.1 Rapid Prototyping for Aeroelastic Wind Tunnel Models

In 2011, an aeroelastic model of a wing box was created by Zhu et al., at the State Key Laboratory of Manufacturing Systems Engineering at Jiatong University in China, using a RP technique employing SLA [19]. A wing box is an aluminum structure, consisting of skins, ribs,

webs and strings shown in Figure 2-11 below. The model was never tested in a wind tunnel; rather, it was scaled to insure structural similarity and tested to determine the natural modes of the model. In this particular case, the research team used the low stiffness of the SLA material as an advantage to create a flexible model.

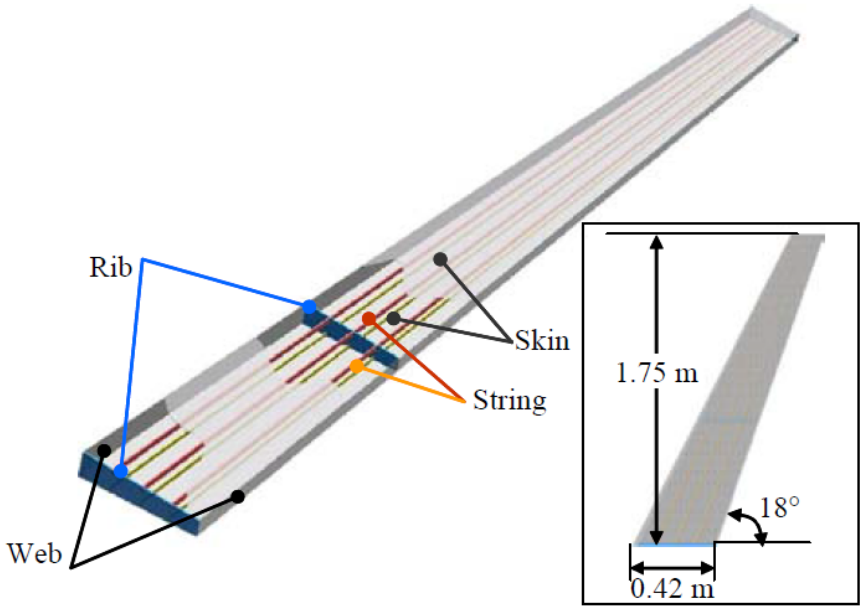

Figure 2-11: A wing box structure [19]

The CAD rendering and RP manufactured model are shown in Figure 2-12. The model had to be printed at a 15 degree angle with supports due to the limitation of the layered build. Although the models were not tested in a wind tunnel, results that were acquired using a laser-vibration-measuring apparatus showed an agreement between the wing-box prototype and model natural frequency with about a 1% error. [19].

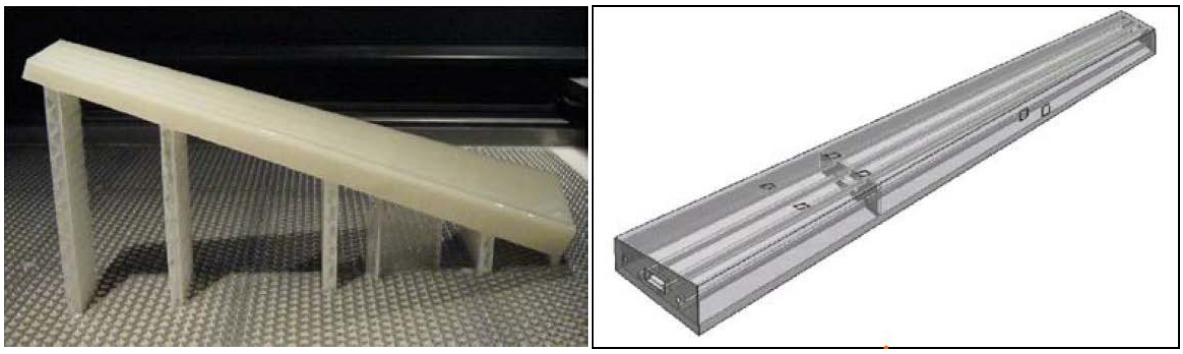

(a) (b)

Figure 2-12: (a) SLA model of the wing box (b) CAD model of the wing box

Wang et al. has created a novel method for preparing static aeroelastic prototypes by attaching panels manufactured by SLA to a metallic structure [32]. The stiffness similarity principle was used to achieve the desired stiffness distribution using the metal and resin structure to model the full scale aircraft. Wind tunnel testing at Mach number ranging from 0.4 to 0.65 and stiffness measurements using photogrammetry demonstrated that the novel method is both practical and feasible.

2.2.2 Polyjet Printing for Wind Tunnel Models

PP has been previously used by several groups to manufacture wind tunnel models. Kroll et al. created the wind tunnel model of the CERBERUS airplane, which was previously mentioned in this chapter, using an Objet printer. The model was printed using the VeroBlue material. The study was done at the Technion – Israel Institute of Technology in Haifa, Israel, where the models were manufactured. Udroiu et al. at the Transilvania University of Brasov in Romania has also successfully employed PP to fabricate wind tunnel models of an NACA airfoil [20, 21] and a self-balancing electric scooter [22]. The models were printed using an Objet EDEN 350 printer using the transparent FullCure 720 material.

In both PP cases, the models were fabricated using a single material and were not multi-material models. Both of the materials used in these two studies were hard plastics. Even though several groups have studied aeroelastic behavior in wind tunnel models, it was done with models manufactured using the SLA technique which uses a photopolymer that hardens during the manufacturing process, but has a low stiffness, exhibiting aeroelastic behavior. A thorough review of literature did not turn up testing of multi-material wind tunnel model for the purpose of observing aeroelastic behavior.

2.3 ADEPT Aerodynamic Decelerators

The ADEPT structure that is being investigated is a mechanically deployable aerodynamic decelerator which is employed in NASA's Adaptive Deployable Entry and Placement Technology (ADEPT), currently under development for landing missions on Mars and Venus [33, 34]. ADEPT was conceived to replace technology currently being used for landing missions on Mars, called Entry, Descent, Landing (EDL) technology. EDL relies on an aeroshell for entry into the Martian atmosphere, a parachute for deceleration, and rocket propulsion for slowing down just before landing. EDL has been used for Mars landers since the 1970s when it was developed for the Viking missions. Because this technology has a 1.2 metric ton (mT) weight capacity limit, new technologies, such as ADEPT, are being researched to land larger payloads for future robotic and human exploration which are estimated to have a 40 mT landing weight. In addition, this technology is also being considered for landing the Venus Intrepid Tessera Lander (VITaL) on Venus. The ADEPT-VITaL technology is a spinoff from the ADEPT Ballistic for Robotic Mars. Figure 2-13 shows the planned timeline for the development of the ADEPT technology [35].

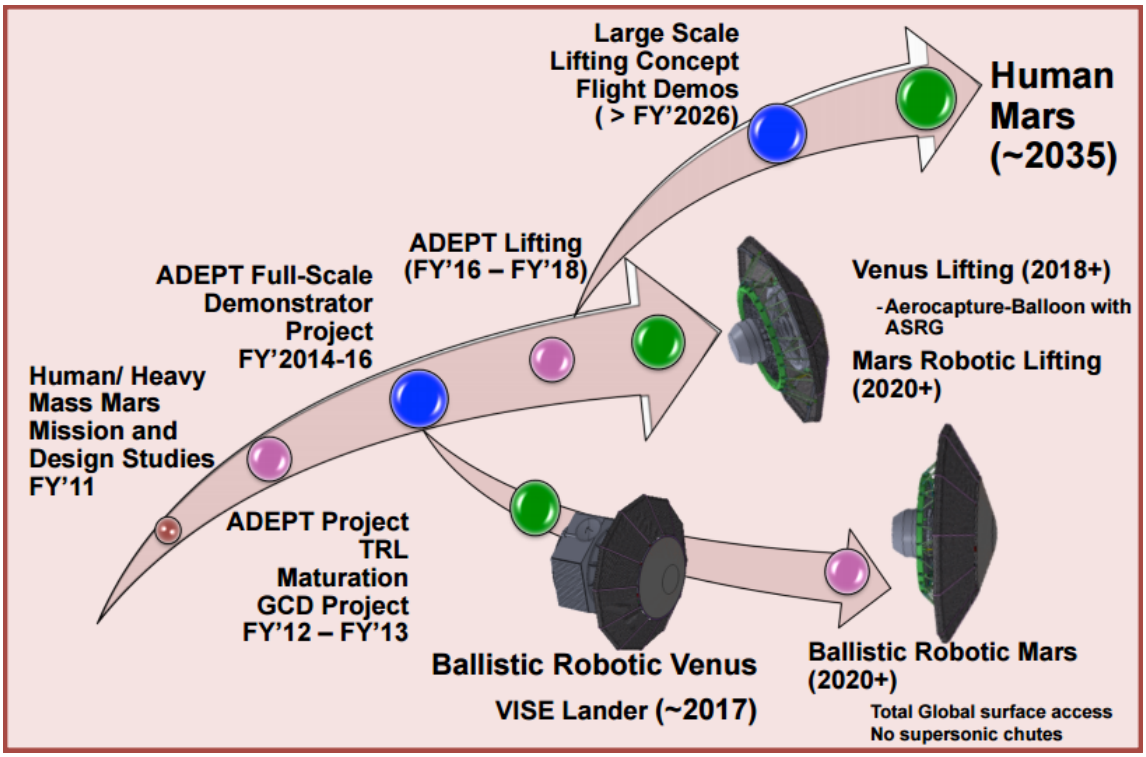

Figure 2-13: Planned timeline for development of different ADEPT concepts [35].

ADEPT employs an umbrella-like rib and strut mechanism covered with a flexible carbon fabric which is stiffened by ribs. The structure is stowed in the closed configuration in the payload shroud during the launch. This mechanism is then deployed in earth orbit to form a blunted spherical cone structure to be used as the decelerator and heat shield during entry into the atmosphere and descent. The ADEPT-VITaL decelerator is depicted in the deployed configuration in Figure 2-14 [36].

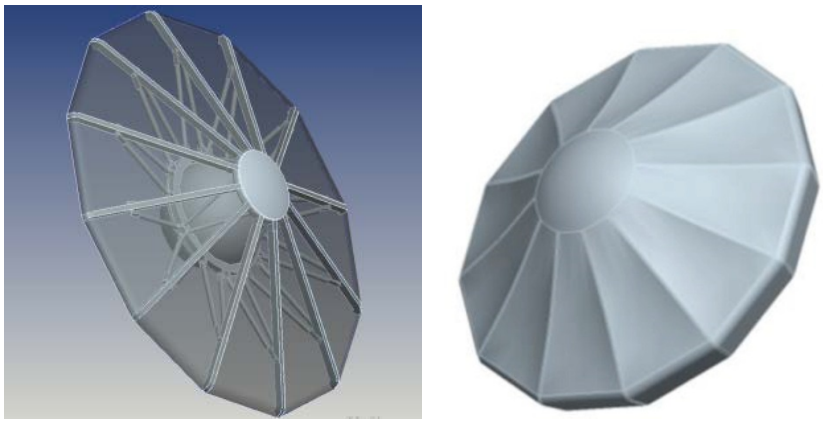

Figure 2-14: ADEPT decelerator [36].

The carbon cloth vanes of the ADEPT decelerator are shown in Figure 2-15 [35, 36].

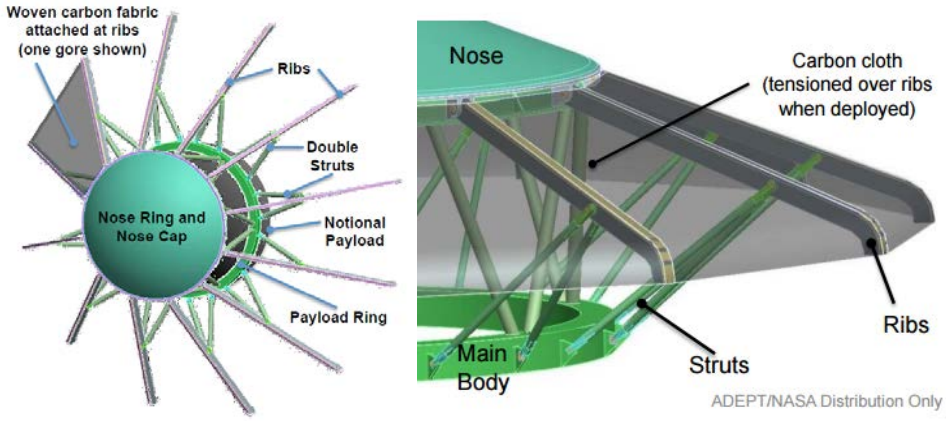

Figure 2-15: ADEPT Venus-VITaL decelerator structure with woven carbon fabric [35, 36]

The ADEPT decelerator is shown in the stowed configuration in Figure 2-16 [35].

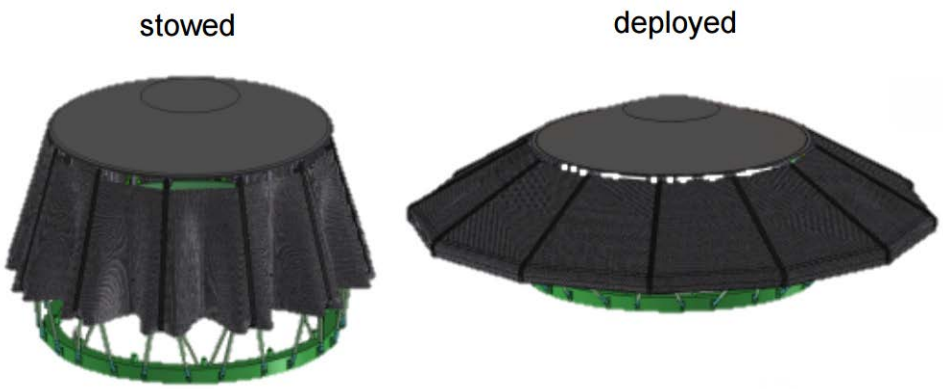

Figure 2-16: ADEPT Venus-VITaL decelerator in stowed and deployed configuration [35].

As can be seen from Figure 2-13, there are a number of Mars and Venus ADEPT decelerator concepts which vary in size and structure (number of ribs and panels). The Venus-VITaL and Mars-MELs robotic mission decelerators are smaller than the decelerator concepts for the human mars mission. The Venus-VITaL decelerator is 6 meters in diameter, while the MELs concept which is based off of it is between 5 and 15 meters in diameter. Both of these decelerators have 12 ribs and panels. The decelerator concepts for the human mars mission are between 23 and 44 meters in diameter and have 16, 24, or 32 ribs and panels.

Because part of the structure is flexible, its aeroelastic behavior is of interest. A scaled wind tunnel model can be used to determine the aeroelastic behavior that the full scale ADEPT decelerator will exhibit.

2.4 Aerodynamic Data of Similar Known Geometry

The spherically blunted cone shape which is used to construct the decelerator is a commonly used geometry for non-winged re-entry vehicles, such as probes and capsules. Some were constructed for space missions while many more were tested as prototypes, but never built because their projects were cancelled. Therefore, a lot aerodynamic data

has been collected for this type of geometry. The two VIKING spacecrafts, which were successfully landed on Mars in the mid-1970's, are one of the types of vehicles that were tested extensively and for which an abundance of aerodynamic data has been previously collected. The geometry of the entry module is illustrated in Figure 2-17 [37]. Its aeroshell is a spherically blunted nose cone with a semi-apertural angle of 70 degrees.

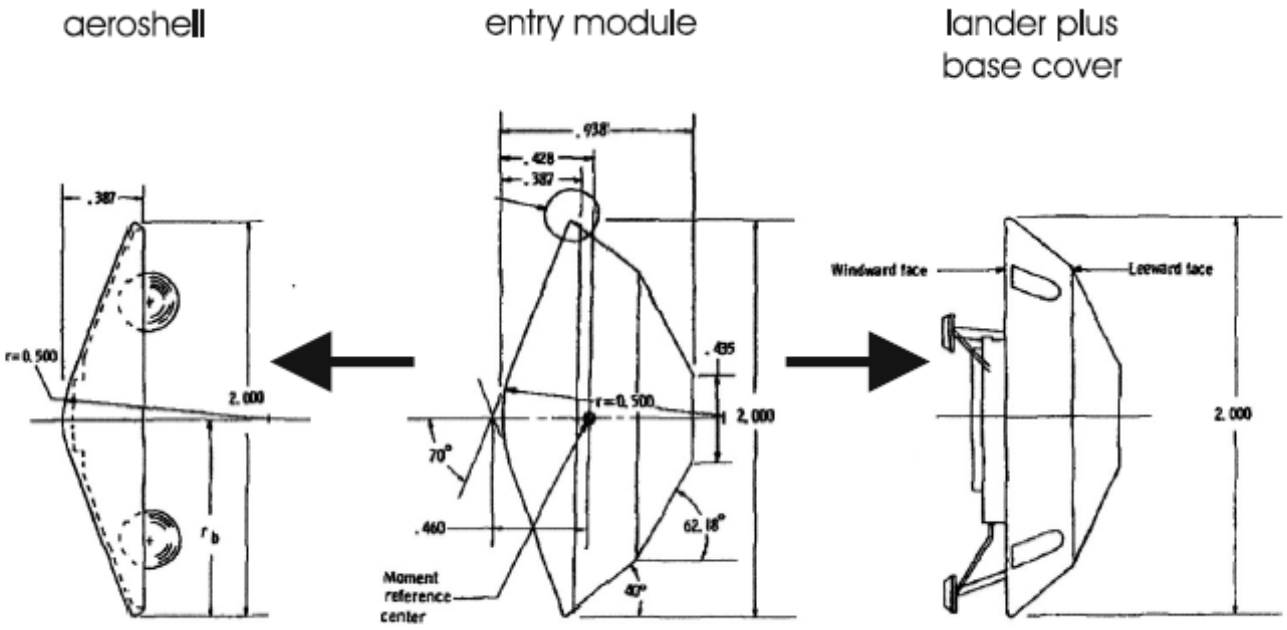

Figure 2-17: VIKING's entry module (middle) is composed of the aeroshell (left) and the lander plus base cover part (right) (dimensions in meters)

The aerodynamic data of the Viking entry module is shown in Figure 2-18 [37].

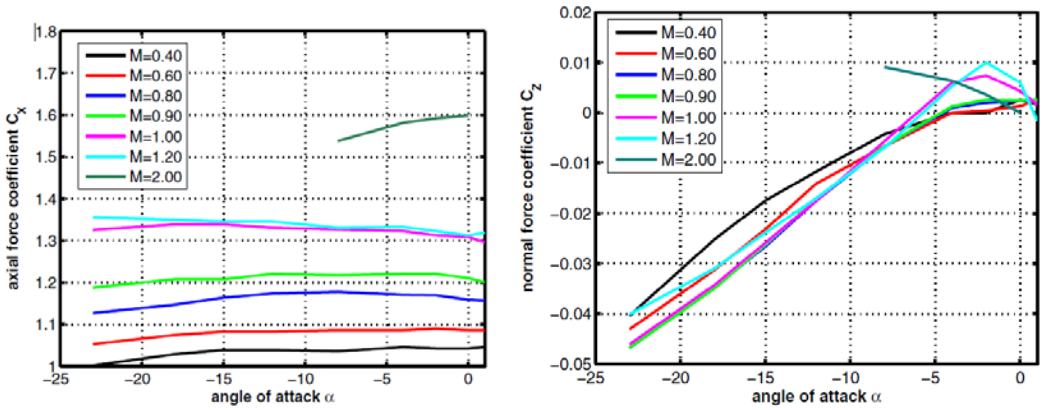

(a) (b)

Figure 2-18: (a) VIKING entry module axial force coefficient versus angle of attack. (b) VIKING entry module normal force coefficient versus angle of attack [37].

The axial force coefficient is the same as the drag force coefficient at 0° angle of attack. The values of interest which are relevant to the experiment in this thesis are Mach 0.40 because the testing was performed at lower Mach numbers. We expect the values of the drag force coefficient for similar geometry to be about 1 or even smaller.

2.5 Aeroelasticity and Similitude

The term aeroelasticity is used to describe an important class of aerodynamic problems in aircraft design. Aeroelasticity addresses the interaction between aerodynamic, inertial, and elastic forces on an elastic body that is exposed to fluid flow [38]. Aeroelasticity includes a number of phenomena which can be grouped into two separate categories: static and dynamic. Static phenomena involve interactions between aerodynamic and elastic forces, while dynamic phenomena involve interactions between inertial, aerodynamic, and elastic forces [39].

Static aeroelastic behavior in the aerodynamic decelerator structure manifests itself in the deflection of the flexible vanes of the multi-material aerodynamic decelerator under the

aerodynamic forces. The change in geometry due to the deflection could have an effect on aerodynamic properties, e.g. drag and lift coefficients.

Flutter is the most common dynamic aeroelastic phenomenon which is studied when determining an aircraft's performance because of the risk of structural failure. Flutter is the dynamic instability that occurs in an aircraft in flight, at a speed called flutter speed, where the structure's elasticity plays a big part in the instability. Scaled models of aircraft are typically built and tested in wind tunnels to test the iterations of a design for flutter. The multi-material model of the aerodynamic decelerator was observed in this thesis to see if flutter could be detected.

Similitude conditions need to be met in order to extrapolate the results of the tests on the model to the full scale aircraft. Similitude for aeroelastic models is nontrivial. References list a large number of possible non-dimensional similitude parameters and point out the impossibility of matching all of them [40, 41].The following flow, structural, and aerodynamic non-dimensional parameters will be considered in this work [40, 41].

2.5.1 Flow Parameters

1. Reynolds number, $Re = \frac{\rho_f V l}{\mu}$, is the ratio of inertial forces to viscous forces for a given flow condition, where ρ_f is the mass density of fluid (kg/m^3), V is the velocity (m/s), l is the length (m), and μ is the absolute viscosity (N·s/m^2).

The Reynolds number of the airflow around the aircraft typically cannot be matched by the airflow conditions in the wind tunnel; it is much lower than that of the aircraft at flight altitude. According to Bisplinghoff et al. and Lambourne et al., the change of Reynolds number has little effect on the oscillatory air forces which cause flutter as long

as the Reynolds number is above 4 x 10^5. Flutter speed and frequency is relatively unaffected by Reynolds numbers variations [41, 42].

2. Mach number, $M = \frac{V}{V_{sound}}$, is the ratio of V, velocity of the vehicle, to V_{sound}, the velocity of sound in the medium in which the aircraft is flying.

The Mach number is used to measure a fluid's compressibility effects. This parameter needs to be considered for similitude only in transonic and supersonic flow, so it needs to be matched if M > 0.3 at any location in the flow. If M < 0.3, the flow is considered incompressible and the Mach number need not be matched.

2.5.2 Structural Parameters

The following non-dimensional parameters taken from [40, 41] are derived by nondimensionalizing the equations of motion. Their derivations are shown in section 2.6.

3. Aeroelastic-bending parameter, $\frac{EI}{\rho_f V^2 l^4}$, where EI is the bending stiffness ($N \cdot m^2$) of the structure.

The bending stiffness may be determined using the formula, $M = EI'(d\theta/dx)$, where M is the bending moment and $d\theta/dx$ is the resulting change in slope per unit length of the structure in the x-direction. The aeroelastic-bending parameter should be matched if structural bending is expected.

4. Aeroelastic-torsion parameter, $\frac{\kappa_\theta G}{\rho_f V^2 L^4}$ where $\kappa_\theta G$ is the torsional stiffness ($N \cdot s/m^2$) of the structure.

The torsional stiffness may be determined using the formula, $T = \kappa_\theta G(d\gamma/dx)$, where T is the twisting moment and $d\gamma/dx$ is the resulting change in angle of twist per unit length of the structure in the x-direction. The aeroelastic torsion parameter should be matched if structural twist is expected.

5. Relative mass density factor, $\frac{m}{\rho_f l^3}$, is the ratio of structural density, m/l^3 or ρ_s, to mass density of fluid, ρ_f.

Relative mass density factor is derived from the force equations. This parameter should be matched if any translational vibration behavior is expected.

6. Relative mass moments of inertia, $\frac{I}{\rho_f l^5}$, is the ratio of $I = \int \rho_s r^2 dV$, the mass moment of inertia (kg·m^2), to $\rho_f l^5$, where r is the distance to the axis of rotation, ρ_s is the density of the solid integration is over the volume, V.

This parameter should be matched if any rotational vibration is expected.

7. Structural damping parameter, δ.

This parameter is listed as one of the parameters that needs to be matched in reference [41], but not [40] signifying that the damping of the material may not be as important as matching the other parameters. In addition to this, according to reference [41], the structural damping parameter typically does not have a big impact on flutter as long as the model parameter does not greatly exceed the full scale value. The structural damping parameter is beyond the scope of this study because damping characteristics of the material used for the model are unknown.

2.5.1 Aerodynamic Parameters

If the similitude parameters of the model and aircraft are matched, it can be inferred that the full scale aircraft will experience the following non-dimensional values that are similar to the measured values of the model under test in a wind tunnel.

8. Aerodynamic drag coefficient, $C_D = \frac{F_D}{0.5A\rho_f V^2}$, where F_D is the drag force, A is the characteristic frontal area of the model, and V is the flow velocity. The aerodynamic drag coefficient is a measure of the time average drag experienced.
9. Aerodynamic lift coefficient, $C_L = \frac{F_L}{0.5A\rho V^2}$, where F_L is the lift force. The aerodynamic lift coefficient is a measure of the time average lift experienced.
10. Strouhal number, $St = \frac{\omega l}{V}$, is used to describe the frequencies that are present in the time resolved periodic motion of the structure.

2.6 Nondimensionalization of Equations of Motion

In this section, the structural nondimensional parameters that were listed in the previous section are derived from the equations of motion for the following simple cases: bending beam, torsion, flat plate, and membrane.

2.6.1 Bending Beam

The governing differential equation of motion for forced vibrations of a uniform cross-section beam in cross flow illustrated in Figure 2-19 is

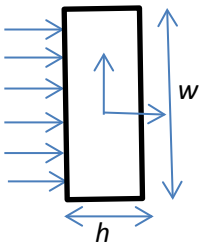

Figure 2-19: Cross-section of a uniform rectangular beam in cross flow

$$EI\frac{\partial^4 u}{\partial x^4}+\rho_L\frac{\partial^2 u}{\partial t^2}=\frac{1}{2}\rho_f V^2 w \tag{1}$$

where *EI* is the flexural rigidity (*E* is Young's modulus of the linearly elastic material, and *I* is the area moment of inertia), *u(x,t)* describes the displacement of the beam along its length with respect to time, ρ_L is the material density per unit length of the beam, $\frac{1}{2}\rho_f V^2 w$ is the dynamic pressure per unit width of the beam (ρ_f is the fluid mass density, *V* is the flow velocity, and *w* is the width of the beam) [43] section 4.1.

To nondimensionalize the governing equation, the nondimensional variables u^*, x^*, and t^* are defined:

$$x^*=\frac{x}{L} \tag{2}$$

$$u^*=\frac{u}{L} \tag{3}$$

$$t^*=\frac{t}{(L/V)} \tag{4}$$

where *L* is the length scale and *V* is velocity. These relations can be used to transform each parameter of the differential equation to use the nondimensional variables. The term $\partial^4 u/\partial x^4$ becomes:

$$\frac{\partial^4 u}{\partial x^4} = \frac{\partial^4 u}{\partial x^4}\left(\frac{1}{L}\frac{\partial x}{\partial x^*}\right)^4 \tag{5}$$

$$\frac{\partial^4 u}{\partial x^4} = \frac{1}{L^4}\frac{\partial^4 u}{\partial x^{*4}} \tag{6}$$

$$\frac{\partial^4 u}{\partial x^4} = \frac{1}{L^4}\frac{\partial^4 \left(Lu^*\right)}{\partial x^{*4}} \tag{7}$$

$$\frac{\partial^4 u}{\partial x^4} = \frac{1}{L^3}\frac{\partial^4 u^*}{\partial x^{*4}} \tag{8}$$

The term $\partial^2 u/\partial t^2$ becomes:

$$\frac{\partial^2 u}{\partial t^2} = \frac{\partial^2 \left(Lu^*\right)}{\partial t^2}\left(\frac{\partial t}{\left(L/V\right)\partial t^*}\right)^2 \tag{9}$$

$$\frac{\partial^2 u}{\partial t^2} = \frac{V^2}{L}\frac{\partial^2 u^*}{\partial t^{*2}} \tag{10}$$

Substituting the nondimensionalized terms back into the equation gives:

$$\frac{EI}{L^3}\frac{\partial^4 u^*}{\partial x^{*4}} + \frac{\rho_L V^2}{L}\frac{\partial^2 u^*}{\partial t^{*2}} = \frac{1}{2}\rho_f V^2 w \tag{11}$$

Since the width of the geometry scales with the length, the width, *w*, can be replaced with L, the length dimension that is scaled. Dividing each term of the equation by $\frac{1}{2}\rho_f V^2 L$ produces the dimensionless form of the equation:

$$\boxed{\frac{EI}{(1/2)\rho_f V^2 L^4}\frac{\partial^4 u^*}{\partial x^{*4}} + \frac{\rho_L}{(1/2)\rho_f L}\frac{\partial^2 u^*}{\partial t^{*2}} = 1} \tag{12}$$

with the nondimensional bending stiffness parameter, $\frac{EI}{\rho_f V^2 L^4}$, and inertia in bending parameter, $\frac{\rho_L}{\rho_f L^2}$.

2.6.2 Torsion

The governing differential equation of motion for forced torsional vibrations of a uniform cross-section beam in cross flow illustrated in Figure 2-20 is

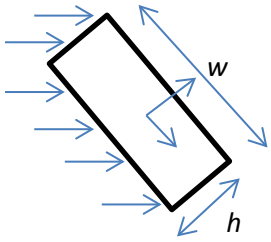

Figure 2-20: Cross-section of a uniform rectangular beam in cross flow

$$\kappa_\theta G \frac{\partial^2 \theta}{\partial x^2} - \rho_s J_p \frac{\partial^2 \theta}{\partial t^2} = m_t \tag{13}$$

where $\kappa_\vartheta G$ is the torsional rigidity [43] section 3.2. κ_ϑ is a torsional stiffness coefficient which depends on the geometry of the cross section. κ_θ can be determined using the St Venant's stress function model, where

$$\kappa_\theta = \iint_A \Psi(x,y) dx dy \tag{14}$$

where Ψ(y,z) is the stress function [44]. For example, a rectangular cross section has

$$\kappa_\theta \approx w h^3 \left[\frac{1}{3} - 0.21 \frac{h}{w} \left(1 - \frac{h^4}{12 w^4} \right) \right] \tag{15}$$

G is the shear modulus, $G = E/2(1+\nu)$, ρ_s is the volume mass density, and J_p is the polar area moment of inertia of the cross section. J_p is defined as

$$J_p = \int_A (x^2 + y^2) dA \tag{16}$$

For example, for a rectangular cross-section,

$$J_p = \frac{wh}{12}(w^2 + h^2) \tag{17}$$

m_t is the twisting moment per unit length that is determined by integrating the surface traction (that is, the force per unit area) crossed with the moment arm, r, around the perimeter of the section, P.

$$m_t = \int_P \left[\underline{r} \times \underline{T}\right] ds = rF_L \tag{18}$$

This could be simply expressed as F_L , the component of the equivalent force per until length that is orthogonal to r, the effective lever arm from the centroid of the cross-section to the location where the equivalent force is located. The expression for F_L is,

$$F_L = pw \tag{19}$$

where p is the dynamic pressure. The dynamic pressure can be expressed in terms of the fluid mass density and the velocity of the flow,

$$p = \frac{1}{2}\rho_f V^2 \tag{20}$$

Substituting equations (19) and (20) into (18) gives the following expression for the twisting moment per unit length, where we are assuming that the cross-sectional dimensions vary in the same ratio as the length, L,

$$m_t = \frac{1}{2}\rho_f V^2 L^2 \tag{21}$$

To nondimensionalize the governing equation, the nondimensional variable ϑ^* is defined:

$$\theta^* = \theta \tag{22}$$

ϑ^*, x^*, and t^* are substituted into the equation's terms,

$$\frac{\partial^2\theta}{\partial x^2} = \frac{\partial^2\theta^*}{\partial x^2}\left(\frac{1}{L}\frac{\partial x}{\partial x^*}\right)^2 \tag{23}$$

$$\frac{\partial^2\theta}{\partial x^2} = \frac{1}{L^2}\frac{\partial^2\theta^*}{\partial x^{*2}} \tag{24}$$

$$\frac{\partial^2\theta}{\partial t^2} = \left(\frac{V}{L}\right)^2\frac{\partial^2\theta}{\partial t^{*2}} \tag{25}$$

Substituting the nondimensionalized terms back into the equation gives:

$$\frac{\kappa_\theta G}{L^2}\frac{\partial^2\theta^*}{\partial x^{*2}} - \frac{\rho_s J_p V^2}{L^2}\frac{\partial^2\theta^*}{\partial t^{*2}} = m_t \tag{26}$$

Substituting (21) into (26) gives,

$$\frac{\kappa_\theta G}{L^2}\frac{\partial^2\theta^*}{\partial x^{*2}} - \frac{\rho_s J_p V^2}{L^2}\frac{\partial^2\theta^*}{\partial t^{*2}} = \frac{1}{2}\rho_f V^2 L^2 \tag{27}$$

Dividing each term of the equation by $\frac{1}{2}\rho_f V^2 L^2$ produces the dimensionless form of the equation:

$$\boxed{\frac{\kappa_\theta G}{(1/2)\rho_f V^2 L^4}\frac{\partial^2\theta^*}{\partial x^{*2}} - \frac{\rho_s J_p V^2}{(1/2)\rho_f V^2 L^4}\frac{\partial^2\theta^*}{\partial t^{*2}} = 1} \tag{28}$$

which contains the nondimensional torsional stiffness parameter, $\frac{\kappa_\theta G}{\rho_f V^2 L^4}$, and rotational inertia parameter, $\frac{\rho_s J}{\rho_f L^4}$.

2.6.3 Flat Plate

The governing differential equation of motion for forced vibrations of a uniform thickness plate in cross flow is

$$D\nabla^4 u + \rho_A \frac{\partial^2 u}{\partial t^2} = \frac{1}{2}\rho_f V^2 \tag{29}$$

where $D = Eh^3/12(1-\nu^2)$ is the flexural rigidity of the plate, *u(x,y,t)* describes the displacement at different locations on the plate with respect to time, and ρ_A is the material density per unit area of the plate [43] section 6.1.

Expanding the expression $\nabla^4 u$:

$$D\left[\frac{\partial^4 u}{\partial x^4} + 2\frac{\partial^4 u}{\partial x^2 \partial y^2} + \frac{\partial^4 u}{\partial y^4}\right] + \rho_A \frac{\partial^2 u}{\partial t^2} = \frac{1}{2}\rho_f V^2 \tag{30}$$

To nondimensionalize the governing equation, the nondimensional variables u^*, x^*, and t^* are defined:

$$x^* = \frac{x}{L} \tag{31}$$

$$u^* = \frac{u}{L} \tag{32}$$

$$t^* = \frac{t}{(L/V)} \tag{33}$$

Substituting the nondimensionalized terms back into the equation gives:

$$\frac{D}{L^3}\left[\frac{\partial^4 u^*}{\partial x^{*4}} + 2\frac{\partial^4 u^*}{\partial x^{*2}\partial y^{*2}} + \frac{\partial^4 u^*}{\partial y^{*4}}\right] + \frac{\rho_A V^2}{L}\frac{\partial^2 u^*}{\partial t^{*2}} = \frac{1}{2}\rho_f V^2 \tag{34}$$

Substituting $\nabla^4 u^*$ back into the equation results in:

$$\frac{D}{L^3}\nabla^4 u^* + \frac{\rho_A V^2}{L}\frac{\partial^2 u^*}{\partial t^{*2}} = \frac{1}{2}\rho_f V^2 \tag{35}$$

Dividing each term of the equation by $\frac{1}{2}\rho_f V^2$ produces the dimensionless form:

$$\boxed{\frac{D}{(1/2)\rho_f V^2 L^3}\nabla^4 u^* + \frac{\rho_A}{(1/2)\rho_f L}\frac{\partial^2 u^*}{\partial t^{*2}} = 1} \tag{36}$$

where $\frac{D}{\rho_f V^2 L^3}$ is the flexural rigidity parameter and $\frac{\rho_A}{\rho_f L}$ is the inertia in bending parameter.

2.6.4 Membrane

The governing differential equation of motion for a membrane in cross flow is

$$T\nabla^2 u + \rho_A \frac{\partial^2 u}{\partial t^2} = \frac{1}{2}\rho_f V^2 \tag{37}$$

where $T = \sigma h$ is the tension, a product of residual stress and thickness of the membrane [43] section 5.1.

Expanding the expression $\nabla^2 u$:

$$T\left[\frac{\partial^2 u}{\partial x^2} + 2\frac{\partial^2 u}{\partial x\partial y} + \frac{\partial^2 u}{\partial y^2}\right] - \rho_A \frac{\partial^2 u}{\partial t^2} = \frac{1}{2}\rho_f V^2 \tag{38}$$

To nondimensionalize the governing equation, the nondimensional variables u^*, x^*, and t^* are defined:

$$x^* = \frac{x}{L} \tag{39}$$

$$u^* = \frac{u}{L} \tag{40}$$

$$t^* = \frac{t}{(L/V)} \tag{41}$$

Substituting the nondimensionalized terms back into the equation gives,

$$\frac{T}{L}\left[\frac{\partial^2 u^*}{\partial x^{*2}} + 2\frac{\partial^2 u^*}{\partial x^* \partial y^*} + \frac{\partial^2 u^*}{\partial y^{*2}}\right] + \frac{\rho_A V^2}{L}\frac{\partial^2 u^*}{\partial t^{*2}} = \frac{1}{2}\rho_f V^2 \tag{42}$$

Substituting $\nabla^2 u^*$ back into the equation results in:

$$\frac{T}{L}\nabla^2 u^* + \frac{\rho_A V^2}{L}\frac{\partial^2 u^*}{\partial t^{*2}} = \frac{1}{2}\rho_f V^2 \tag{43}$$

Dividing each term of the equation by $\frac{1}{2}\rho_f V^2$ produces the dimensionless form,

$$\boxed{\frac{T}{(1/2)\rho_f V^2 L}\nabla^2 u^* - \frac{\rho_A}{(1/2)\rho_f L}\frac{\partial^2 u^*}{\partial t^{*2}} = 1} \tag{44}$$

where $\frac{T}{\rho_f V^2 L}$ is the tension parameter and $\frac{\rho_A}{\rho_f L}$ is the inertial parameter.

2.6.5 Summary of Dimensionless Parameters

Table 2-1 summarizes the dimensionless stiffness and inertial parameters for the 4 geometries: bending beam, torsion, flat plate, and membrane.

Geometry	Stiffness Parameter	Inertial Parameter
Bending Beam	$\frac{EI}{\rho_f V^2 L^4}$	$\frac{\rho_L}{\rho_f L^2}$
Torsion	$\frac{\kappa_\theta G}{\rho_f V^2 L^4}$	$\frac{\rho_s J}{\rho_f L^4} = \frac{I}{\rho_f L^5}$
Flat Plate	$\frac{D}{\rho_f V^2 L^3}$	$\frac{\rho_A}{\rho_f L}$
Membrane	$\frac{T}{\rho_f V^2 L}$	$\frac{\rho_A}{\rho_f L}$

Table 2-2: Summary of dimensionless parameters

2.7 Scaling Procedure

When performing scaling for a simple example of an aeroelastic phenomenon such as flutter of a cantilever beam in bending, that is not subjected to torsion, the following nondimensional parameters, which were derived earlier, have to be matched for the full scale article and scaled model: M, Re, $\frac{EI}{\rho_f V^2 L^4}$, $\frac{\rho_L}{\rho_f L^2}$.

An aluminum cantilever beam illustrated in Figure 2-21 with a length of 2 meters, width of 0.5 meter, and height of 0.1 meter is traveling at a velocity of 100 m/s in air. The following derivation will go through an example of a procedure for this geometry and these conditions.

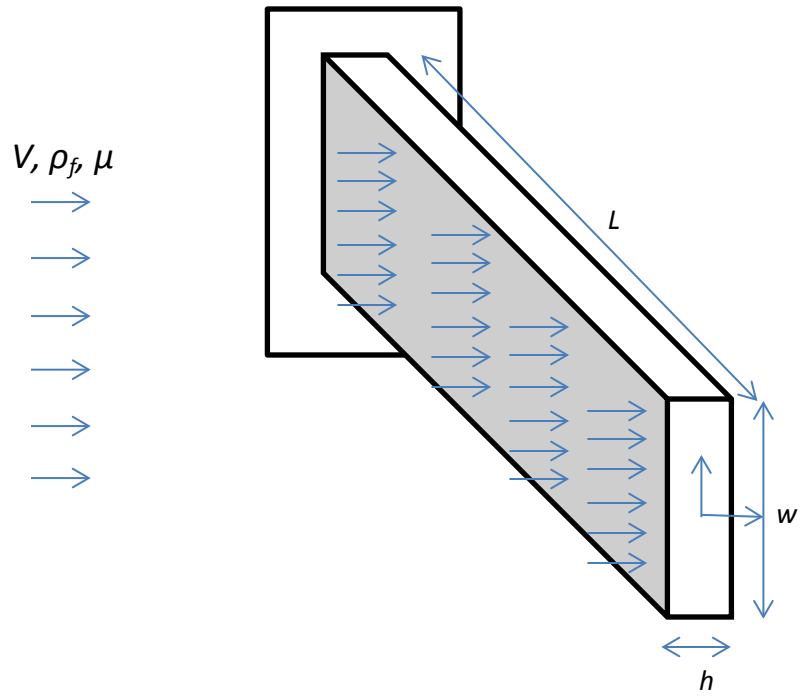

Figure 2-21: Cantilever beam in crossflow

The first step in a non-dimensional analysis is picking *n*, a length scale factor for the model. This is typically determined by the size of the wind tunnel that the model has to fit into for testing. If the length of the full scale article is 5 times the length of the model, the scaling factor is 1:5.

$$n = \frac{L_m}{L_{fs}} = \frac{1}{5} \tag{45}$$

For a full scale cantilever beam with a length of 2 meters, the scaled beam will have a length of 0.4 meters.

The next step is to match the Mach number, $M = \frac{V}{V_{sound}}$. We will assume that the full scale article is flown in air at an altitude very close to sea level which is the same as the altitude of the wind tunnel and at ambient temperature which is the same as the room temperature of the wind tunnel. This means that the velocity of sound, V_{sound}, is 343.2m/s.

The Mach number of the flow around the full scale article is

$$M = \frac{100\,m/s}{343.2\,m/s} = 0.29 \tag{46}$$

Mach number only needs to be matched if the flow around the full scale article or model is compressible. If the flow is incompressible (as in this example, where the full scale Mach number is less than 0.3), then it is not important to exactly match the Mach number; it is, however, required, that the Mach number remain below 0.3 so that the flow stays essentially incompressible [40]. If the velocity of the full scale article was to increase above 100m/s, Mach number would have to be matched

$$M_m = M_{fs} \tag{47}$$

which becomes

$$\frac{V_m}{V_{sound}} = \frac{V_{fs}}{V_{sound}} \tag{48}$$

Since the medium that the full scale article and the model are both in is air at the same temperature and similar static pressures, the velocity of sound V_{sound} is the same, which results in the following relationship

$$V_m = V_{fs} \tag{49}$$

Therefore, to match the Mach number, if the velocity of the full scale article is above 100m/s, the velocity of the flow around the model would have to be the same.

Now that we know that V_{fs} has a Mach number that is below 0.3, the velocity of the flow around the model can be varied as long as it stays below 100m/s.

The next step is to match the Reynolds number, $\frac{\rho_f V l}{\mu}$. Since we have assumed that the altitude and temperature of the full scale article is equal to that of the wind tunnel, the fluid mass density, ρ, and the dynamic viscosity, μ, of the air flow around the model and full scale article are the same.

$$\mathrm{Re}_m = \mathrm{Re}_{fs} \tag{50}$$

According to the definition of the Reynolds number

$$\frac{\rho_m V_m L_m}{\mu_{fs}} = \frac{\rho_{fs} V_{fs} L_{fs}}{\mu_m} \tag{51}$$

Substituting equation (45) into (51) results in

$$\frac{V_m \rho_m n}{\mu_m} = \frac{V_{fs} \rho_{fs}}{\mu_{fs}} \tag{52}$$

Velocity of the scaled model can be found by solving equation (52) for V_m

$$V_m = \frac{V_{fs} \rho_{fs} \mu_m}{n \rho_m \mu_{fs}} \tag{53}$$

Because we assumed that the fluid mass density and dynamic viscosity of the scale model is the same as the full scale article, we obtain

$$V_m = \frac{V_{fs}}{n} = 5 V_{fs} \tag{54}$$

Since the velocity of the full scale model is 100 m/s, the velocity of the flow in the wind tunnel must be 500 m/s in order to match the Reynolds number. This velocity has a Mach number of 1.46, so the flow is now supersonic and will exhibit many features such as shocks that would not be present in the full scale model. In other words, we have not been able to match

the Reynolds number. In order to prevent compressibility effects, the velocity has to be kept below approximately 100 m/s. In order to reduce the velocity at which the model is tested while still matching the Reynolds number, the fluid mass density and dynamic viscosity values can be changed. The fluid mass density of the flow around the full scale article can be lowered by flying it at a higher altitude where the air is thinner or the fluid mass density of the flow in the wind tunnel can be increased by pressurizing the wind tunnel. The dynamic viscosity of the flow can also be lowered through a cryogenic concept, where the air is replaced by a higher density-lower viscosity fluid which operates at lower temperatures. Because these techniques are very complex and expensive, many times it is not possible to match the Reynolds number of the model to the full scale article. In addition, according to Binsplinghoff et al. and Lambourne et al, the differences in Reynolds number has little effect on the oscillatory air forces which cause flutter as long as the Reynolds number is above 4 x 10^5 [41, 42]. So, it may not be necessary to match Re exactly either, although in the ideal case we would want to match both Re and Ma.

The Reynolds number of the flow around the full scale article is

$$\mathrm{Re} = \frac{\rho V_{fs} L_{fs}}{\mu} = \frac{1.23kg}{m^3}\frac{100m}{s}\frac{2m}{1}\frac{m \cdot s}{1.79\times10^{-5}kg} = 1.37\times10^7 \tag{55}$$

We can also use this value for the Reynolds number to find the lower limit of the velocity at which the model can be tested.

$$V_m = \frac{\mathrm{Re}\,\mu}{\rho L_m} = \frac{4\times10^5}{1}\frac{1.79\times10^{-5}kg}{m \cdot s}\frac{m^3}{1.23kg}\frac{1}{0.4m} = 14.6\,m/s \tag{56}$$

If the Reynolds number is greater than 4 x 10^5 and the velocity is greater than 14.6 m/s, a somewhat similar aerodynamic behavior and flutter may be achieved.

The next step is to match the bending stiffness parameter, $\frac{EI}{\rho_f V^2 L^4}$.

$$\frac{E_m I_m}{\rho_m V_m^{\ 2} L_m^{\ 4}} = \frac{E_{fs} I_{fs}}{\rho_{fs} V_{fs}^{\ 2} L_{fs}^{\ 4}} \tag{57}$$

Since the fluid mass density is the same, the expression simplifies to

$$\frac{E_m I_m}{V_m^{\ 2}} = \frac{E_{fs} I_{fs} \cdot n^4}{V_{fs}^{\ 2}} \tag{58}$$

The full scale cantilever beam is made out of aluminum, so its Young's modulus, E_{fs}, is 69 GPa. The model is manufactured by rapid prototyping, so there is a range of values for the Young's modulus depending on the material used. Stratasys Polyjet printer materials have a Young's modulus ranging from 1000 MPa to 3500 MPa. We will select a material with the highest, E_m, 3500 MPa. The moment of inertia for the full scale model is

$$I_{fs} = \frac{1}{12} w_{fs} h_{fs}^{\ 3} = \frac{1}{12}\left(0.5\frac{m}{s}\right)\left(0.1\frac{m}{s}\right)^3 = 4.17\times10^{-5}\, m^4/s^4 \tag{59}$$

According to the equation, since n=1/5, we need to pick the largest I_m, so a solid rectangular cross-section is chosen:

$$I_m = \frac{1}{12} w_m h_m^{\ 3} = \frac{1}{12}\left(0.1\frac{m}{s}\right)\left(0.02\frac{m}{s}\right)^3 = 6.67\times10^{-8}\, m^4/s^4 \tag{60}$$

The velocity of the flow around the model has to be lower in order to match the bending stiffness parameter. To find the velocity, we solve for V_m

$$V_m = \sqrt{\frac{E_m I_m V_{fs}^{\ 2}}{E_{fs} I_{fs} \cdot n^4}} = 22.17\, m/s \tag{61}$$

Using the velocity found in (61), the bending stiffness parameter for the model and full scale article can be calculated:

$$\frac{E_m I_m}{\rho_m V_m^{\,2} L_m^{\,4}} = \frac{E_{fs} I_{fs}}{\rho_{fs} V_{fs}^{\,2} L_{fs}^{\,4}} = 14.61 \tag{62}$$

The following plot shows the bending stiffness parameter versus the velocity of the flow for several RP materials with different modulus of elasticity:

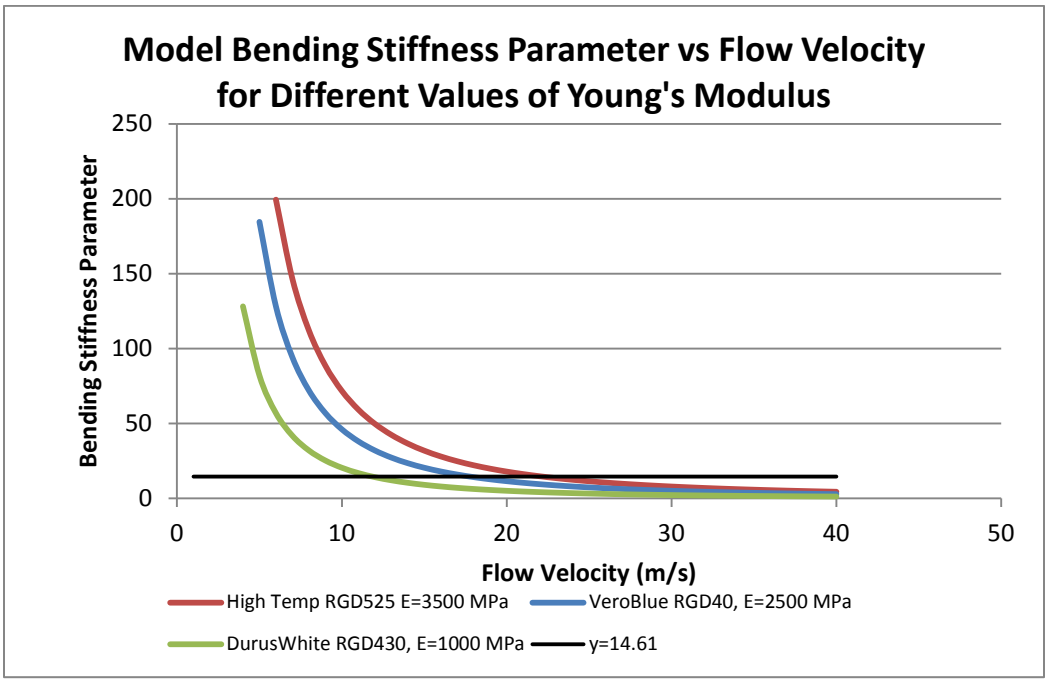

Figure 2-22: Model bending stiffness parameters for 3 different Stratasys PolyJet materials versus flow velocity and an intercepting line showing the velocity required to get a value of 14.61 for the parameter for each material.

Next, the inertia in bending parameter, $\frac{\rho_L}{\rho_f L^2}$, needs to be matched, where ρ_L is the density per unit length, or ρ times the cross sectional area of the beam, *A*. To find the inertial bending parameter of the full scale article, we use the density of aluminum 2700 kg/m^3 and cross sectional area, 0.05 m^2, to calculate the density per unit length of 135 kg/m.

$$\frac{\rho_{L,fs}}{\rho_{f,fs}L_{fs}^{\ 2}} = \frac{135kg}{m}\frac{m^3}{1.23kg}\left(\frac{1}{2m}\right)^2 = 27.44 \tag{63}$$

For the inertial bending parameter of the model, we use the density of the RP plastic used in Stratasys Objet printers which is 1170 kg/m^3 times the cross sectional area of 0.001 m^2.

$$\frac{\rho_{L,m}}{\rho_{f,m}L_{m}^{\ 2}} = \frac{1.17kg}{m}\frac{m^3}{1.23kg}\left(\frac{1}{0.4m}\right)^2 = 5.95 \tag{64}$$

The inertia in bending parameter of the full scale model is greater than that of the model by a factor of 4.61. The only way to match this parameter exactly would be to find a material with a higher density, which is not possible if manufacturing the model using a PolyJet printer because the density of conventional plastics does not get much higher than 2,000 kg/m^3. The density that is required to get an inertial parameter of 27.44 is approximately 5,400 kg/m^3 and the closest material to that is titanium with a density of 4500 kg/m^3. However, titanium has a Young's modulus much larger than required to match the bending stiffness parameter. A possible technique that is commonly used if a material with a lower density is required to match a dimensionless parameter is making the model hollow.

This exercise proves how difficult it can be to match all of the dimensionless parameters to obtain similitude. However, with some assumptions, it is possible to come within an order of magnitude.

3 Methods

In this chapter, the stiff and soft wind-tunnel models of the ADEPT decelerator are discussed, including their geometry and material properties. Next, the wind-tunnel setup and experimental procedure are reviewed.

3.1 Decelerator Model

For this investigation, two scaled models were manufactured using a Stratasys Objet Connex 500 multi-material 3D printer based on a CAD model obtained from NASA Ames Research Center. One of the benefits of creating a model using a multi-material printer is the ability to compare results between a flexible, multi-material, model and a rigid model made out of one stiff material with the identical geometry. This section will describe the geometry of the scaled models and their materials.

3.1.1 Geometry

A schematic of the decelerator model is depicted in Figure 3-1. It is a 60 degree cone with a spherically blunted nose. In the multi-material, soft, decelerator, the supporting structure, which includes the ribs, nose, and rim, is printed out of a stiff material, while the flexible vane, which models the flexible carbon fabric, is printed out of a flexible, rubber-like, material.

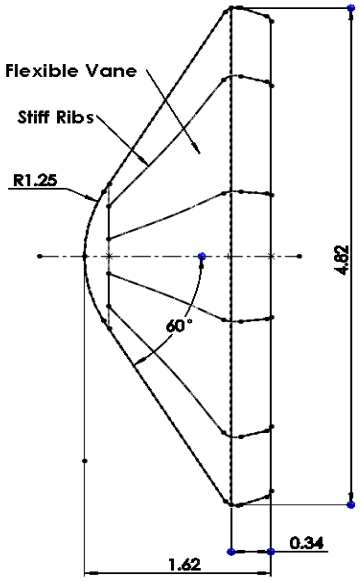

Figure 3-1: Schematic of decelerator model [inches].

A photo of the decelerator model is shown in Figure 3-2. A square post extends from the rounded nose and stiff ribs, which is used for mounting the model onto a rod.

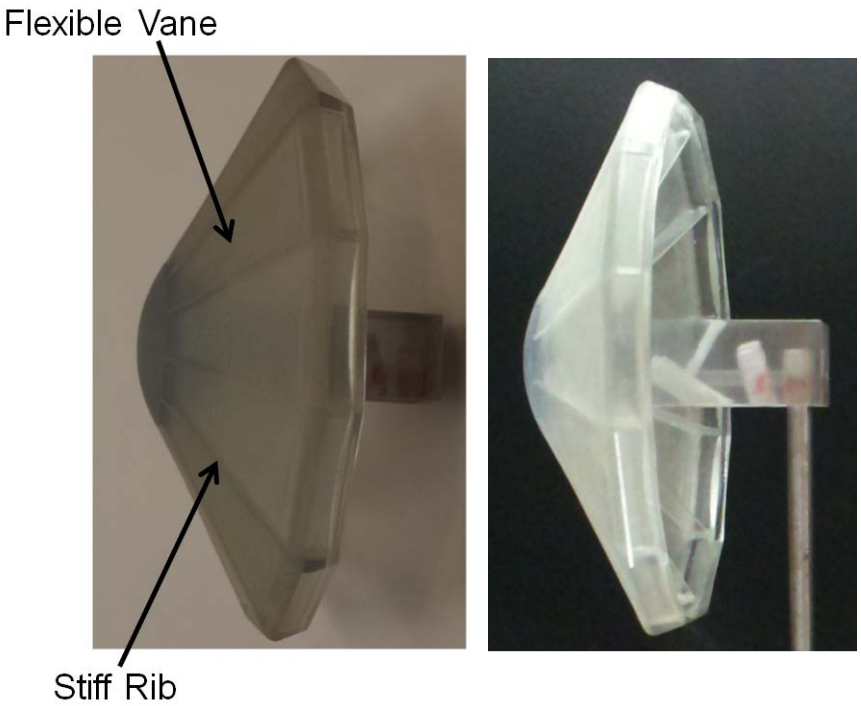

Figure 3-2: Decelerator model.

3.1.2 Materials

The Objet Connex 500 printer uses PolyJet™ technology to manufacture a single model out of both hard and flexible materials. The model supporting structure is printed out of a stiff, ABS-like material designated by Stratasys as “VeroClear”, while the vane, which represents the flexible carbon fabric, is printed out of a flexible rubber-like material named “TangoPlus”. The material properties of VeroClear and TangoPlus from the manufacturer are shown in Table 3-1 and Table 3-2.

Property	ASTM	Units	Metric	Units	Imperial
Tensile Strength	D-638-03	MPa	50-65	psi	7,250-9,450
Elongation at Break	D-638-05	%	10-25	%	10-25
Modulus of Blasticity	D-638-04	MPa	2,000-3,000	psi	290,000-435,000
Flexural Strength	D-790-03	MPa	75-110	psi	11,000-16,000
Flexural Modulus	D-790-04	MPa	2,200-3,200	psi	320,000-465,000
HDT, °C @ 0.45MPa	D-648-06	°C	45-50	°F	113-122
HDT, °C @ 1.82MPa	D-648-07	°C	45-50	°F	113-122
Izod Notched Impact	D-256-06	J/m	20-30	ft lb/inch	0.375-0.562
Water Absorption	D-570-98 24hr	%	1.1-1.5	%	1.1-1.5
Tg	DMA, E>>	°C	52-54	°F	126-129
Shore Hardness (D)	Scale D	Scale D	83-86	Scale D	83-86
Rockwell Hardness	Scale M	Scale M	73-76	Scale M	73-76
Polymerized Density	ASTM D792	g/cm3	1.18-1.19		
Ash Content	USP281	%	0.02-0.06	%	0.02-0.06

Table 3-1: VeroClear material properties [45].

Property	ASTM	Units	Metric	Units	Imperial
Tensile Strength	D-412	MPa	0.8-1.5	psi	115-220
Elongation at Break	D-412	%	170-220	%	170-220
Compressive Set	D-395	%	4-5	%	4-5
Shore Hardness (A)	D-2240	Scale A	26-28	Scale A	26-28
Tensile Tear Resistance	D-624	Kg/cm	2-4	Lb/in	18-22
Polymerized Density	ASTM D792	g/cm3	1.12-1.13		

Table 3-2: TangoPlus material properties [45].

In comparison, VeroClear has a much higher tensile strength, 50-65 MPa, than TangoPlus, 0.8-1.5 MPa. The elastic modulus of VeroClear is 2,000-3,000 MPa and it is not given for TangoPlus. However, from physical examination, it can be seen that the TangoPlus material is rubber-like and much softer than VeroClear.

Tensile tests of dog bone samples made out of both materials were performed on an Instron 3366 machine with a 1000 Newton load cell in accordance with the ASTM D-638 standard for specimen type V. A photo of the Instron machine that the test was performed on as well as close up of the grippers loaded with samples can be seen in Figure 3-3. The samples were manufactured about 2 hours before the tests.

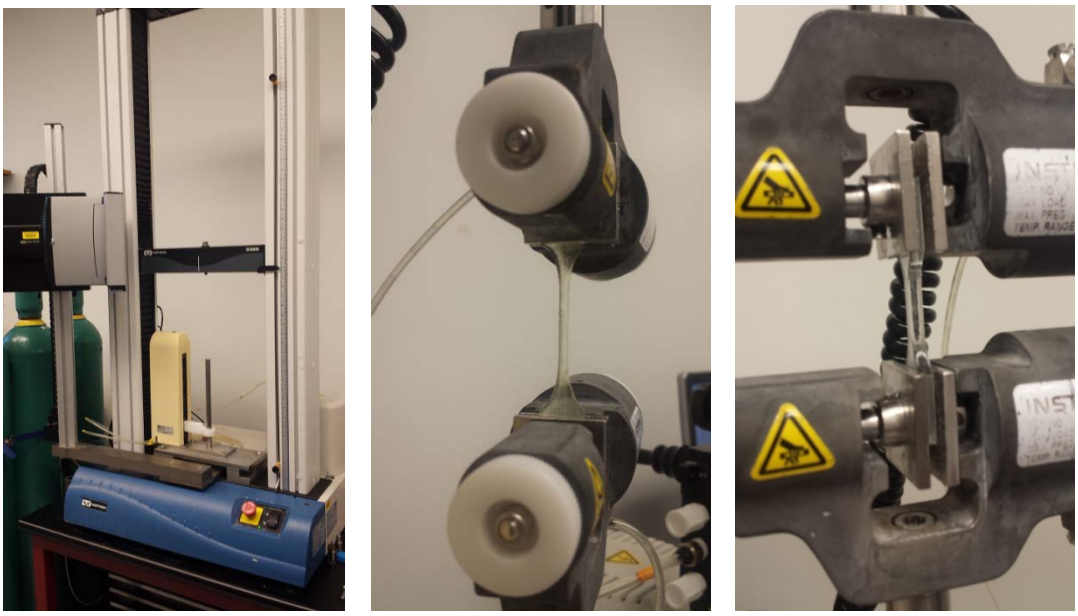

(a) **(b)** **(c)**

Figure 3-3: (a) Instron 3366 machine (b) Instron grippers with TangoPlus sample (c) Instron grippers with VeroClear sample

Per recommendations from the standard, the pull rate was 10 mm/min for the TangoPlus, and 1 mm/min for the Veroclear. The overall length and width of the sample was 60.30 mm by 12.70 mm. The cross section of the sample at the narrowest section was square with side length of 3.20 mm. A dimensioned drawing of the sample is displayed in Figure 3-4.

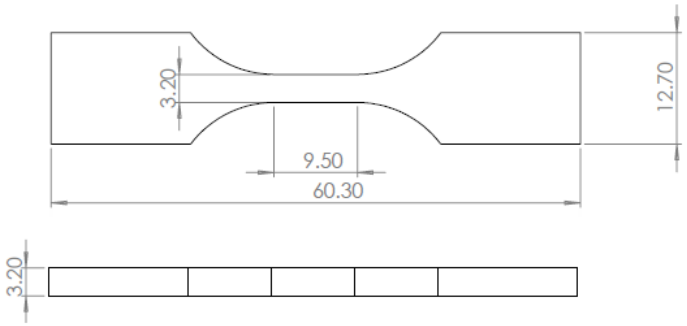

Figure 3-4: ASTM D-638 Type V specimen dimensions [millimeters].

In order to convert force and displacement measurements from the pull test to stress-strain curves, the effective length of the test sample needs to be known. A COMSOL simulation was performed to determine the effective length. The elastic modulus, E, and the Poisson's ratio, ν, of the materials were set to 1 GPa and 0.45 respectively. The "nearly incompressible" setting in COMSOL was turned on because the value of ν was very close to 0.5, resulting in a computation which used a mixed formulation to avoid locking of the elements. The results of the simulation are illustrated in Figure 3-5.

The black rectangles in the figure are used to represent the grips of the Instron machine which define the boundary conditions. The rectangles and thus the grips are 25.4 mm (1 inch) apart. The part of the specimen in the lower rectangle is fixed, while the part in the top rectangle was displaced up by 0.1 mm to stretch the specimen in the vertical direction. The effective length of the sample is determined so that the displacement of the grips divided by the effective length gives the strain in the center of the sample, that is,

$$\varepsilon_y = \frac{\Delta y}{L}$$

So, the effective length was computed from simulation by dividing the end displacement, 0.1 mm, by the strain in the middle of the test section from the results, 0.0047. The effective length, L, is then 21.2 mm.

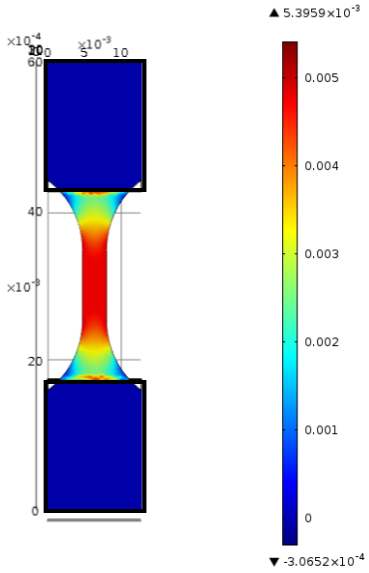

Figure 3-5: Results of COMSOL study.

The measured force is converted into stress by dividing it by the area of the cross section, A = 10.22 mm^2, and the measured displacement, Δy, is converted into strain by dividing it by the effective length, L.

The stress-strain data calculated using this method is illustrated in stress-strain diagrams in Figure 3-6 and Figure 3-7 below.

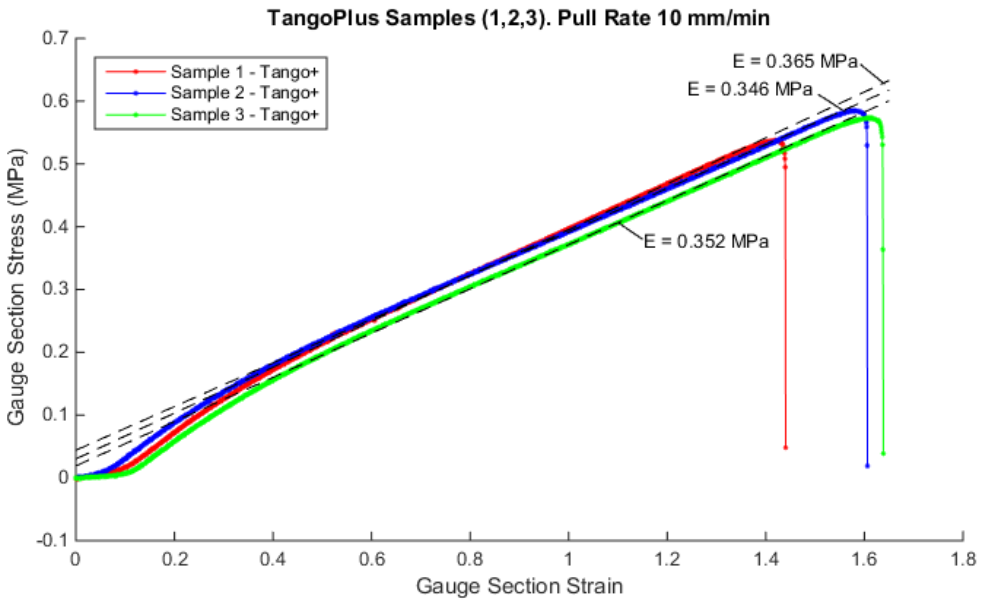

Figure 3-6: TangoPlus stress-strain curves.

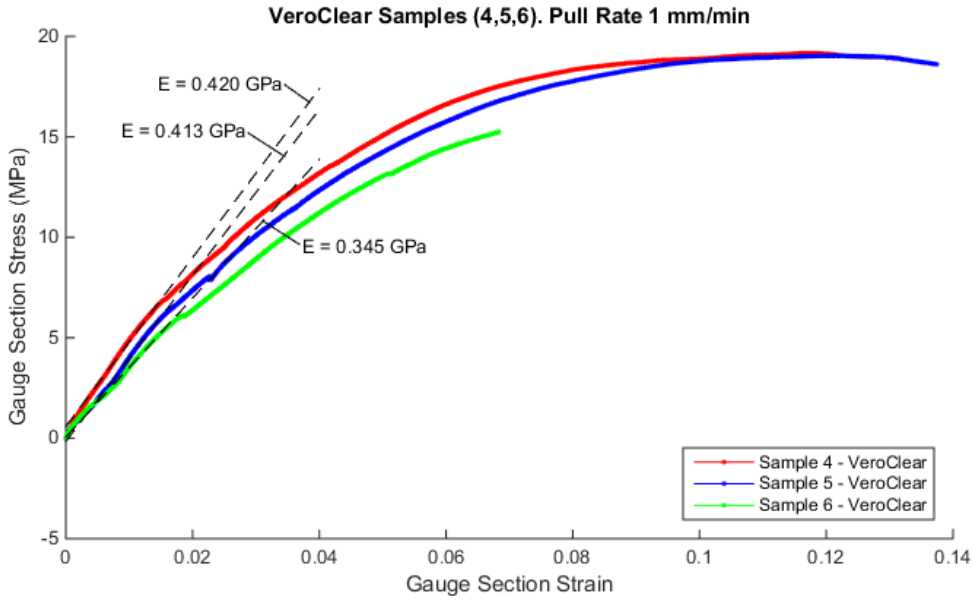

Figure 3-7: VeroClear stress-strain curves.

The plots show good repeatability. A linear regression was performed for the linear sections of the stress-strain curves to find the elastic modulus of the materials. The average modulus of elasticity for the TangoPlus samples from tensile tests is 0.354 MPa while average tensile strength is 0.566 MPa. The modulus elasticity is not given for

TangoPlus by the manufacturer, but the tensile strength is smaller than the one given by the manufacturer, 0.8 – 1.5 MPa. It is possible that this is related to the fact that the conditions that the tests were performed under were different or that the samples were manufactured only 2 hours prior to the test.

The VeroClear samples slipped in the grippers during the tensile tests, which can be seen by the kinks in the stress-strain curves. The linear section before the first slipping event occurred was used to calculate the elastic modulus. The elastic modulus of VeroClear given by the manufacturer (2 GPa) and that of the tensile tests (0.393 GPa) differs by 80%. The tensile strength of VeroClear given by the manufacturer (50 MPa) and that of the tensile tests (19.1 MPa) differs by 62%. However, the slipping of the sample made it impossible to make the samples fail because the stress strain curve flattened out. Had there been enough compression force in the grippers to prevent the slipping, it is possible that a higher stress could be observed before failure.

3.2 Wind-Tunnel Testing

Experimental data was collected in a horizontal wind tunnel at NASA's Ames Research Center. This section describes the experimental setup in the wind tunnel and procedures used to collect the data.

3.2.1 Wind Tunnel Experimental Setup

The flow testing was performed in the NASA Ames horizontal 15" x 15" indraft tunnel illustrated in Figure 3-8. After entering the wind tunnel through the inlet, the air

passes through a series of screens as it flows down the contraction section. It then flows through the test section and exits through the expansion sections and by the blower fan.

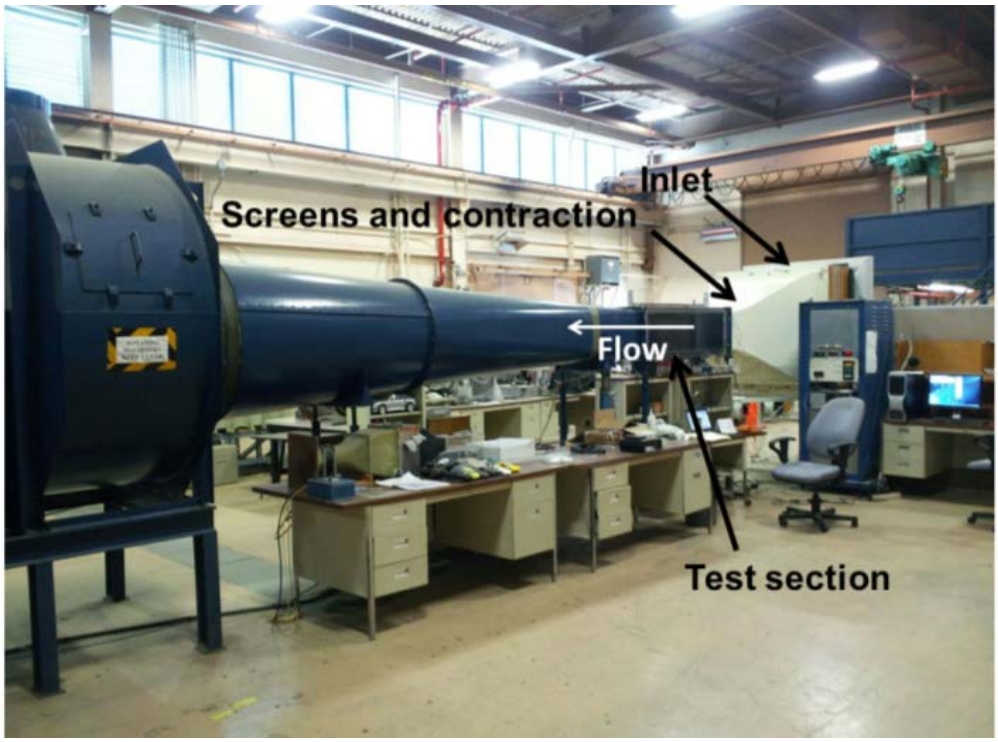

Figure 3-8: NASA Ames 15 inch indraft tunnel.

The wind tunnel test section is shown in Figure 3-9. The decelerator model is mounted horizontally on a 0.25" stainless steel rod which is attached to an Omega TQ201-25 torque transducer (full range 25 in-lbs, accuracy ±0.15% FSO) on the other end which is used to measure the unsteady aero loads on the model under flow. The rod extends through the base plate which is mounted flush with the floor of the test section. A pitot probe at the front of the test section was used to measure dynamic pressure which was used to derive the velocity of the flow. Another pitot probe behind the model was used to record the wake data by measuring the dynamic pressure as a function of distance from the floor. Thermocouples were used to measure flow temperatures as part of the pitot

probes and standard tunnel instrumentation. The standard Basic Data Acquisition Software, BDAS, developed at NASA Ames was used to measure data from the pitot problem and static pressure taps. Discrete measurements were taken at each flow condition and recorded manually. Standard BDAS software was used to control tunnel speed and acquire operational data. Facility instrumentation for the 15” x 15” indraft tunnel was calibrated in-situ.

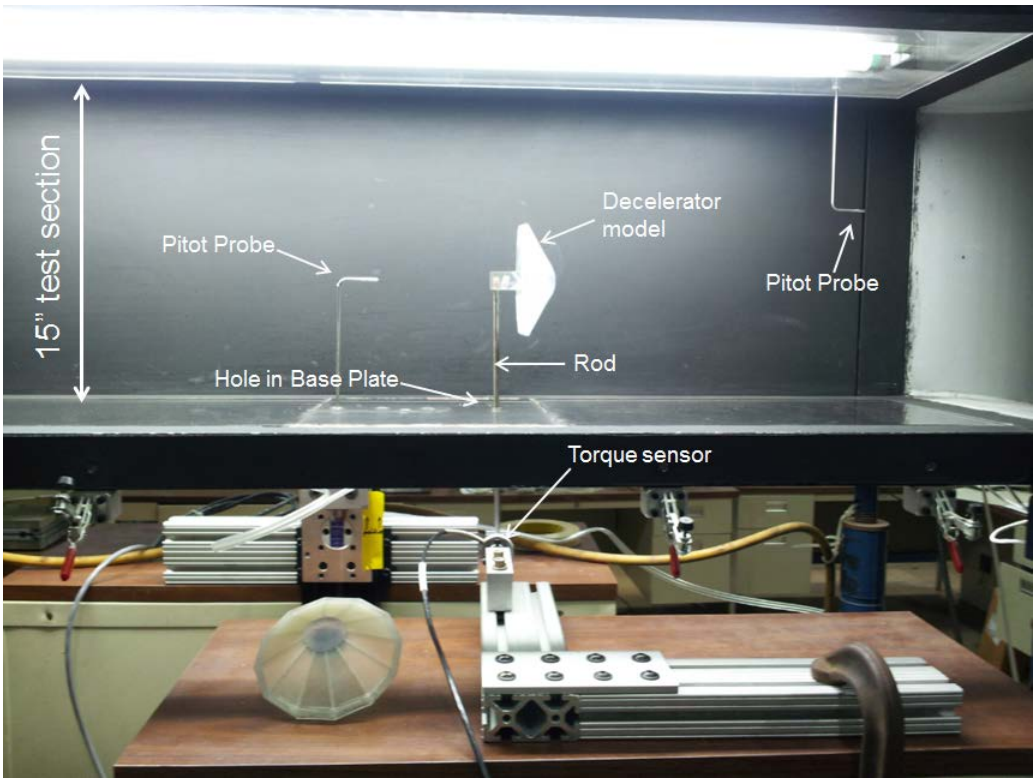

Figure 3-9: Wind tunnel test section set up with decelerator model on a 30.5 inch rod which is attached to a torque transducer.

3.2.2 Test Details

3.2.2.1 Test Configurations

The models were tested on two rods of different lengths: 7.5 inch (19.05 cm) and 12 inch (30.5 cm). Two different wind tunnel speeds were run: 57 feet per second (16.8

m/s, 420 fan rpm, Ma 0.05) and 113 feet per sec (32.6 m/s, 763 fan rpm, Ma 0.1). The model was oriented at 3 angles of attack: 0°, 15°, and 60°. These are fixed angles built into the support structure. The model and rod at different angles of attack is illustrated in a CAD rendering in Figure 3-10.

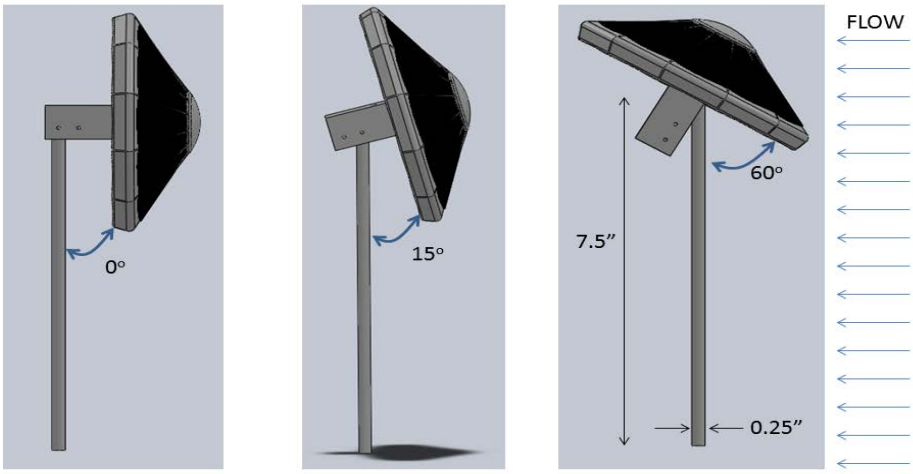

Figure 3-10: Model mounting orientations.

Two models were run: single-material and multi-material. The rod was also tested without a model on it. The test matrix with the rod length, tunnel speed, and angle of attack is shown in Table 3-3.

Rod without model	*Rod Length (cm, in)*	*Tunnel Speed (mps, fps)*	*Angle of Attack (deg)*
1	30.05 (12)	16.8 (57)	-
2	30.05 (12)	32.6 (113)	-
Stiff - Single Material Model			
3	19.05 (7.5)	16.8 (57)	0
4	19.05 (7.5)	16.8 (57)	15
5	19.05 (7.5)	16.8 (57)	60
6	19.05 (7.5)	32.6 (113)	0
7	19.05 (7.5)	32.6 (113)	15
8	19.05 (7.5)	32.6 (113)	60
Soft - Multi Material Model			
9	19.05 (7.5)	16.8 (57)	0
10	19.05 (7.5)	16.8 (57)	15
11	19.05 (7.5)	16.8 (57)	60
12	19.05 (7.5)	32.6 (113)	0
13	19.05 (7.5)	32.6 (113)	15
14	19.05 (7.5)	32.6 (113)	60
Stiff - Single Material Model			
15	30.05 (12)	16.8 (57)	0
16	30.05 (12)	16.8 (57)	15
17	30.05 (12)	16.8 (57)	60
18	30.05 (12)	32.6 (113)	0
19	30.05 (12)	32.6 (113)	15
20	30.05 (12)	32.6 (113)	60
Soft - Multi Material Model			
21	30.05 (12)	16.8 (57)	0
22	30.05 (12)	16.8 (57)	15
23	30.05 (12)	16.8 (57)	60
24	30.05 (12)	32.6 (113)	0
25	30.05 (12)	32.6 (113)	15
26	30.05 (12)	32.6 (113)	60

Table 3-3: Test Matrix

In addition to the runs in flow, resonance tests were performed for each model, rod length, and angle of attack combination.

3.2.2.2 Test Procedures

The floor plate and associated instrumentation were mounted once at the beginning of testing. The tunnel door was closed. The fan rpm control panel was operated to bring the flow up to the desired speed. A BDAS point was acquired, recording tunnel conditions. A time series of torque measurements were acquired from the Omega TQ201-25 using a laptop and National

Instruments data acquisition system. Wake measurements were also taken while traversing the pitot tube behind the model up from the tunnel floor to the center of the tunnel. The flow velocity was brought back down to zero and the next configuration was set up and measured.

4 Results

In the following sections, the data collected for the different cases is analyzed and presented. MATLAB was used for analyzing all of the data and plotting the results.

4.1 Rod without Model in Flow

The first set of measurements was taken for the rod without a mounted model in order to compare the aerodynamic coefficients to theoretical values for a cylinder in cross-flow. The raw data collected were measurements of the torque taken using the torque transducer. The setup of the rod without model is shown in photo in Figure 4-1 and diagram in Figure 4-2.

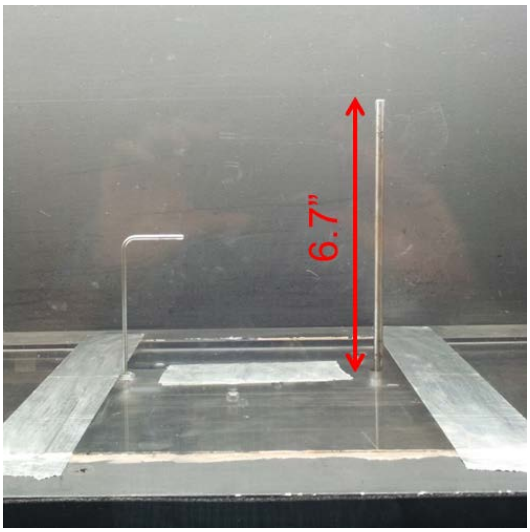

Figure 4-1. Photo showing a 30.5 cm (12 in) rod without mounted model in the wind tunnel test section.

17.0 cm (6.7 inches) of the rod extends through a hole in the base plate into the test section. The air flows right to left and the pitot tube behind the rod measures the dynamic pressure of the wake.

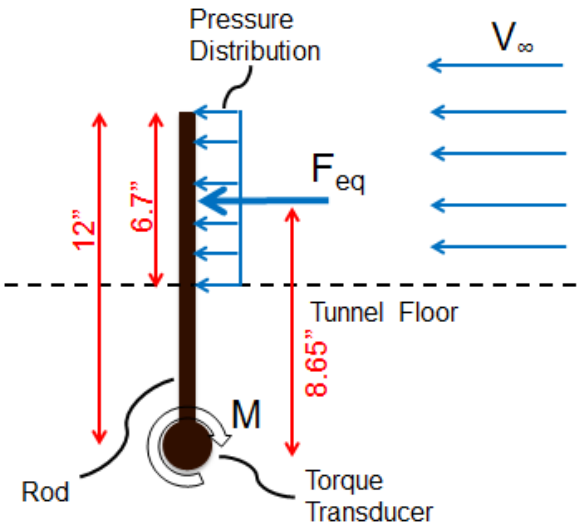

Figure 4-2: Diagram of the 30.5 cm rod in cross-flow.

The rod is attached to a torque transducer at the bottom end. There is a pressure distribution on the exposed section of the rod that extends through the tunnel floor. Assuming that the pressure distribution along the exposed section is constant, an equivalent force acting in the middle of the exposed section or 22.0 cm (8.65 in) away from the torque transducer can be calculated.

Data was collected at two different flow speeds as well as with the wind-tunnel off for control. 16.8 m/s flow had a Reynolds number of 7,400 and 32.6 m/s had a Reynolds number of 14,200 based on the 0.25 inch rod diameter. Raw torque measurements are shown in Figure 4-3. The torque measurements are oscillatory in nature suggesting that there is broadband unsteady forcing of the system.

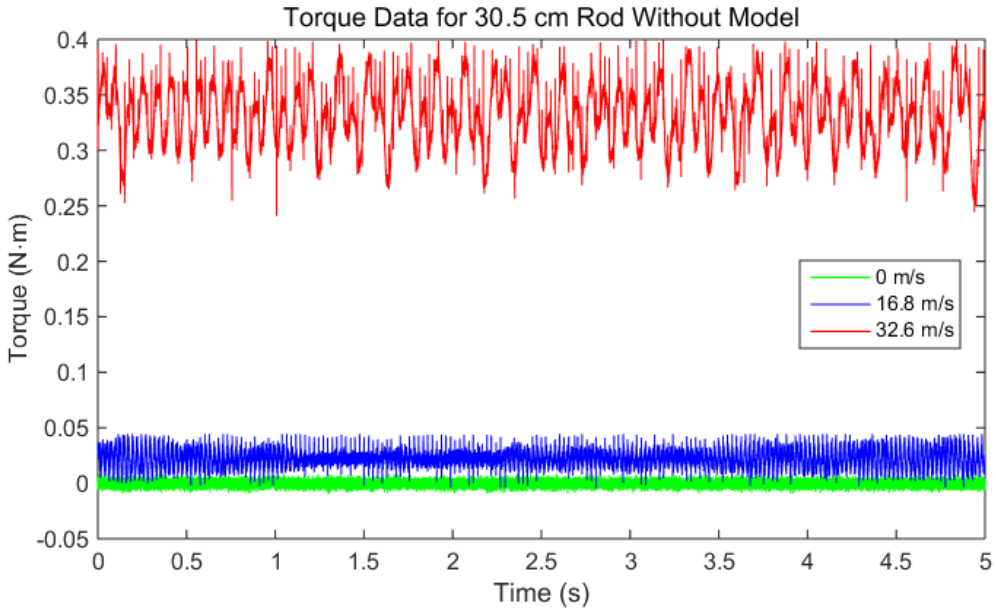

Figure 4-3: Raw torque data for a 30.5 cm rod without a model in 16.8 m/s and 32.6 m/s flow. Also plotted for reference is the torque data taken with wind tunnel off.

The torque was converted into the equivalent force acting on the 12 inch rod by multiplying the torque by a factor of 4.50. The measurements which are converted into equivalent force are shown in Figure 4-4 below.

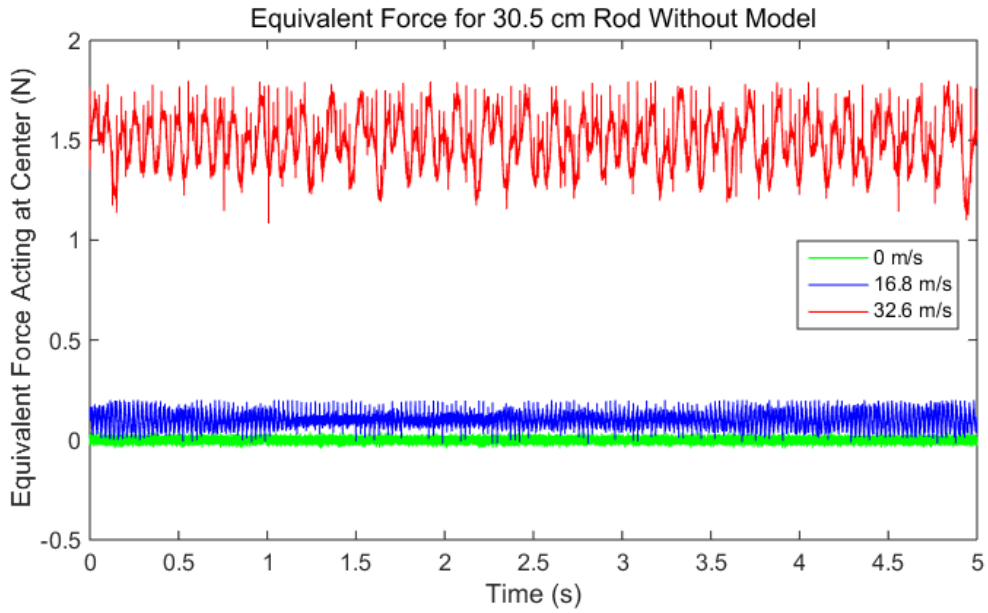

Figure 4-4: Equivalent force acting at center of 30.5 cm rod's region exposed to the flow for rod without a model. Also plotted for reference is the torque data taken with wind tunnel off.

The equivalent force acting on the rod is found by taking the mean of the measured values over the 5 second time period. In 16.8 m/s flow, the mean force is 0.10 N and in 32.6 m/s flow it is 1.49 N. The mean force acting on the rod when the tunnel is off is 0, as expected.

The drag coefficient of the rod can be calculated from the measured drag force using $C_D = \frac{F_D}{0.5A\rho_f V^2}$, where A is the projected frontal area of the exposed portion of the rod, ρ_f is the fluid density. The A of the rod can be calculated by multiplying the diameter of the rod, 0.25 inches, by the length of the rod above the tunnel floor, 6.7 inches. After converting the units to meters, the area is found to be 0.0011 m^2. A table showing the fluid (air) density, ρ_f, at the two different flow velocities measured by BDAS can be found below.

Velocity (m/s)	ρ_f (kg/m^3)
16.8	1.195
32.6	1.186

Table 4-1: Fluid density at the two different flow velocities

The drag force on the rod with 30.5 cm length and 0.25 inch diameter in 16.8 m/s flow is 0.55 and in 32.6 m/s flow it is 2.18. The drag force and drag coefficients on the rod at the two different flow velocities are shown in Table 4-2.

	16.8 m/s Flow (Re 7,400)	32.6 m/s Flow (Re 14,200)
F_D(N)	0.0998	1.4875
C_D	0.5498	2.1824

Table 4-2: Drag force and coefficient on the 30.5 cm length and ¼ inch rod rod

In this experiment, the drag coefficient of the rod at two different flow velocities varies greatly which does not agree with the expected values. According to Figure 4-5 taken

from [46], the drag coefficient for Reynolds numbers 7,400 and 14,200 is about 1.2 and 1.7 respectively. So, the drag coefficient for the 32.6 m/s flow is close to the expected value, while the drag coefficient for the 16.8 m/s does not match. One possible source of error could be a result of the fact that the rod is not a truly infinitely long cylinder, but has a finite length which ends in the middle of the flow which could potentially cause unexpected flow conditions at the free end. This could have caused the deviation of the experimental values from the expected values in Figure 4-5.

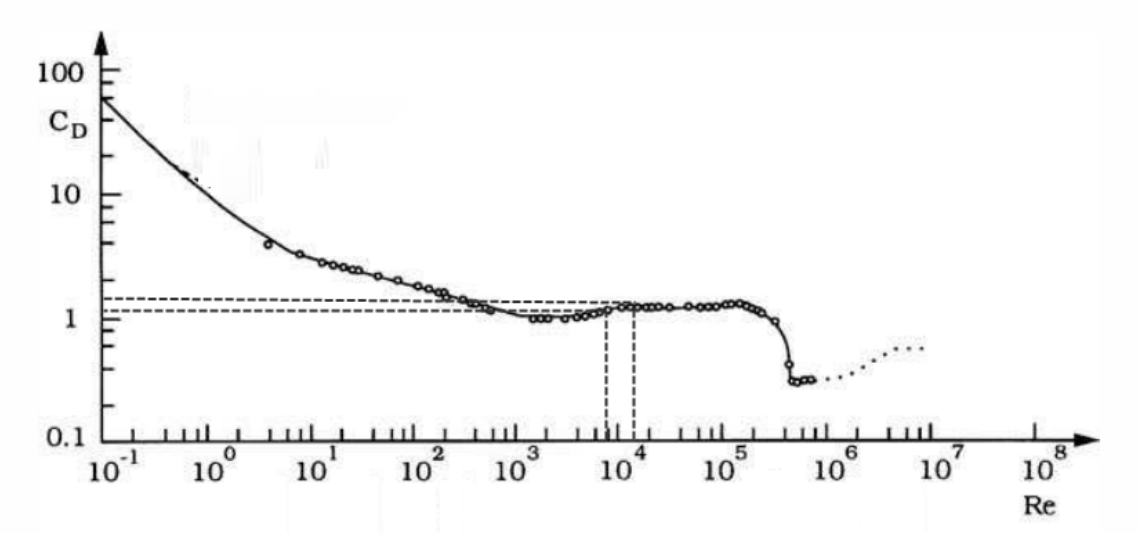

Figure 4-5: Drag coefficient for a smooth circular cylinder as a function of the Reynolds number. Modified from [46] Page 43

Next, the data was zeroed by subtracting the mean force value from the measurements and filtered using a Butterworth filter resulting in Figure 4-6.

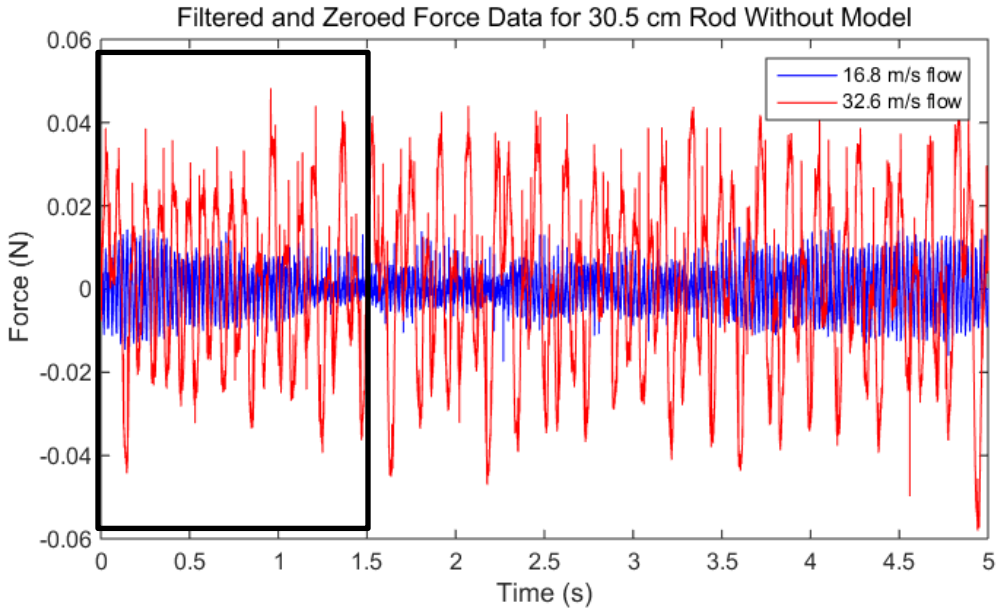

Figure 4-6: Filtered and zeroed equivalent force data for force acting at center of 30.5 cm rod's region exposed to the 16.8 m/s and 32 m/s flow after a Butterworth filter (5th order and break frequency of 300 Hz) is applied.

A detail view of the area in the box in Figure 4-6 from 0 to 1.5 seconds can be seen in Figure 4-7.

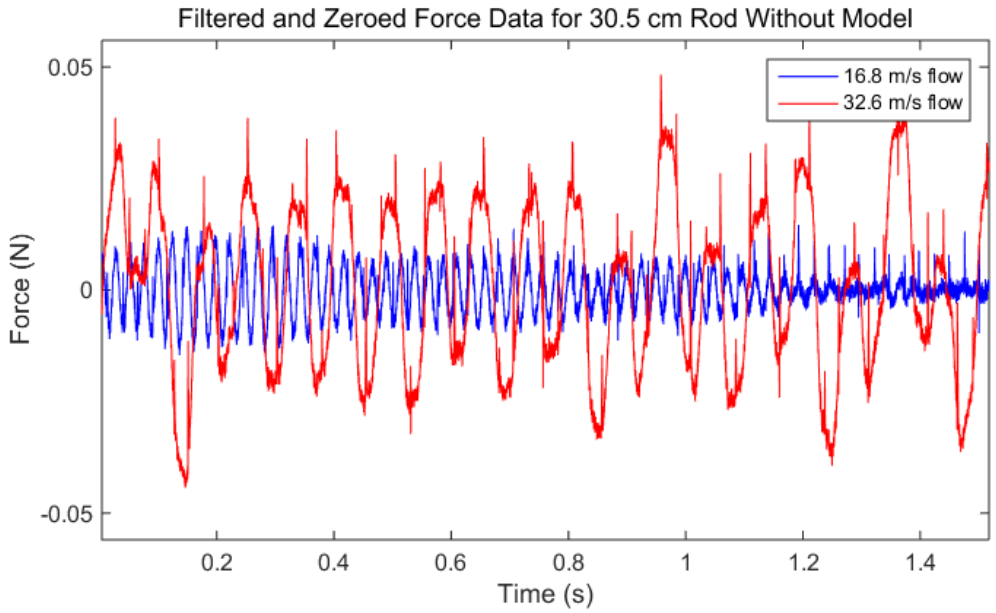

Figure 4-7: Detail view displaying the area shown in Figure 4-6 of filtered and zeroed equivalent force data for force acting at center of 30.5 cm rod's region exposed to the 16.8 m/s and 32 m/s flow after a Butterworth filter (5th order and break frequency of 300 Hz) is applied.

A Fast Fourier Transform (FFT) was used calculate and plot the single-sided amplitude spectrum on a logarithmic scale, shown in Figure 4-8, to find the resonant frequency.

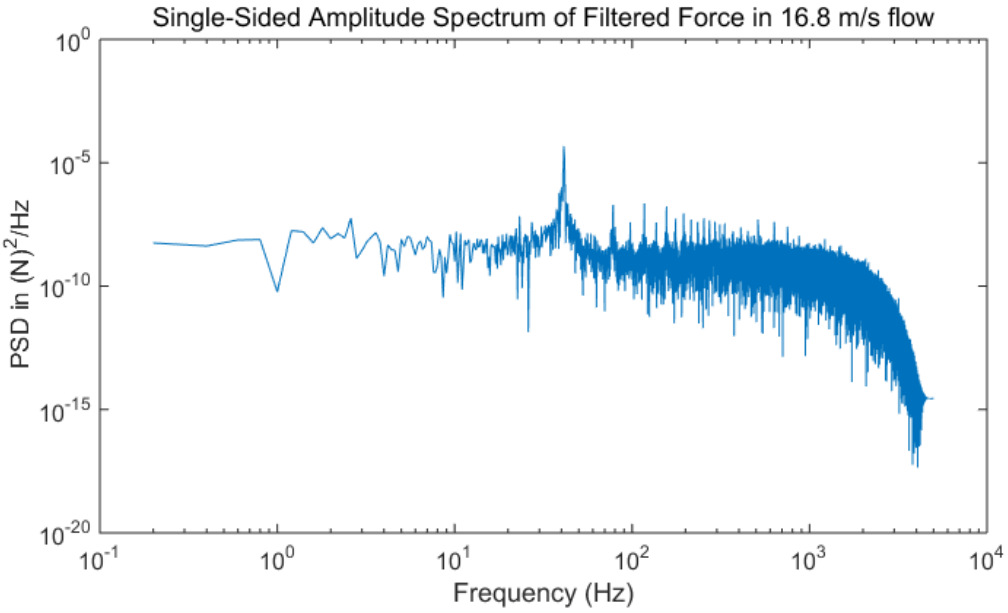

Figure 4-8: Single-sided amplitude spectrum of filtered force for 30.5 cm rod in 16.8 m/s flow.

The resonant frequency of the vibrating rod in the 16.8 m/s flow is at a frequency where there is a distinct peak, 41.2 Hz. The corresponding Strouhal number (St) for this frequency can be found using $St = \frac{\omega l}{V}$, and is 0.0156 for the 0.25 inch rod in 16.8 m/s flow. The frequencies and Strouhal numbers for the two flow velocities are shown in Table 4-3.

	16.8 m/s Flow (Re 7,400)	32.6 m/s Flow (Re 14,200)
ω (Hz)	41.2	38.2
St	0.016	0.007

Table 4-3: Resonant frequency and Strouhal number for the 30.5 cm length and ¼ inch rod at different flow speeds

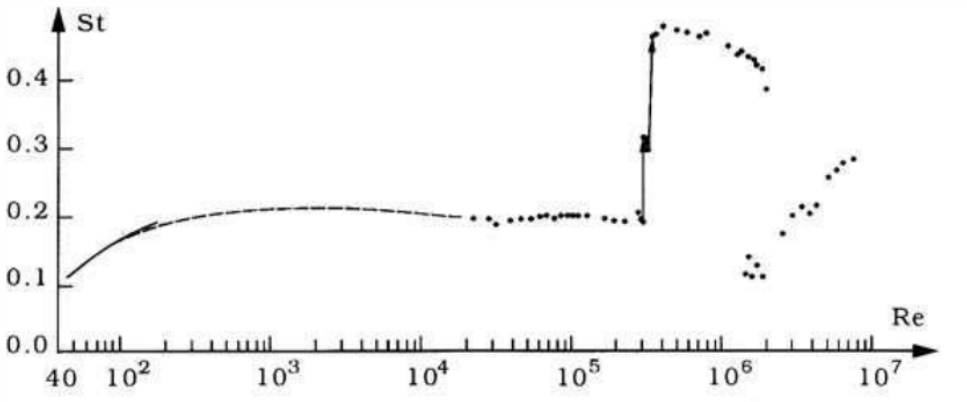

Figure 4-9: Strouhal number for a smooth circular cylinder taken from [46] page 10 and modified. Experimental data from: Solid curve: Williams (1989). Dashed curve: Roshko (1961). Dots: Schewe (1983).

According to Figure 4-9, the Strouhal number for the rod at these Reynolds numbers should be approximately 0.2. The fact that the St for the resonant frequency is much smaller shows that frequency that the rod is vibrating at is not the vortex shedding frequency. It is likely that the resonant frequency of the mechanical system which is excited by the broadband unsteady forcing is dominating any vibration that may be occurring due to the vortex shedding.

The resonant frequency for the 32.6 m/s flow is less obvious from the power spectral density (PDS) as seen in Figure 4-10. The two peaks at 5.4 Hz and 12.8 Hz are likely caused by the rod is coming in contact with the base plate as it is vibrating, causing other modes of vibration.

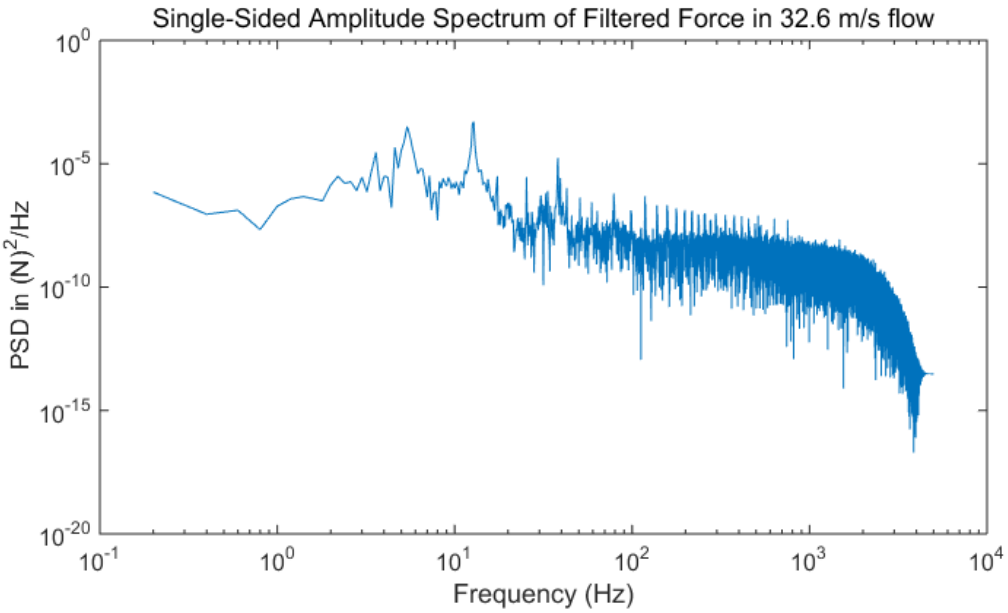

Figure 4-10: Single-sided amplitude spectrum of filtered force for 30.5 cm rod in 32.6 m/s flow.

Just as with the rod in 16.8 m/s flow, the vibration due to vortex shedding is not apparent in the PSD.

4.2 Rod with Decelerator Model in Flow

The next sets of measurements were taken with the stiff and soft decelerator models mounted on two rods of 19.05 cm and 30.5 cm length. The setup of a 19.05 cm rod with a decelerator model is shown in photo in Figure 4-11 and diagram in Figure 4-12.

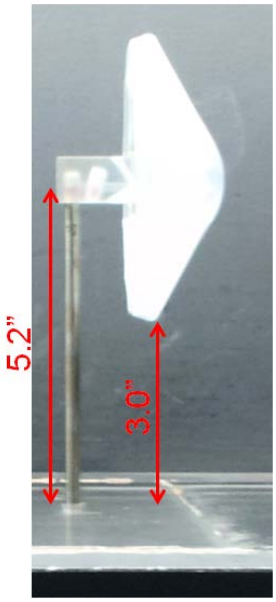

Figure 4-11: Decelerator model on 19.05 cm (7.5 inch) rod in test section.

The rod extends 5.2 inches from the base plate. In the 0° angle of attack setup as shown in the photo, the decelerator model is mounted perpendicular to the rod so that the centerline of the decelerator is parallel to the direction of flow. The decelerator is also mounted with a 15° and 60° angle of attack for another set of measurements.

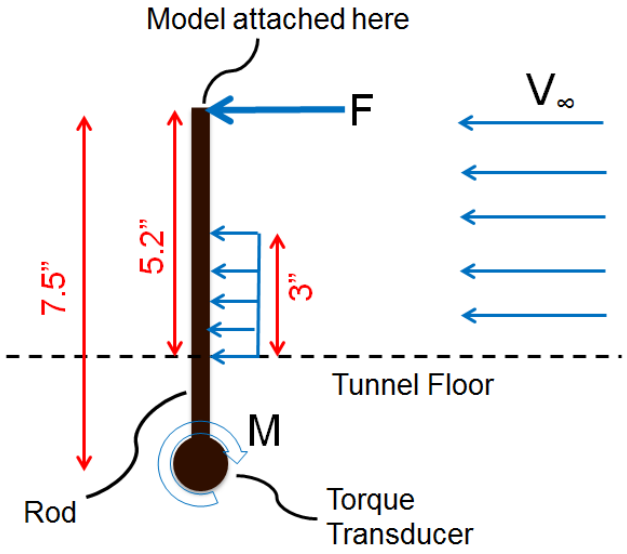

Figure 4-12: Diagram of decelerator on rod in flow.

The rod is attached to a torque transducer at the bottom end. The force on the decelerator acts as a point force on the end of the rod. There is a pressure distribution on the 3 inch exposed section of the rod that extends from the tunnel floor up to the lower edge of the decelerator. When converting torque to force, this force is not taken into account because of its small contribution to the overall force acting on the decelerator.

The torque measurements for the stiff and soft decelerator models mounted on a 19.05 cm rod in 32.6 m/s flow at 0° angle of attack and just the rod are shown in Figure 4-13 below. The torque on both stiff and soft decelerators oscillates from about 1.4 to 1.9 N-m. The force on the rod itself is much lower at about 0.4 N-m.

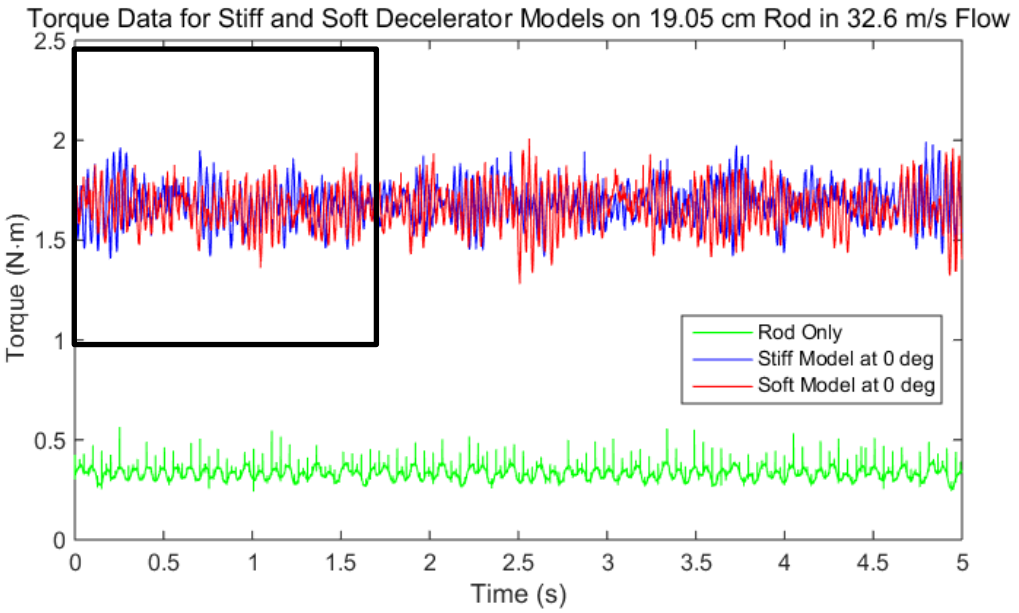

Figure 4-13: Torque vs time for stiff and soft decelerator models mounted on a 19.05 cm rod in 32.6 m/s flow at 0° angle of attack. Also plotted for reference is equivalent force vs time on a 30.5 cm rod without model.

A detail view of the area in the box in Figure 4-13 from 0 to 1.7 seconds can be seen in Figure 4-14.

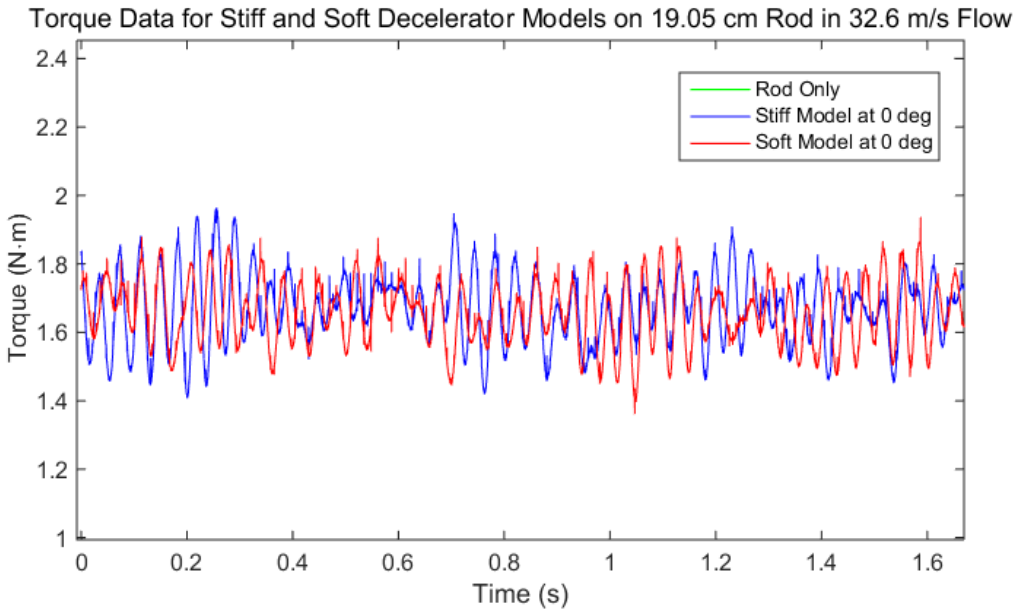

Figure 4-14: Detail view displaying the area shown in Figure 4-13 of torque vs time for soft and stiff decelerator models mounted on a 19.05 cm rod in 32.6 m/s flow at 0° angle of attack.

The torque data can be converted into force data by multiplying the torque by a factor of 5.25. The measurements which are converted into force acting on the decelerator are shown in Figure 4-15 below.

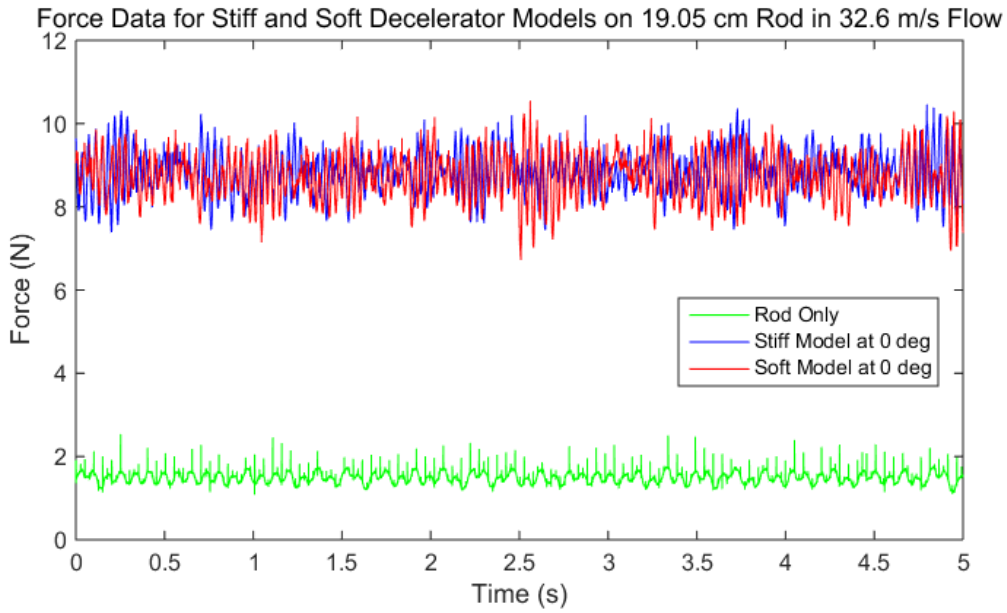

Figure 4-15: Force vs time for stiff and soft decelerator models mounted on a 19.05 cm rod in 32.6 m/s flow at 0° angle of attack. Also plotted for reference is equivalent force on a 30.5 cm rod without model vs time.

The force acting on the decelerator model and rod at 0° angle of attack oscillates between approximately 7.5 N and 10.1 N. The mean drag force is 8.80 N on the stiff decelerator and 8.71 N on the soft decelerator. The drag force on decelerator models in the different test scenarios can be found in Table 4-4 below.

	0 degree angle of attack			
	16.8 m/s Flow		32.6 m/s Flow	
	Stiff Model	Soft Model	Stiff Model	Soft Model
19.05 cm rod	2.0918	2.0683	8.8017	8.7113
30.50 cm rod	2.1687	2.1865	9.0792	8.9518
	15 degree angle of attack			
	16.8 m/s Flow		32.6 m/s Flow	
	Stiff Model	Soft Model	Stiff Model	Soft Model
19.05 cm rod	1.8768	1.8865	7.7884	7.922
30.50 cm rod	2.0123	2.083	8.2417	8.3504
	60 degree angle of attack			
	16.8 m/s Flow		32.6 m/s Flow	
	Stiff Model	Soft Model	Stiff Model	Soft Model
19.05 cm rod	0.5794	0.4898	2.388	2.8438
30.50 cm rod	0.6779	0.5949	2.7401	2.4495

Table 4-4: Drag force in Newtons on stiff and soft decelerator models in different test scenarios: on 19.05 cm and 30.50 cm rods, in 16.8 m/s and 32.6 m/s flow, and 0°, 15°, and 60° angle of attack.

The drag coefficient of the decelerator models can be calculated from the measured drag force using $C_D = \frac{F_D}{0.5 A \rho_f V^2}$, where A is the projected frontal area of the decelerator models.

A list of the projected frontal areas, *A*, of the model can be found below in Table 4-5. The areas are found by projecting the outline of the decelerator CAD model at each angle of attack onto a plane in SOLIDWORKS.

Angle of Attack	A (m^2)
0°	0.012139
15°	0.011747
60°	0.006797

Table 4-5: Projected frontal areas of the decelerator model

The drag coefficient of the stiff and soft decelerator models on 19.05 cm rod, in 32.6 m/s flow, and at a 0° angle of attack is 1.15 and 1.14 respectively. The drag coefficient on decelerator models in the different test scenarios can be found in Table 4-6 below.

	0 degree angle of attack			
	16.8 m/s Flow		32.6 m/s Flow	
	Stiff Model	Soft Model	Stiff Model	Soft Model
19.05 cm rod	1.0266	1.015	1.1496	1.1378
30.5 cm rod	1.064	1.0727	1.1858	1.1692
	15 degree angle of attack			
	16.8 m/s Flow		32.6 m/s Flow	
	Stiff Model	Soft Model	Stiff Model	Soft Model
19.05 cm rod	0.9518	0.9567	1.0512	1.0692
30.5 cm rod	1.0201	1.056	1.1123	1.127
	60 degree angle of attack			
	16.8 m/s Flow		32.6 m/s Flow	
	Stiff Model	Soft Model	Stiff Model	Soft Model
19.05 cm rod	0.5078	0.4293	0.557	0.6633
30.5 cm rod	0.5949	0.5212	0.6392	0.5713

Table 4-6: Drag coefficient on stiff and soft decelerator models in different test scenarios: on 19.05 cm and 30.50 cm rods, in 16.8 m/s and 32.6 m/s flow, and 0°, 15°, and 60° angle of attack.

The drag coefficient is near 1 for the model at 0° and 15° angle of attack which is close to the expected values taken from the Viking lander data in section 2.4 which was also near 1 at Mach 0.4. The drag coefficient is much lower and is close to 0.5 for the model at 60° angle of attack. It is possible that this is due to the smaller projected frontal area. Unfortunately, we don't have any data to compare it to because the axial force coefficient in Figure 2-18(a) is not recorded for angle of attack lower than -25°, but does begin to decrease as the angle of attack gets below -15°.

There is no statistically significant difference between the measured drag coefficient of the soft and stiff models. This was determined by taking the ratio of the drag coefficient for stiff and soft models and subtracting 1. The average of the ratios for the different scenarios is approximately 2% and the standard deviation is approximately 9%.

Next, the data was zeroed by subtracting the mean force value from the measurements and filtered using a Butterworth filter resulting in Figure 4-16.

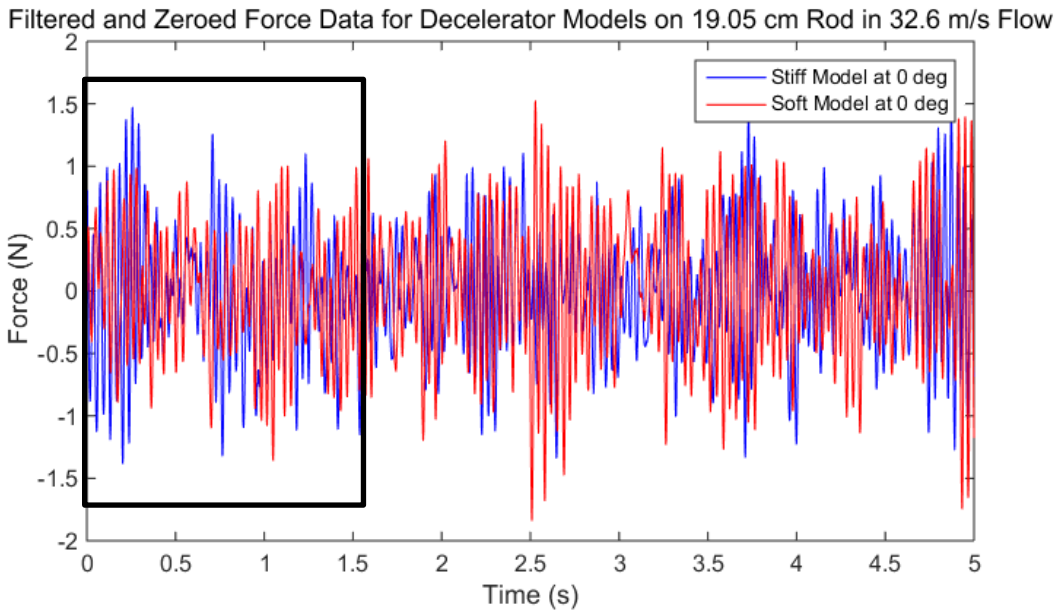

Figure 4-16: Filtered and zeroed force vs time for stiff and soft decelerator models mounted on a 19.05 cm rod in 32.6 m/s flow at 0° angle of attack after a Butterworth filter (5th order and break frequency of 300 Hz) is applied.

A detail view of the area in the box in Figure 4-16 from 0 to 1.5 seconds can be seen in Figure 4-17.

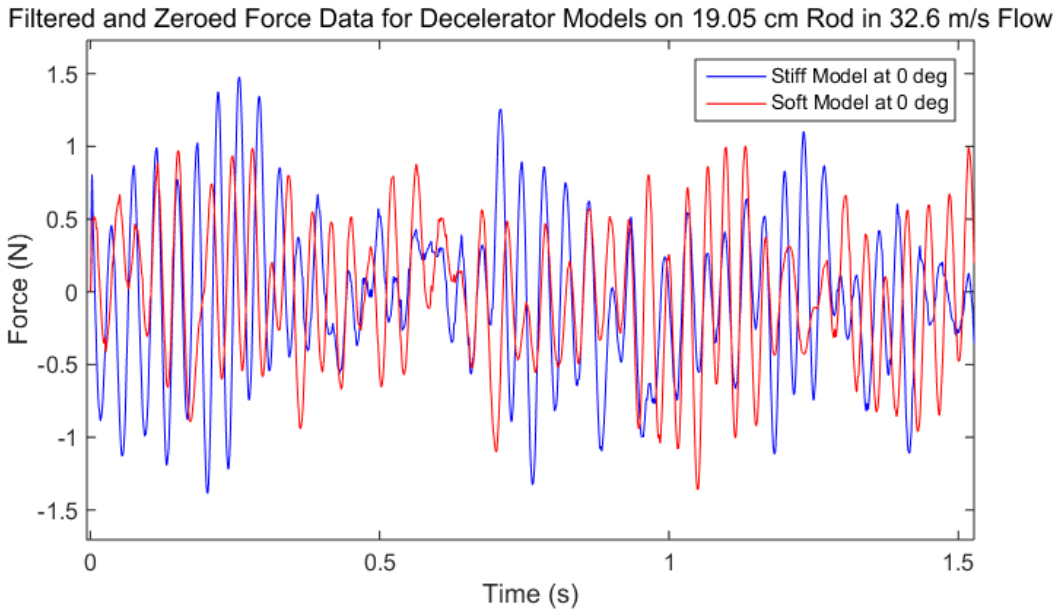

Figure 4-17: Detail view displaying the area shown in Figure 4-16 of filtered force vs time for stiff and soft decelerator models mounted on a 19.05 cm rod in 32.6 m/s flow at 0° angle of attack after a Butterworth filter (5th order and break frequency of 300 Hz) is applied.

An FFT was used to calculate and plot the single-sided amplitude spectrum on a logarithmic scale as shown in Figure 4-18 for the stiff decelerator and Figure 4-19 for the soft decelerator.

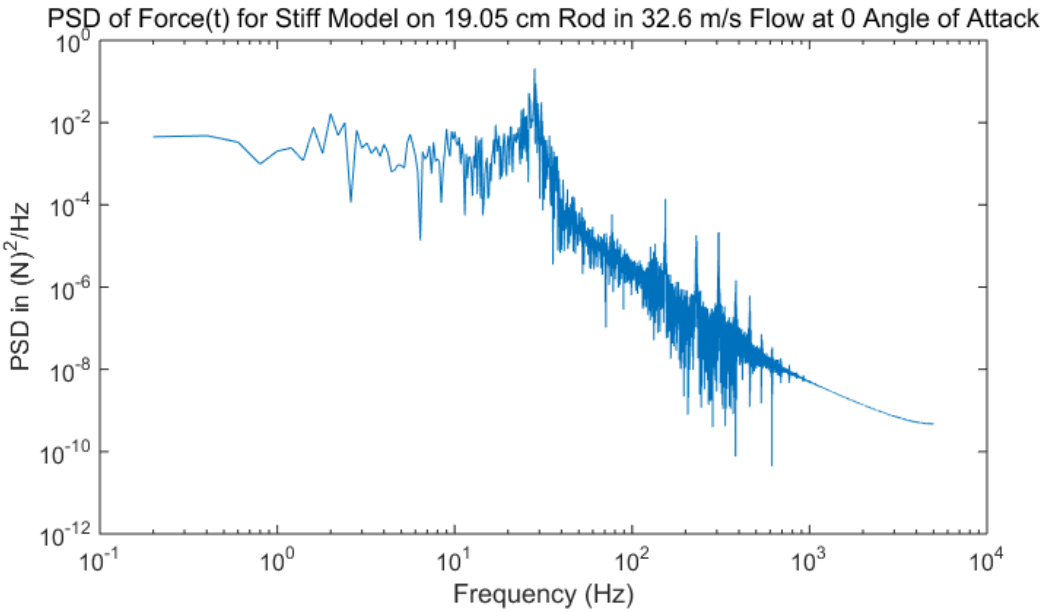

Figure 4-18: Power spectral density of force vs time for stiff decelerator model mounted on a 19.05 cm rod in 32.6 m/s flow at 0° angle of attack.

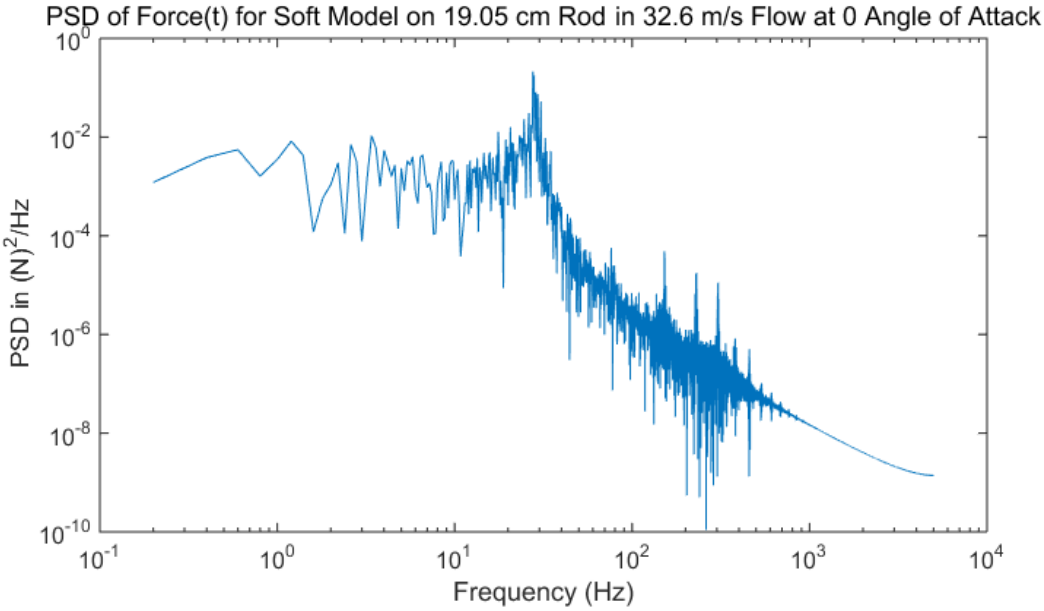

Figure 4-19: Power spectral density of force vs time for soft decelerator model mounted on a 19.05 cm rod in 32.6 m/s flow at 0° angle of attack.

The resonant frequency of the stiff and soft decelerator models in the 32.6 m/s flow is 28.2 Hz and 27.6 Hz respectively. The resonant frequency of decelerator models in the different test scenarios can be found in Table 4-7 below.

	0 degree angle of attack			
	16.8 m/s Flow		32.6 m/s Flow	
	Stiff Model	Soft Model	Stiff Model	Soft Model
19.05 cm rod	28.4	28.4	28.2	27.6
30.5 cm rod	16.4	16.4	16	16.2
	15 degree angle of attack			
	16.8 m/s Flow		32.6 m/s Flow	
	Stiff Model	Soft Model	Stiff Model	Soft Model
19.05 cm rod	27.6	28.6	27.2	27.6
30.5 cm rod	15.8	15.8	16.2	16.2
	60 degree angle of attack			
	16.8 m/s Flow		32.6 m/s Flow	
	Stiff Model	Soft Model	Stiff Model	Soft Model
19.05 cm rod	28.2	28.8	31	36
30.5 cm rod	16.2	16.6	16.2	16.4

Table 4-7: Resonant frequency of stiff and soft decelerator models in different test scenarios: on 19.05 cm and 30.50 cm rods, in 16.8 m/s and 32.6 m/s flow, and 0°, 15°, and 60° angle of attack.

Both the stiff and soft models on the 19.05 cm rod have a resonant frequency of about 28 Hz which is not dependent on the flow speed and angle of attack and both the stiff and soft models on the 30.5 cm rod have a resonant frequency of about 16 Hz which is also independent of the flow speed and angle of attack.

The PSD for all scenarios with the exception of the ones in red text have a single, defined, peak. The stiff and soft models on a 19.05 cm rod at 60° angle of attack in 32.6 m/s flow have multiple peaks. Example of the plot for the soft model is shown in Figure 4-20. There are three distinct peaks at 5.2 Hz, 12.8 Hz, and 36 Hz. The additional modes of vibration could have been caused by the rod coming in contact with the base plate during the test.

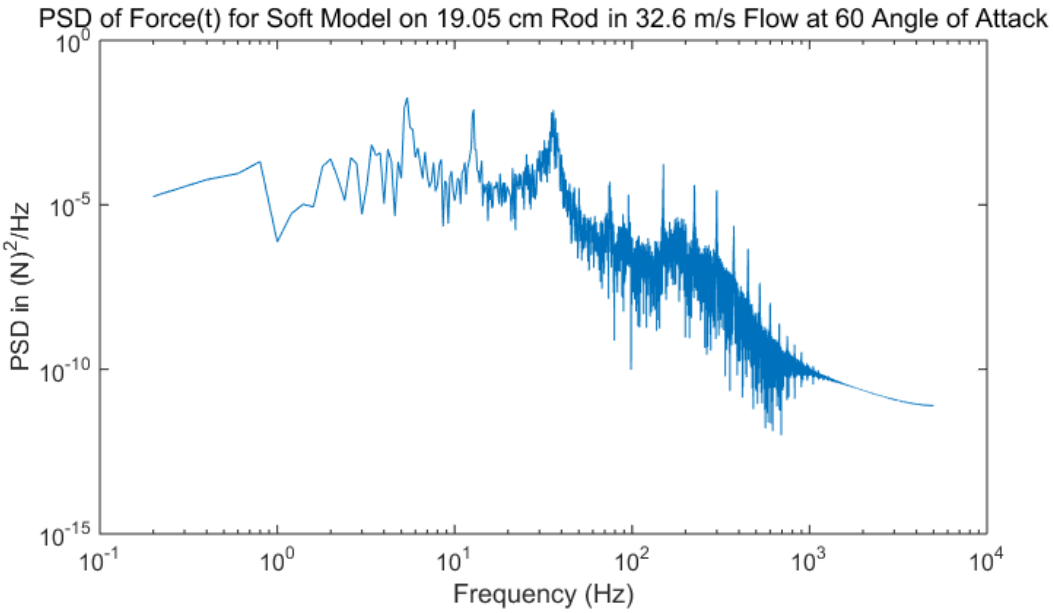

Figure 4-20: Power spectral density of force vs time for soft decelerator model mounted on a 19.05 cm rod in 32.6 m/s flow at 60° angle of attack.

The corresponding Strouhal number for each frequency can be found using $St = \frac{\omega l}{V}$, and is 0.110 for the stiff decelerator model and 0.108 for the soft decelerator model on a 19.05 cm rod and 0° angle of attack in 32.6 m/s flow. The Strouhal Numbers of decelerator models in the different test scenarios can be found in Table 4-8 below.

	0 degree angle of attack			
	16.8 m/s Flow		32.6 m/s Flow	
	Stiff Model	Soft Model	Stiff Model	Soft Model
19.05 cm rod	0.216	0.216	0.110	0.108
30.5 cm rod	0.124	0.124	0.062	0.063
	15 degree angle of attack			
	16.8 m/s Flow		32.6 m/s Flow	
	Stiff Model	Soft Model	Stiff Model	Soft Model
19.05 cm rod	0.209	0.217	0.106	0.108
30.5 cm rod	0.120	0.120	0.063	0.063
	60 degree angle of attack			
	16.8 m/s Flow		32.6 m/s Flow	
	Stiff Model	Soft Model	Stiff Model	Soft Model
19.05 cm rod	0.214	0.219	0.121	0.140
30.5 cm rod	0.123	0.126	0.063	0.064

Table 4-8: Strouhal number of stiff and soft decelerator models in different test scenarios: on 19.05 cm and 30.50 cm rods, in 16.8 m/s and 32.6 m/s flow, and 0°, 15°, and 60° angle of attack.

There is no statistically significant difference between the St of the soft and stiff models. This was determined by taking the absolute value of the ratio of the St for stiff and soft models and subtracting 1. The average of the ratio is approximately 2% and the standard deviation is approximately 1%.

It is also clear that the resonant frequency is dominated by the natural frequency of the mechanical system which is a mass (decelerator) on a spring (rod). The system is excited by the broadband unsteady forcing and is dominating any vibration due to aeroelastic effects. The fact that the St is different for the different rod lengths illustrates that it is dependent on the mass-spring mechanical system. Had there been aeroelastic behavior, it would have resulted in a peak in the PSD corresponding to a single St the soft models on both rod lengths.

4.3 Resonance Tests

The resonance test measurements were taken with the wind tunnel off by flicking the models on the rods to see their response. Figure 4-21 below shows the torque data for stiff and soft decelerator models on 19.05 cm rod at 0° angle of attack. The decelerator model and rod is an underdamped system.

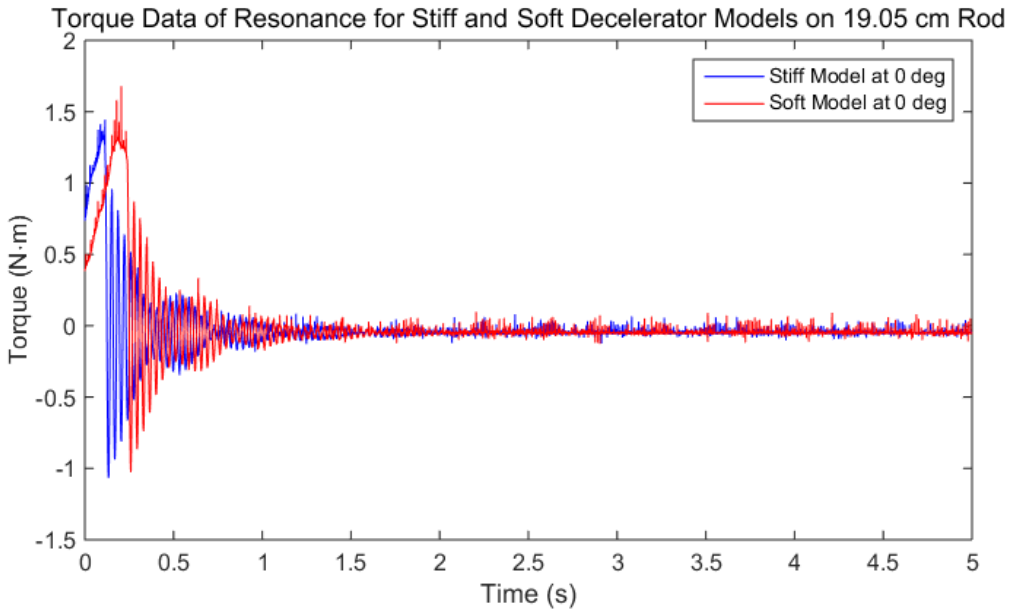

Figure 4-21: Torque vs time measured after a flick during a resonance test for stiff and soft decelerator models mounted on a 19.05 cm rod at 0° angle of attack.

The torque can be converted to force for the 19.05 cm rod by multiplying by a factor of 5.25. The data converted into force and then filtered using a Butterworth filter is shown in Figure 4-22 below.

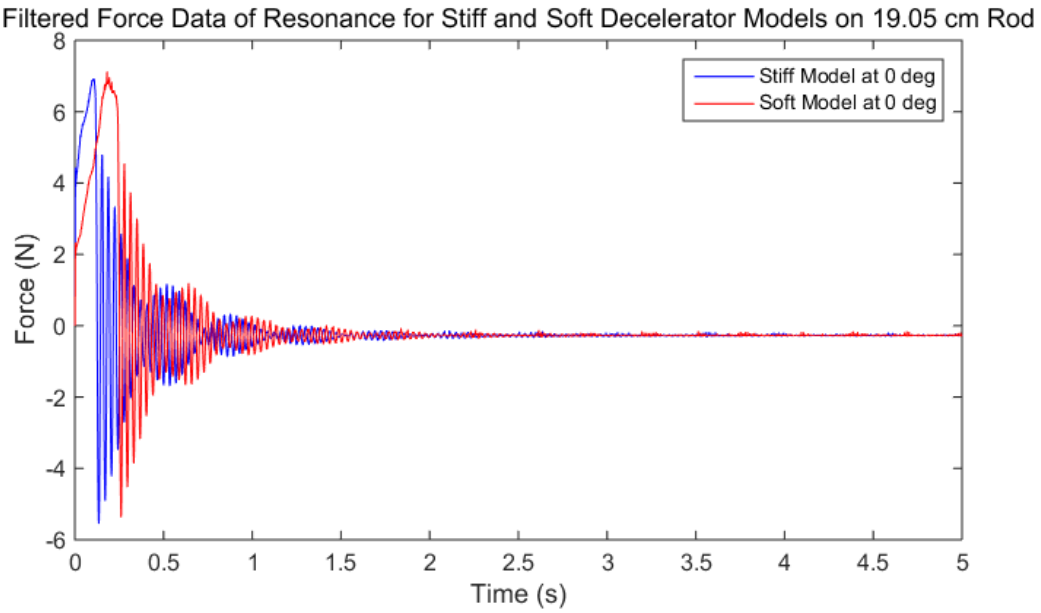

Figure 4-22: Filtered force vs time measured after a tap during a resonance test for stiff and soft decelerator models mounted on a 19.05 cm rod at 0° angle of attack after a Butterworth filter (5th order and break frequency of 300 Hz) is applied.

The power spectral density (PSD) found using an FFT is shown in Figure 4-23 below. The stiff and soft models both vibrate at 27.8 Hz.

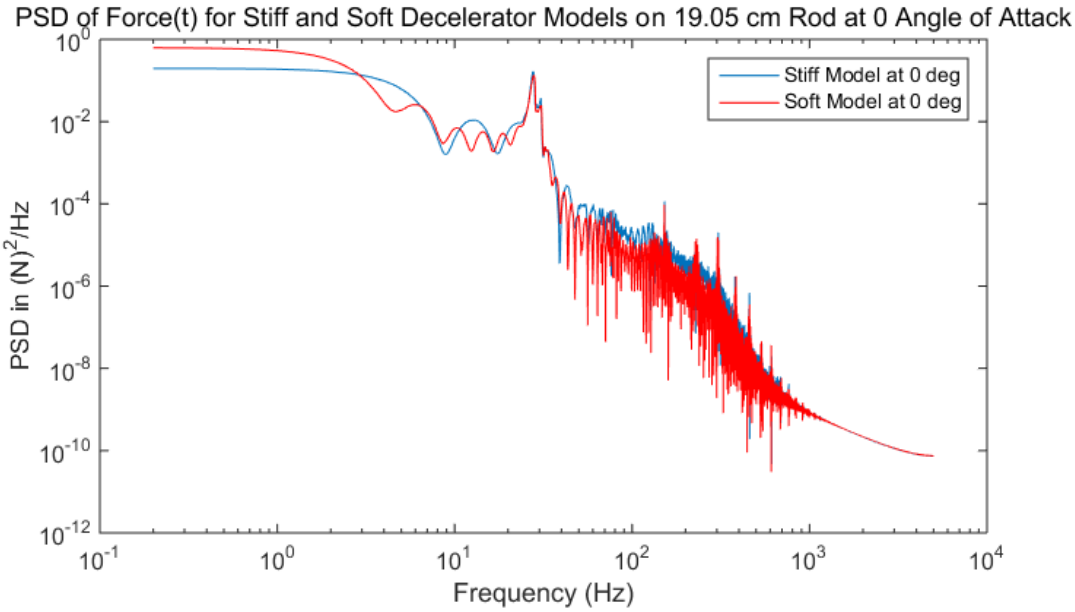

Figure 4-23: Power spectral density of force vs time of a resonance test for stiff and soft decelerator models mounted on a 19.05 cm rod at 0° angle of attack.

The values for the other rod lengths and angle of attack combinations are listed in Table 4-9.

0 degree angle of attack		
	Stiff Model	Soft Model
19.05 cm rod	27.8	27.8
30.5 cm rod	16.4	21.6
15 degree angle of attack		
	Stiff Model	Soft Model
19.05 cm rod	26.8	27.8
30.5 cm rod	16	20.8
60 degree angle of attack		
	Stiff Model	Soft Model
19.05 cm rod	27.2	28.4
30.5 cm rod	20.4	21

Table 4-9: Resonant frequencies of stiff and soft models on 19.05 cm and 30.5 cm rod and 0°, 15°, and 60° angle of attacks.

The numbers in the highlighted red cells are not accurate, so they do not have to be considered because there was a problem with the data which was caused by the rod coming into contact with the wall of the hole in the base plate. It appears to occur for the 30.5 cm rod, but not the 19.05 cm rod; probably because the short rod doesn't have as much travel as the long rod. An example of force data for such a bad case can be seen in Figure 4-24. The oscillation is very far from symmetric, suggesting that the rod was in contact with the base plate.

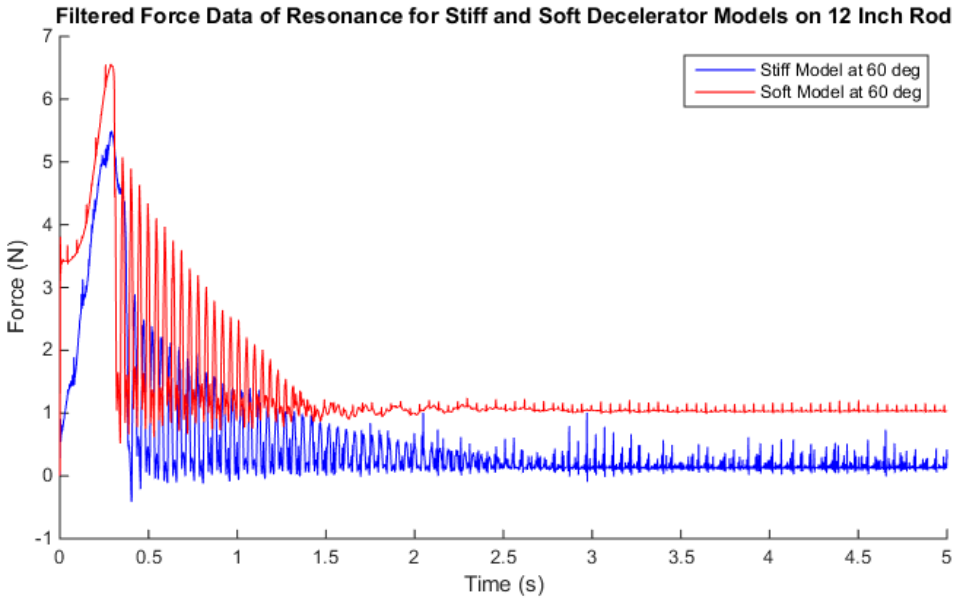

Figure 4-24: Force vs time measured after a tap during a resonance test for stiff and soft decelerator models mounted on a 30.50 cm rod at 60° angle of attack which shows asymmetric likely caused by contact with the base plate.

The PSD for the resonance tests and model in flow can now be compared to see if the frequency of the dominant vibration matches the resonant frequency or if there are other modes of vibration. Figure 4-25 and Figure 4-26 show the superimposed graphs for the stiff and soft models respectively in 32.6 m/s flow, on a 19.05 cm long rod at 0° angle of attack.

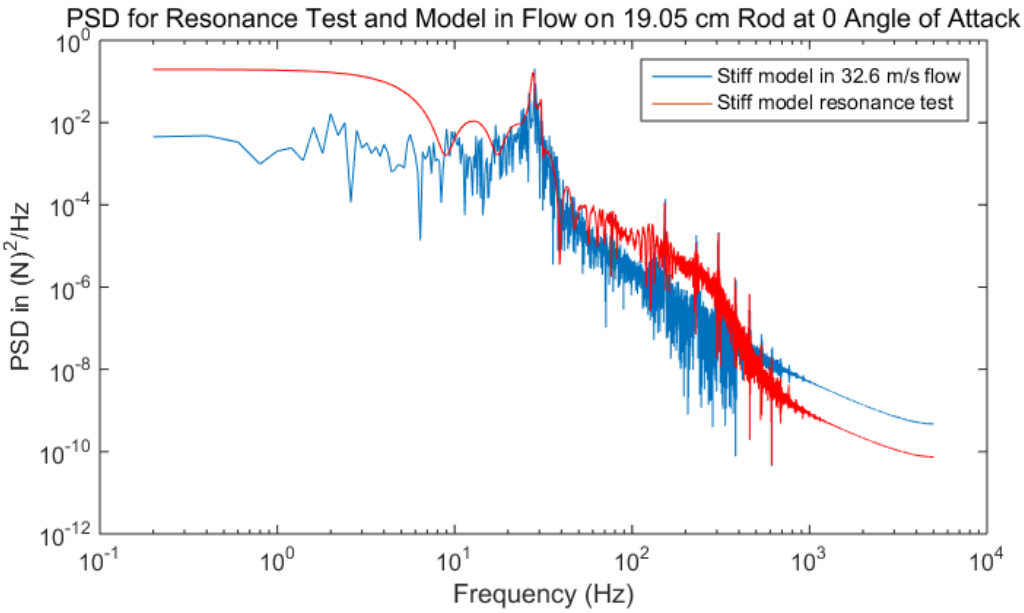

Figure 4-25: Power spectral density of force vs time for a resonance and flow test of a stiff decelerator model mounted on 19.05 cm Rod at 0° angle of attack.

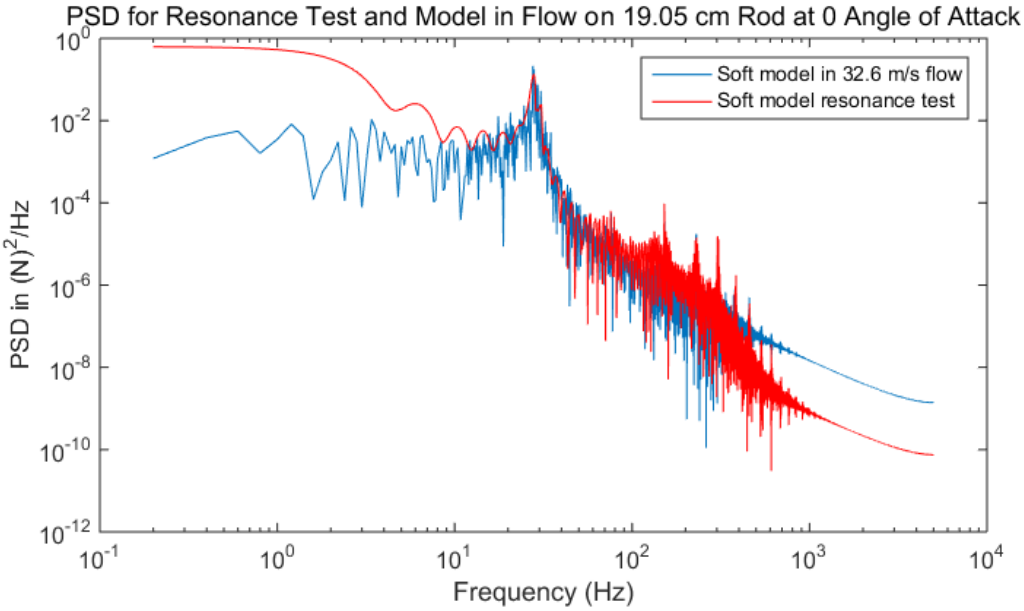

Figure 4-26: Power spectral density of force vs time for a resonance and flow test of a soft decelerator model mounted on 19.05 cm Rod at 0° angle of attack.

The peaks coincide in both figures, showing that the models do vibrate at resonant frequencies in the flow.

4.4 Wake Data

The wake data measurements were taken using the pitot tube behind the model which measured the dynamic pressure data for the different cases. The pitot tube is shown in Figure 4-1.

The pitot tube measures the dynamic pressure for the stiff and soft models, which can be seen in Figure 4-27 for the stiff model and Figure 4-28 for the soft model. In all the figures in this section, a dark, heavy outline cartoon of the decelerator's profile is included to show its vertical location in the tunnel. As the model is rotated to different angles of attack, its centerpoint moves in the tunnel, and also the blocked area of the flow changes.

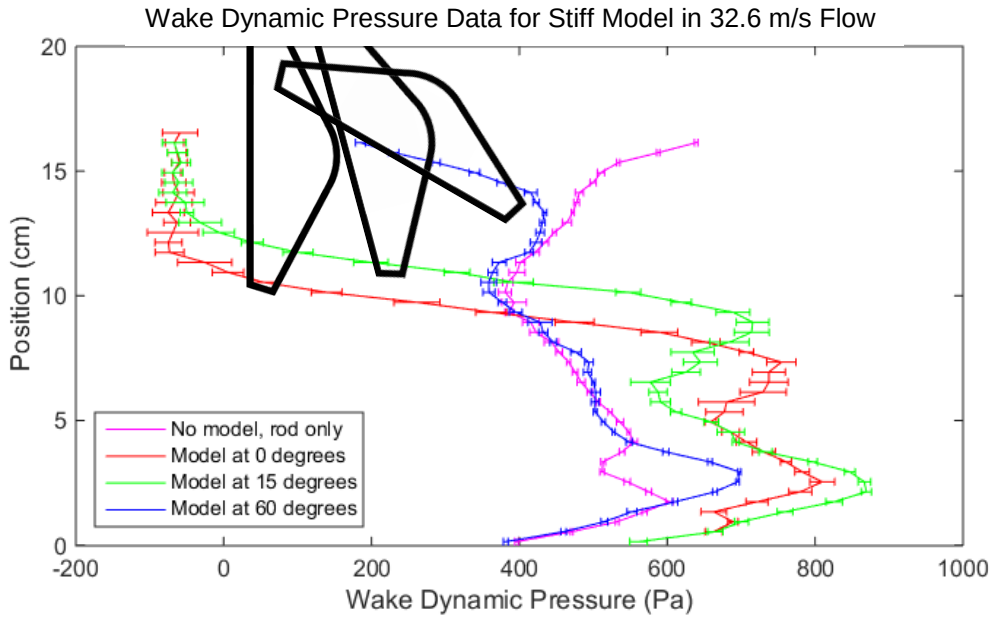

Figure 4-27: Dynamic pressure of wake vs position for stiff model in 32.6 m/s flow with error bars showing the standard deviation for the 10 measurements taken at each position.

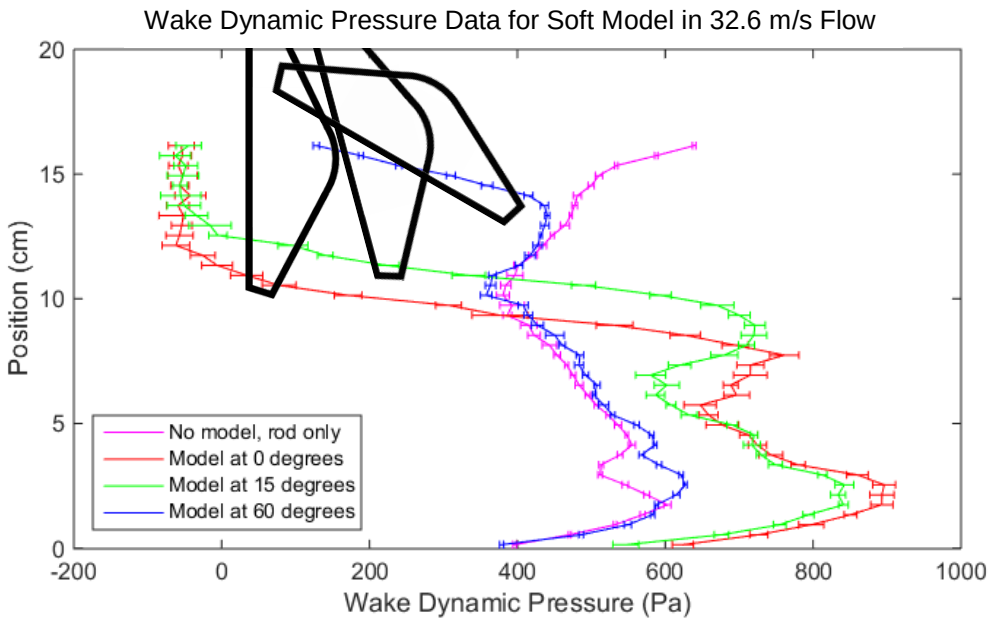

Figure 4-28: Dynamic pressure of wake vs position for soft model in 32.6 m/s flow with error bars showing the standard deviation for the 10 measurements taken at each position.

The dynamic pressure can be converted into velocity using $V = \frac{p}{|p|}\sqrt{|2p/\rho|}$, where v is the velocity, p is the pressure, and ρ is the dynamic pressure. The velocity data can be seen in Figure 4-29 for the stiff model and Figure 4-30 for the soft model. They are very similar and are superimposed in Figure 4-31. The magenta line for the rod without model is shown for reference. The wake velocity directly behind the rod along the length of the rod is around 30 m/s and decreases to 26 m/s when approaching the floor of the wind tunnel due to the boundary layer. The red line represents the wake velocity profile for the model at a 0° angle of attack. It matches expectation because the velocity below the lower edge of the decelerator is greater than the wind tunnel flow speed because the flow speeds up as it is forced around the model. According to Figure 4-11, the lower edge of the decelerator at 0° angle of attack is 3 inches or 7.62 cm above the floor of the tunnel. Above this height, the wake velocity decreases because it is in the shadow of the

decelerator. Then, at about 12 cm above the floor of the tunnel, the vortices appear to create a swirl which reverses the flow, causing a negative velocity which gets to -10 m/s.

As the angle of attack of the decelerator is increased to 15°, the lower edge of the decelerator is higher, so the transition from high to low velocity and then negative velocity happens 2 cm higher than the transition of the decelerator at 0° angle of attack. When the angle of attack is increased to 60°, the lower edge of the decelerator is much higher and the velocity does not get forced around the lower edge of the decelerator because of the orientation of its geometry, thus the wake velocity profile is similar to the rod with no model. They begin to diverge at about 14 cm above the tunnel floor when getting above the lower edge of the decelerator model.

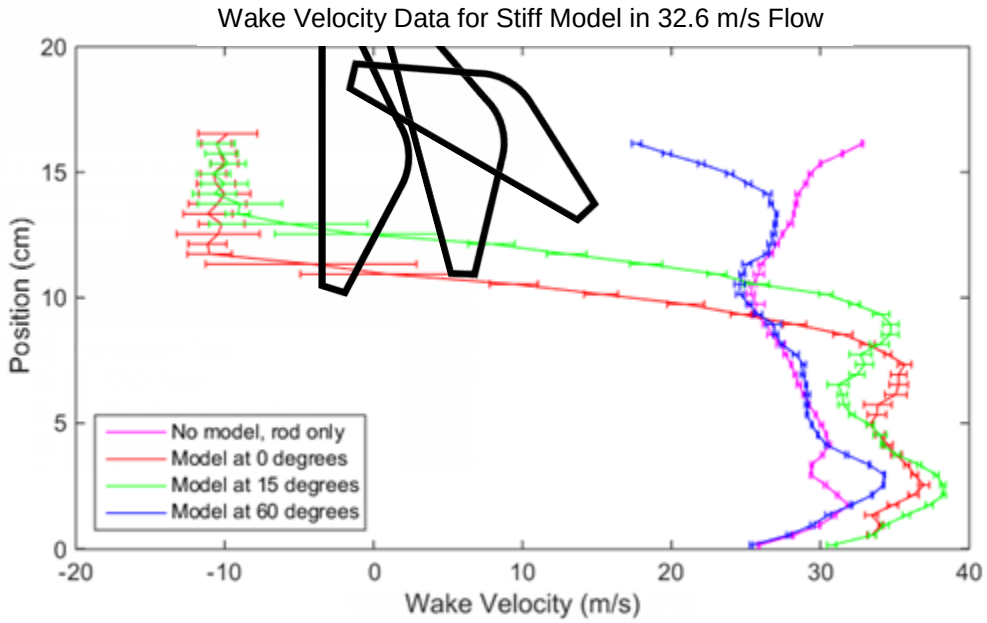

Figure 4-29: Wake velocity vs position for stiff model in 32.6 m/s flow with error bars showing the standard deviation for the 10 measurements taken at each position.

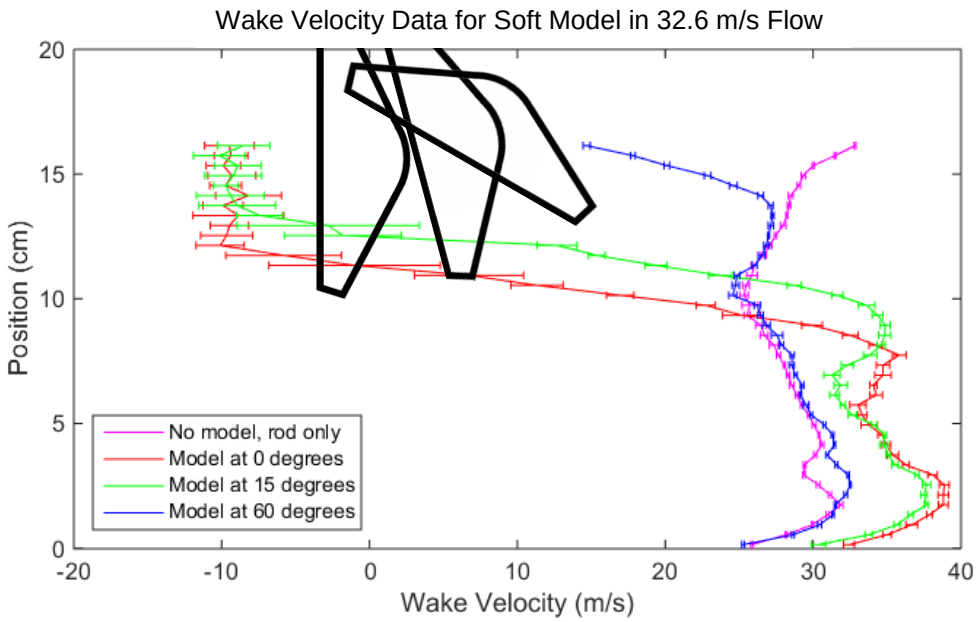

Figure 4-30: Wake velocity vs position for soft model in 32.6 m/s flow with error bars showing the standard deviation for the 10 measurements taken at each position.

The wake velocity data for stiff and soft models in 32.6 m/s flow are superimposed in Figure 4-31 and for stiff and soft models in 16.8 m/s flow in Figure 4-32. It appears that the stiff and soft models have similar wake velocity profiles at both flow speeds.

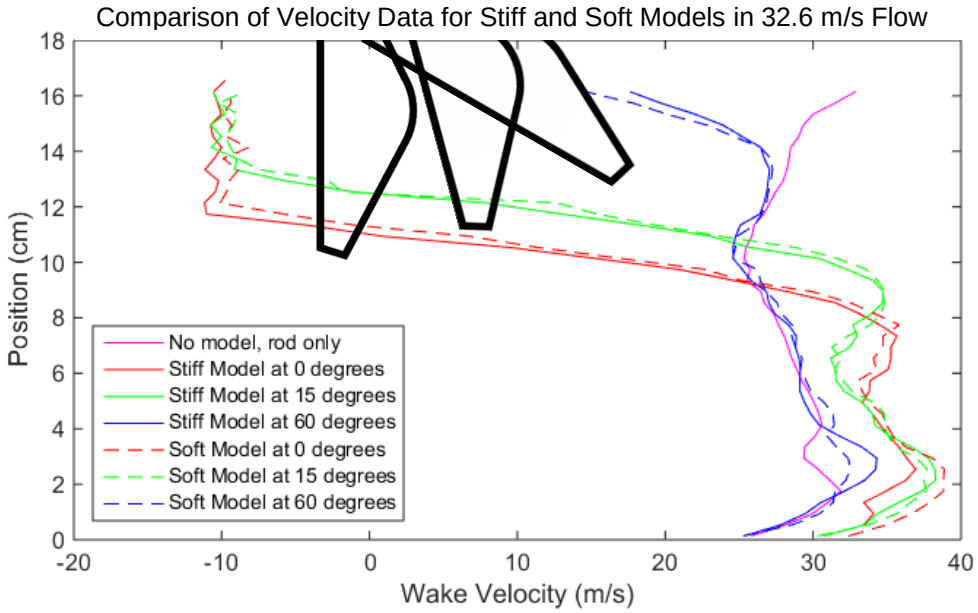

Figure 4-31: Comparison of the mean wake velocity vs position for stiff and soft models in 32.6 m/s flow.

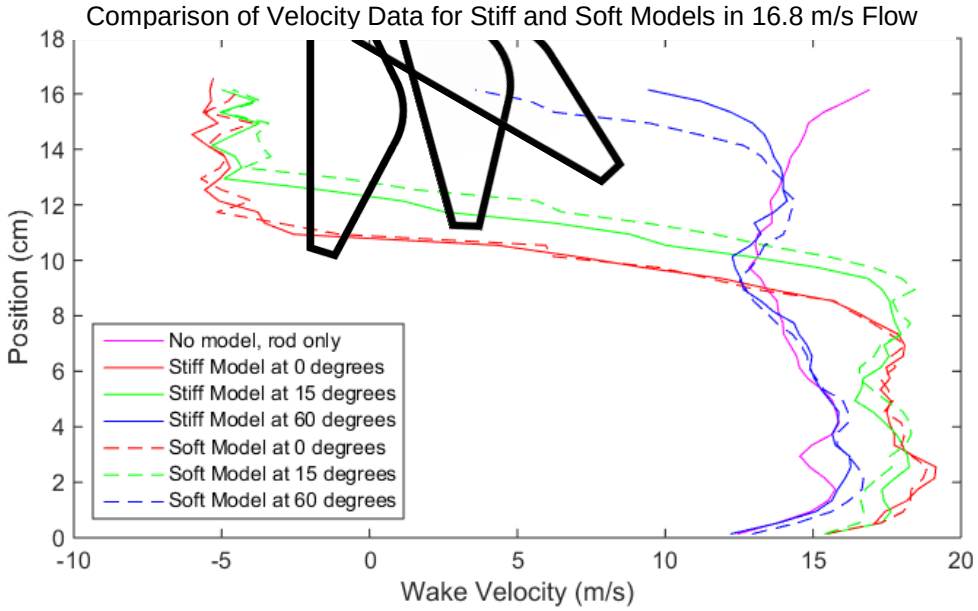

Figure 4-32: Comparison of the mean wake velocity vs position for stiff and soft models in 16.8 m/s flow.

4.5 Decelerator Model Similitude

A scaling technique similar to the one used in section 2.7 will be used in this section to compare the rapid prototyped scale model to the full scale ADEPT-VITaL decelerator in a wind tunnel on earth and in Venus's atmosphere. The calculations will be focused on the flexible vane of the full scale decelerator and the flexible panel of the model. It is important to note that there is a fundamental difference in the structure and the materials of the two. The flexible vane of the full scale decelerator is made from a flexible carbon fabric which is stretched over and attached to the ribs, while the flexible panel of the model is printed by a multi-material 3d printer so that it is surrounded on all edges by the stiff structure without any tension. As a result, the equation of motion for a membrane best describes the behavior of the full scale decelerator, while the equation of motion of a flat plate best describes the model.

A schematic of the decelerator model is shown in Figure 3-1. The diameter of the decelerator model is 4.82 inches (12.2 cm). The geometry of the model's flexible panel is shown below in Figure 4-33.

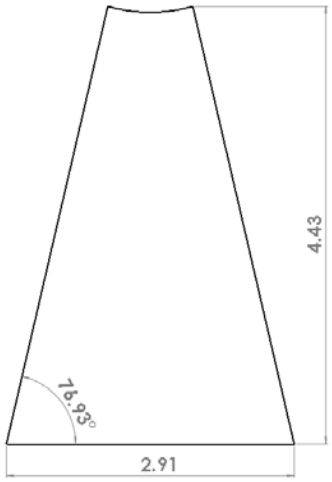

Figure 4-33: Detail drawing of scale model's flexible panel (cm)

The supporting structure of the soft decelerator (ribs, nose, and rim) is made out of a stiff material called VeroClear which has a high elastic modulus, while the flexible panel is made out of TangoPlus, a flexible and rubber-like material with a much lower elastic modulus. A full list of properties for both materials can be found in section 3.1.2. The relevant properties of the flexible panel are:

$$E = 0.354 \text{ MPa}$$

$$h = 0.003175 \text{ m}$$

$$\rho_s = 1120 \text{ kg/m}^3$$

The full scale of the ADEPT-VITaL decelerator is shown in Figure 2-14. The diameter of the full scale ADEPT decelerator is 6 meters. The surface of the ADEPT full scale decelerator is made out of a 3D woven carbon cloth [47-49]. The cloth has been tested under tension which is listed below with other relevant material properties:

$$T = 65673 \text{ N/m} – 131345 \text{ N/m}$$

$$h = 0.00381 \text{ m (0.15 in)}$$

$$\rho_s = 920 \text{ kg/m}^3$$

The scaling factor can be found by taking the ratio of the diameter of the model and full scale article; it is 1:49.2,

$$n = \frac{D_m}{D_{fs}} = \frac{0.122m}{6.00m} = \frac{1}{49.2} = 0.0203$$

The dimensions, material properties, flow conditions, and flow properties are listed in Table 4-10 below along with the non-dimensional parameters that have been calculated for the decelerator model as well as the full scale decelerator in a wind tunnel on earth

and in flight 90 km above the surface of Venus. Values for air density and kinematic viscosity on Venus were obtained from a reference [50].

	Wind Tunnel Model	Full Scale in Wind Tunnel	Full Scale in flight (90 km above surface of Venus)
Thickness, h (m)	0.003175	0.00381 (0.15in)	0.00381 (0.15in)
Decelerator diameter, d (m)	0.122	6	6
Length scale, L (cm)	1.89	92.6	92.6
Scale, n	0.02	1	1
ρ_s (kg/m^3)	1120	920	920
ρ_f (kg/m^3)	1.195 (at surface)	1.195 (at surface)	1.22×10^{-3} (at 90 km)
μ (kg/m·s)	1.79×10^{-5}	1.79×10^{-5}	$.877 \times 10^{-5}$ (at 90 km)
Velocity, V (m/s)	16.8 – 32.6	120 (could go faster)	4,000 m/s (at 90 km); min: 274.4 m/s (Mach 0.8) – max: 10,800 m/s
Re	147,000 - 284,000	16,960,000	515,000
V_{sound} (m/s)	343.2	343.2	215.10 (at 90 km)
Ma	0.049-0.095	0.350	18.60
E (MPa)	0.354	-	-
Flexural rigidity, $D = \frac{Eh^3}{12(1-\nu^2)}$	1.27×10^{-3}	-	-
Bending stiffness parameter, $\frac{D}{\rho_f V^2 L^3}$	0.539 – 0.143	-	-
Tension, T (kN/m)	0	66 - 131	66 - 131
Stiffness in tension parameter, $\frac{T}{\rho_f V^2 L}$	0	4.14	3.65
Inertia in bending parameter, $\frac{\rho_A}{\rho_f L}$	157.4	3.17	0.00310

Table 4-10: Dimensions, material properties, flow conditions, and non-dimensional parameters for the decelerator model and full scale decelerators in a wind tunnel on earth and in flight 90 km above the surface of Venus.

It is not possible to compare the structural stiffness parameter between this model and the full-scale article because the carbon cloth of the full-scale decelerator is tensioned and the flexible panels of the test article are in bending. The inertia parameter can be compared and are very different (2 - 3 orders of magnitude). The full scale tunnel model and the in-flight model have similar tension parameter.

The most challenging thing to overcome is the very large difference in velocity between the model or even full scale decelerator in a wind tunnel and the decelerator during reentry because at 90 km above the surface of Venus, the ADEPT decelerator will be travelling at 4,000 m/s which is Mach 18.6 and at the beginning of entry at 200 km above the surface of Venus, it will be travelling 10,800 m/s. In addition, compressible behavior of the flow conditions are introduced at these high Mach numbers which makes the comparison impossible. This exercise goes to show how difficult it is to match all of the parameters. There are tradeoffs and as you get closer to matching one parameter, another parameter might start to diverge.

If the velocities get out of range of the wind tunnel capability, the next easiest parameters to modify would be the length scale and panel thickness dimension by creating a new rapid prototyped model. The bending stiffness parameter and stiffness in tension parameters can be reduced by increasing the length scale. The bounding box dimensions of the 3d printer are the limitation on how large the model could be. The bending stiffness can also be decreased by making the panel thinner or using a softer material with a smaller modulus of elasticity.

4.6 Uncertainty

Uncertainty is calculated for a decelerator on a 19.05 cm rod at 0° angle of attack and a 12 inch rod without a model. The formula used to find the coefficient of drag is

$$C_D = \frac{F_D}{0.5A\rho V^2}$$

The force, F_D, is found by dividing the torque, T, measured by the torque transducer, by the arm length, l, which is also the length of the rod.

$$F_D = T / l$$

According to SolidWorks, the projected area of the decelerator at 0° angle of attack is a regular dodecagon, a 12-sided polygon with equal length sides. The area of a regular dodecagon can be calculated using

$$A = 3(2+\sqrt{3})a^2$$

Substituting this into the equation for C_D gives the following expression

$$C_D = \frac{T / l}{0.5\left[3(2+\sqrt{3})a^2\right)\rho V^2}$$

Uncertainty values:

1. Torque Transducer, T

   The range and accuracy of the torque transducer as listed on the datasheet for the Omega TQ201-25 is 0 – 2.82 N·m and 0.15% FSO respectively.

   The ADR01 voltage reference used to drive the bridge has 0.1% uncertainty, which becomes a measured uncertainty of 0.1%.

   The voltage reference was buffered using a BUF634, which has a ±30 mV offset (0.3% of 10 V) and a gain of 0.85 – 0.99 when driving a 100 – 1000 Ω load. This is as much as a 0.3% offset error and a 15% measured error. In the worst case, the BUF634 completely dominates the torque uncertainty. This uncertainty could

have been corrected for at the time of measurement, but unfortunately no measurement of the DC bias was made.

This makes the absolute uncertainty of the torque 2.82 N·m · 0.45% = ±0.01 N·m and a relative error of 15% of the measured value.

It should be noted that this is entirely a bias error, not random error; all measurements will be shifted up or down from the true value by the same amount. Random error will be much smaller.

2. Length of rod, *l*

   The length of rod was measured using a ruler with a resolution of 1 mm. The length was 19.05 cm and the uncertainty is 1 mm/2 = 0.0005 m.

3. Side of a dodecagon, *a*

   The side measured in SolidWorks is 0.03293m. Objet Connex500, the 3D printer which was used to print the model has a 600 dpi resolution which makes the uncertainty of this dimension 1/600 in = 4.2×10^{-5} m.

4. Air density, ρ

   1.195 kg/m^3 at 420 fan rpm (55 fps)

   1.186 kg/m^3 at 763 fan rpm (107 fps)

   The air density was computed based on the barometric pressure measured in the lab, the static pressure difference in the tunnel measured during run conditions using a temperature-controlled differential pressure transducer, and the temperature in the tunnel measured using a thermocouple. The dominant error

source is likely the temperature. A ±2 degree C thermocouple uncertainty would result in approximately a ±0.7 % uncertainty in density (2/300 K = 0.7%).

5. Flow velocity, *V*

   The experiment was run at two flow velocities: 16.8 m/s and 32.6.

   The flow velocity was computed using incompressible flow theory from the measured pitot-static data and using the air density determine as described above. No specifications were recorded regarding the pressure sensors used in the pitot-static tube, however, the dominant error source is likely the density, as described above. This would suggest approximately a ±0.4 % uncertainty in flow velocity as the velocity varies with the square root of density for incompressible flow.

6. Rod diameter, D

   0.00635 m

   The rod was a precision stainless steel rod and expected to be within 0.05 mm of the expected diameter, although this was not confirmed by measurement in the lab.

Measured variable	Nominal Value	Uncertainty
1. Torque, *T* (N·m)	varies	±0.01 N·m offset ± 15% of measured value
2. Length of rod, *l* (m)	0.1905 or 0.3048	±0.0005 m
3. Side of a dodecagon, a (m)	0.03293	4.2×10^{-5}
4. Air density, ρ (kg/m^3)	1.186	±0.7 % = ± 0.008 kg/m$_3$
5. Flow velocity, *V* (m/s)	16.8 or 32.6	±0.4 % = ± 0.1 m/s
6. Rod diameter, D (m)	0.00635	$\pm 5 \cdot 10^{-5}$ m

Table 4-11: Nominal values of measured variables and their uncertainty

The total uncertainty in the drag coefficient can then be bounded. In the worst case, where all errors trend in the same direction, either driving C_D up or down, we can

compute the maximum and minimum measured values of C_D we would see for a given true value,

$$C_D = \frac{T/l}{0.5\left[3(2+\sqrt{3})a^2)\right]\rho V^2} \text{ (for the model)}$$

$$C_D = \frac{T/(0.72l)}{0.5\left[D(0.56l)\right]\rho V^2} \text{ (for a rod by itself)}$$

Nominal Torque	Nominal C_D	Max measured C_D	Min measured C_D
1.6 N·m (model at 0^o in 32.6 m/s flow)	1.10	1.29	0.91
0.4 N·m (model at 0^o in 16.8 m/s flow)	1.03	1.24	0.83
0.33 N·m (rod in 32.6 m/s flow)	2.18	2.65	1.75
0.02 N·m (rod in 16.8 m/s flow)	0.550	0.919	0.216

Table 4-12: Nominal, maximum, and minimum values of C_D

Table 4-12 lists nominal values of the torque for some cases of the decelerator model and rod in flow and their corresponding $C_{D,}$ as well as the maximum and minimum values of the C_D. The percent uncertainty in the value of C_D decreases as the value of the torque increases. The uncertainty for the larger values of torque for the first three cases is around 20%. However, the last case of the rod in 16.8 m/s flow which has the smallest value of torque, 0.02 N·m, has a possible uncertainty in the value of C_D as much as 67%.

5 Conclusions and Future Work

5.1 Conclusions

This thesis investigates whether it is possible to use a PolyJet rapid prototype technique to construct a novel multi-material wind tunnel model that exhibits aeroelastic behavior. A scaled wind tunnel model of NASA's ADEPT decelerator was 3D printed at 1:49 scale for this investigation using an Objet printer and tested in the NASA Ames horizontal 15" x 15" indraft wind tunnel. In addition to analyzing the test results of the soft multi-material model, measurements taken for the soft model were compared to measurements taken for a stiff model made entirely out of a hard plastic.

The decelerator model was instrumented using a torque transducer to measure the forces exerted on the model in turbulent flow. The model was mounted on two rods of different length that are attached to the transducer. The velocity of the two flow conditions was 16.8 m/s (Re of 147,000) and 32.6 m/s (Re of 284,000). The validity of the collected decelerator model data was verified by comparing the calculated drag coefficient of the decelerator model to a similar geometry of the aeroshell of the Viking lander which was investigated in the 1970's. The drag coefficient of both stiff and soft decelerator models matched the expected results and was near one for both rod lengths at 0° and 15° angle of attack.

It is clear from the data that the underdamped mechanical system dominates the observed vibration of the decelerator model. The resonant frequencies of the system found by performing tap test of the models with the wind tunnel off matched the resonant frequency of the decelerator model under flow. Broadband unsteady forces caused by the

turbulent flow were responsible for the model vibration under flow conditions. The model vibrated at 28 Hz on the 19.05 cm rod and 16 Hz on the 30.50 rod independent of the angle of attack and flow rate parameters. The average percentage difference between the stiff and soft models for all cases was about 2% with a standard deviation of about 1%. In turn, as expected, the St of the decelerator models at the two different flow velocities did not match. This confirms the deduction that dynamic aeroelastic effects such as flutter were not visible from the collected data.

Measurements of the wake were also made by traversing a pitot tube behind the model up from the tunnel floor. The results were as expected. The flow sped up as it was forced around the decelerator. It was much slower or even reversed at some points behind the decelerator.

Nondimensional parameters were computed for the panels of the decelerator model and the full scale decelerator in a wind tunnel on Earth and during reentry conditions, 90 km above Venus's surface. An attempt was made to match the parameters to see if similitude could be achieved. It was possible to get the bending stiffness and stiffness in tension parameters close for the full scale decelerator in a wind tunnel and Venus by modifying the velocity of the flow in the wind tunnel for the full scale model. Both nondimensional parameters have a 13% error. Comparison of structural stiffness parameters was not possible because the full-scale article was tension dominated and the tunnel model was bending dominated. However, it may be possible to get the value closer to the full scale, by increasing the length scale (i.e., making the model larger) or increasing the velocity around the scaled model flow conditions. It was challenging to match the inertia in bending parameter because it is not possible to change the mass

density of the decelerator model and the fluid mass density of the flow. The inertia in bending parameter of the full scale model, 90 km over the surface of Venus, was larger than the scaled model by one order of magnitude. The length scale of the model can be decreased in order to increase the parameter for the scaled model, but that will not be enough because the parameter was directly proportion to the length scale. This exercise verified how difficult it is to match all of the nondimensional parameters to make a similar wind tunnel model.

Uncertainty analysis was performed to investigate the impact that uncertainty of variables used to calculate the drag force had on the results. The uncertainty of the torque, length of rod, length of a side of the dodecagon, air density, and flow velocity were considered. The largest uncertainty was introduced in the torque measurement because the buffer used for the voltage reference had a ±30 mV offset (0.3% of 10 V) and a gain of 0.85 – 0.99 when driving a 100 – 1000 Ω load. It should be noted that this error is entirely a bias error, which will cause an offset in the data collected from the true value by a constant number. This bias error on torque could result in uncertainty in the measured drag coefficient for the model of as much as 25% (see Table 4-12). However, since these are bias errors, all measured values would shift in the same direction; and thus the uncertainties do not change the conclusion that there is no observable difference between the soft and stiff models; nor do they impact the Strouhal number measurements. The remaining variables had a relatively low uncertainty of less than 1%.

5.2 Future Work

While the initial objective of creating the multi-material wind tunnel model and instrumenting a wind tunnel testing experiment was achieved, a number of issues remain to be investigated and expanded on. For further investigation of the ADEPT decelerator, the mounting scheme should be changed to avoid the dominating resonant frequency of the mechanical system.

A systems approach can also be used by inverting the system model in order to find the aero forcing function. More work should be done to test if filters with different cutoff frequencies can be used to find high frequency peaks that are a result of shedding of vortices.

To get closer to matching the nondimensional parameters, the model geometry can be scaled to increase the size of the model and length scale and also make the panels thinner. The 3D printer capabilities will need to be researched in order to find the limits of these two parameters. A different wind tunnel can also be used to test the model in a faster flow rate. Tension and bending should be further considered. More research is required to determine the scale and flow conditions required to achieve aeroelastic behavior. If more work is done with the ADEPT decelerator, the geometry itself should be changed to a 70° blunt nose cone, instead of the 60° cone that was tested in this thesis. This is because according to the literature, the ADEPT decelerator will have a 70° angle.

Ultimately, it is still unknown if the full scale ADEPT decelerator exhibits aeroelastic behavior and at what flow velocity and properties. That said, it is unclear that aeroelastic behavior will be visible even if similitude is achieved. A better option might be to select a

different aircraft or part of aircraft that is known to exhibit flutter to try to achieve similitude to see if the multi-material model will exhibit similar behavior.

When working with the mounting rod alone with no model attached, the measured drag coefficients differed from expected values by as much as 54%. In addition, the resonant frequency of the rod varied at two different flow velocities. Further investigation of these unexpected results would bolster confidence in the experiments.

Finally, the viscoelastic and damping properties of the flexible TangoPlus material should be investigated to see if the material would dampen any aeroelastic behavior which might be visible for a given geometry.

References

1. Jamieson, R., *New options in aerodynamic modelling. CAD, CFD, stereolithography and shading in a workstation environment.* Computer-Aided Engineering Journal, 1990. **7**(3): p. 75-79.
2. Landrum, D.B., et al. *Evaluation of stereolithography rapid prototyping for low speed airfoil design*. in *Aerospace Sciences Meetings & Exhibit, 35th*. 1997. Reno, NV: AIAA.
3. Springer, A., K. Cooper, and F. Roberts. *Application of rapid prototyping models to transonic wind tunnel testing*. in *Aerospace Sciences Meeting & Exhibit, 35th*. 1997. Reno, NV; United States: AIAA.
4. Springer, A. and K. Cooper. *Comparing the aerodynamic characteristics of wind tunnel models produced by rapid prototyping and conventional methods*. in *AIAA Applied Aerodynamics Conference, 15th*. 1997. Atlanta, GA; United States.
5. Springer, A., *Evaluating aerodynamic characteristics of wind-tunnel models produced by rapid prototyping methods.* Journal of Spacecraft and Rockets, 1998. **35**(6): p. 755-759.
6. Springer, A.M., *Application of Rapid Prototyping Methods to High-Speed Wind Tunnel Testing*. 1998: Aerospace Database.
7. Springer, A. and K. Cooper, *Aerodynamic properties analysis of rapid prototyped models versus conventional machined models.* STAR, 1999. **37**.
8. Chuk, R.N. and V.J. Thomson, *A comparison of rapid prototyping techniques used for wind tunnel model fabrication.* Rapid Prototyping Journal, 1998. **4**(4): p. 185-196.
9. Hildebrand, R., R. Eidson, and C. Tyler. *Development of a low cost, rapid prototype lambda wing-body wind tunnel model*. in *21st AIAA Applied Aerodynamics Conference*. 2003. Orlando, FL.
10. Kroll, E., D. Artzi, and G. Ralbag. *Structural design guidelines for wind tunnel models made by rapid prototyping*. in *27th Congress of the International Council of the Aeronautical Sciences 2010, ICAS 2010, September 19, 2010 - September 24, 2010*. 2010. Nice, France: ICAS Secretariat.
11. Kroll, E. and D. Artzi, *Enhancing aerospace engineering students' learning with 3D printing wind-tunnel models.* Rapid Prototyping Journal, 2011. **17**(5): p. 393-402.
12. Heyes, A.L. and D.A.R. Smith, *Rapid Technique for Wind-Tunnel Model Manufacture.* Journal of Aircraft, 2004. **41**(2): p. 413-415.
13. Tyler, C., W. Braisted, and J. Higgins. *Evaluation of Rapid Prototyping Technologies for Use in Wind Tunnel Model Fabrication*. in *43rd AIAA Aerospace Sciences Meeting and Exhibit*. 2005.
14. Shun, S. and N.A. Ahmed, *Rapid Prototyping of Aerodynamics Research Models.* Applied Mechanics and Materials, 2012. **217-219**: p. 2016.
15. Aghanajafi, S., R. Adelnia, and S. Daneshmand, *Production of wind tunnel testing models with use of rapid prototyping methods.* WSEAS Transactions on Circuits and Systems, 2006. **5**(4): p. 555-561.
16. Daneshmand, S., A.A. Nadooshan, and C. Aghanajafi, *Investigation of Layer Thickness and Surface Roughness on Aerodynamic Coefficients of Wind Tunnel RP Models*, in *Proceedings of World Academy of Science, Engineering and Technology, Vol 26, Parts 1 and 2, December 2007*, C. Ardil, Editor. 2007. p. 7-12.
17. Daneshmand, S., C. Aghanajafi, and A. Ahmadi Nadooshan, *The effect of chromium coating in RP technology for airfoil manufacturing.* Sadhana, 2010. **35**(5): p. 569-584.

18. Zhou, Z., et al., *Design and fabrication of a hybrid surface-pressure airfoil model based on rapid prototyping.* Rapid Prototyping Journal, 2008. **14**(1): p. 57-66.
19. Zhu, W., et al., *Design and fabrication of stereolithography-based aeroelastic wing models.* Rapid Prototyping Journal, 2011. **17**(4): p. 298-307.
20. Udroiu, R. and F. Dogaru, *Rapid manufacturing of parts for wind tunnel testing using polyjet technology.* Annals of DAAAM & Proceedings, 2009: p. 581.
21. Udroiu, R., *Applications of additive manufacturing technologies for aerodynamic tests.* Academic Journal of Manufacturing Engineering, 2010. **8**(3): p. 96-101.
22. Udroiu, R., D.-A. Serban, and G. Belgiu, *Optimisation of rapid prototyping process for electrical vehicle manufacturing.* Annals of DAAAM & Proceedings, 2010: p. 451.
23. Negi, S., S. Dhiman, and R.K. Sharma, *Basics, Applications and Future of Additive Manufacturing Technologies: A Review.* Journal of Manufacturing Technology Research, 2013. **5**(1/2): p. 75-96.
24. Upcraft, S. and R. Fletcher, *The rapid prototyping technologies.* Assembly Automation, 2003. **23**(4): p. 318-330.
25. *Triple-jetting 3-D Printing Technology*, in *R & D*. 2014, Advantage Business Media: Highlands Ranch.
26. Singh, R., *Process capability study of polyjet printing for plastic components.* Journal of Mechanical Science and Technology, 2011. **25**(4): p. 1011-1015.
27. Dimitrov, D., K. Schreve, and N. de Beer, *Advances in three dimensional printing - state of the art and future perspectives.* Rapid Prototyping Journal, 2006. **12**(3): p. 136-147.
28. Danehy, P.M., et al., *Fluorescence imaging and streakline visualization of hypersonic flow over rapid prototype wind-tunnel models.* Proceedings of the Institution of Mechanical Engineers Part G-Journal of Aerospace Engineering, 2008. **222**(G5): p. 637-651.
29. Alderfer, D.W., et al., *Fluorescence visualization of hypersonic flow over rapid prototype wind-tunnel models.* STAR, 2007. **45**(3).
30. Mathioudakis, K., V. Dedoussis, and V. Canellidis, *Aerodynamic experimental investigation using stereolithography fabricated test models: the case of a linear compressor blading cascade.* Virtual and Physical Prototyping, 2008. **3**(3): p. 151-157.
31. Aghanajafi, C. and S. Daneshmand, *Integration of Three-Dimensional Printing Technology for Wind-Tunnel Model Fabrication.* Journal of Aircraft, 2010. **47**(6): p. 2130-2135.
32. Wang, C., et al., *Design and fabrication of an aircraft static aeroelastic model based on rapid prototyping.* Rapid Prototyping Journal, 2015. **21**(1): p. 34-42.
33. Venkatapathy, E., et al. *Adaptive deployable entry and placement technology (ADEPT): A feasibility study for human missions to mars*. in *21st AIAA Aerodynamic Decelerator Systems Technology Conference and Seminar*. 2011. Dublin, Ireland.
34. Smith, B., et al. *Venus In Situ Explorer Mission design using a mechanically deployed aerodynamic decelerator*. in *2013 IEEE Aerospace Conference*. Big Sky, MT, United States: IEEE.
35. Gage, P. and P. Wercinski, *Hypersonic Deployable Decelerators. Adaptable, Deployable Entry Technology and Placement (ADEPT) Project.* IPPW10 EDL Short Course, 2013.
36. Wercinski, P., et al., *Adaptable, Deployable Entry and Placement Technology (ADEPT) for Future Mars Missions.* IPPW10 Future Mars II Session, 2013.
37. Weiland, C., *Aerodynamic data of space vehicles*. 2014, Heidelberg: Springer.
38. Bisplinghoff, R.L. and H. Ashley, *Principles of aeroelasticity*. 1962, New York: Wiley.
39. Bisplinghoff, R.L., H. Ashley, and R.L. Halfman, *Aeroelasticity*. 1983, Dover Publications.

40. Wolowicz, C.H., J.S. Bowman Jr, and W.P. Gilbert, *Similitude Requirements and Scaling Relationships as Applied to Model Testing.* NASA Technical Paper, 1979(1435).
41. Lambourne, N.C. and C. Scruton, *Conditions of similitude for flutter tests on models (Similitude conditions for flutter tests on models in hypervelocity and low speed wind tunnels)*, in *Onera Aeroelasticity Manual*. 1967.
42. Bisplinghoff, R.L., H. Ashley, and R.L. Halfman, *Aeroelastic Model Theory.* STAR, 2007. **45**(5).
43. Leissa, A.W. and M.S. Qatu, *Vibrations of continuous systems*. 2013, New York: McGraw-Hill.
44. Megson, T.H.G., *An introduction to aircraft structural analysis*. 2010, Amsterdam; Boston: Butterworth-Heinemann/Elsevier.
45. Stratasys. *PolyJet Materials Data Sheet*. 2015 [cited 2015 Jan 15]; Available from: http://www.stratasys.com/~/media/Main/Secure/Material Specs MS/PolyJet-Material-Specs/PolyjetMaterialsDataSheet-08-13.pdf.
46. Sumer, B.M. and J. Fredsøe, *Hydrodynamics around cylindrical structures*. Advanced Series on Ocean Engineering, ed. Sumer. Vol. 26. 2006, London, eBook: World Scientific Pub.
47. Arnold, J.O., et al. *Thermal and structural performance of woven carbon cloth for adaptive deployable entry and placement technology*. in *AIAA Aerodynamic Decelerator Systems Technology Conference*. 2013.
48. Arnold, J., et al. *Arcjet Testing of Woven Carbon Cloth for Use on Adaptive Deployable Entry Placement Technology*. in *International Planetary Probe Workshop*. 2013.
49. Wercinski, P.F., et al., *Enabling Venus In-Situ Science-Deployable Entry System Technology, Adaptive Deployable Entry and Placement Technology (ADEPT): A Technology Development Project funded by Game Changing Development Program of the Space Technology Program.* Oral/Visual Presentation, 2012.
50. Petropoulos, B. and P. Telonis, *Physical parameters of the atmosphere of Venus from Venera 15 and 16 missions.* Earth, Moon, and Planets, 1993. **63**(1): p. 1-7.